TECHNISCHE UNIVERSITÄT MÜNCHEN
Fakultät für Medizin

Opportunistic Screening for Osteoporosis Based on Vertebral Bone Mineral Density Measurements with Dual-Layer Spectral Computed Tomography

Ferdinand Otto Rudolf Roski

Vollständiger Abdruck der von der Fakultät für Medizin der Technischen Universität München zur Erlangung des akademischen Grades eines **Doktors der Medizin (Dr. med.)** genehmigten Dissertation.

Vorsitz: apl. Prof. Dr. Stefan Thorban

Prüfer der Dissertation:
1. Priv.-Doz. Dr. Benedikt Schwaiger
2. apl. Prof. Dr. Thomas Baum

Die Dissertation wurde am 21.07.2022 bei der Technischen Universität München eingereicht und durch die Fakultät für Medizin am 03.01.2023 angenommen.

SCHOOL OF MEDICINE

TECHNICAL UNIVERSITY OF MUNICH

Medical Program (Dr. med.)
Cumulative Thesis

Opportunistic Screening for Osteoporosis Based on Vertebral Bone Mineral Density Measurements with Dual-Layer Spectral Computed Tomography

Ferdinand Otto Rudolf Roski

Contents

Abstract

Osteoporosis poses a substantial burden to patients and health systems globally, being associated with fragility fractures, increased mortality, impaired quality of life, and high costs. Manifold causative factors contribute to loss of BMD and microarchitectural changes and the pathophysiological mechanisms of osteoporosis are complex. Fundamentally, there are effective pharmacological options to reverse bone loss or at least stop its progression. However, there is still a large diagnostic gap leading to patients that would be eligible for therapy, but remain undetected and thus, untreated. X-ray computed tomography is the gold standard for spinal imaging when it comes to accurate fracture assessment, providing a high spatial resolution, high contrast regarding bone tissue, and short examination times. However, considerable radiation exposure limits the applicability for bone loss diagnostics. The use of opportunistic screening for low BMD — i.e., in non-dedicated imaging data acquired for other clinical indications — has the potential to overcome this barrier. Moreover, advanced technical realizations like dual-layer spectral CT (DLCT) allow the extraction of additional information emerging from differential spectral attenuation. The purpose of this thesis was to apply DLCT imaging methods *in vivo* for bone loss diagnostics and evaluate its clinical potential for opportunistic BMD measurements regarding accuracy and diagnostic value for both native and contrast-enhanced examinations from day-to-day clinical care. Both scientific papers this dissertation is based on describe prospective, cross-sectional, mono-center analyses of previously acquired imaging data. Fundamentally, virtual monoenergetic images at different energy levels derived from DLCT data were used for hydroxyapatite-specific BMD quantification. For the first *in-vivo* application, bone mineral quantification was implemented via calibration to hydroxyapatite with the European Spine Phantom, and results were compared with QCT-BMD as the standard of reference. For contrast-enhanced CT examinations, parallel use of spectral information with DLCT-based BMD and vascular iodine contrast measurements was implemented, additionally adjusting for iodine-contrast-related alterations of CT attenuation values. In summary, DLCT allows for BMD assessment in routine clinical examinations without the need for in-scan calibration phantoms. With adjustments for vascular iodine contrast, BMD can be opportunistically measured in virtually all DLCT data acquired in clinical routine. Opportunistic use of DLCT for bone loss diagnostics may help optimizing clinical care by expanding applicability, concomitantly sparing patients additional dedicated BMD assessment.

Zusammenfassung

Osteoporose stellt weltweit eine erhebliche Belastung für Patienten und Gesundheitssysteme dar, da sie mit pathologischen Frakturen, erhöhter Sterblichkeit, eingeschränkter Lebensqualität und hohen Kosten verbunden ist. Die pathophysiologischen Mechanismen der Osteoporose sind komplex und vielfältige Ursachen tragen zum Knochendichteverlust und zu mikrostrukturellen Veränderungen bei. Grundsätzlich gibt es wirksame pharmakologische Optionen, um den Knochenverlust umzukehren oder zumindest sein Fortschreiten aufzuhalten. Es gibt jedoch immer noch eine große diagnostische Lücke, die dazu führt, dass Patienten, die für eine Therapie in Frage kämen, unerkannt und damit unbehandelt bleiben. Die Computertomographie ist der Goldstandard in der Wirbelsäulenbildgebung für die genaue Beurteilung von Knochenbrüchen. Sie bietet eine hohe räumliche Auflösung, hohen Kontrast des Knochengewebes und kurze Untersuchungszeiten. Die erhebliche Strahlenbelastung schränkt jedoch die Anwendbarkeit für die Osteoporose-Diagnostik ein. Der Einsatz eines opportunistischen Screenings für niedrige Knochendichte hat das Potenzial, diese Barriere zu überwinden. Darüber hinaus ermöglichen fortschrittliche technische Realisierungen wie die Zweischicht-Spektral-CT (DLCT) einen zusätzlichen Informationsgewinn durch differentielle spektrale Abschwächung. Ziel dieser Arbeit war die in-vivo Anwendung der DLCT für die Osteoporose-Diagnostik sowie die Beurteilung ihres klinischen Potenzials für opportunistische Knochendichtemessungen mit Blick auf Messpräzision und diagnostischen Wert für native und kontrastverstärkte Untersuchungen aus dem klinischen Alltag. Beide wissenschaftlichen Arbeiten, auf denen diese Dissertation basiert, sind prospektive, monozentrische Querschnittsanalysen von zuvor erhobenen Bildgebungsdaten. Grundsätzlich wurden aus DLCT-Datensätzen virtuelle monoenergetische Bilder verschiedener Energieniveaus abgeleitet und zur phantomlosen Knochendichte-Quantifizierung verwendet. Zunächst wurde für die In-vivo-Anwendung eine Kalibrierung auf Hydroxylapatit mit dem *European Spine Phantom* implementiert und die Ergebnisse mit QCT-BMD als Referenzstandard verglichen. Für kontrastverstärkte CT-Untersuchungen wurde eine parallele Nutzung der spektralen Informationen mit DLCT-basierten Knochendichte- und vaskulären Jodkontrastmessungen eingesetzt, wobei zusätzlich eine Adjustierung für jodkontrastbedingte Veränderungen der Messwerte vorgenommen wurde. Zusammenfassend ermöglicht die DLCT eine Knochendichtemessung bei klinischen Routineuntersuchungen auch ohne ein Referenzphantom zur Kalibrierung während des Scans. Mit Anpassungen für den vaskulären Jodkontrast kann die Knochendichte in praktisch allen DLCT-Datensätzen, die in der klinischen Routine erfasst werden, opportunistisch gemessen werden. Die opportunistische Nutzung der DLCT für die Diagnostik von Osteoporose kann dazu beitragen, die klinische Versorgung zu optimieren, indem sie die Anwendbarkeit erweitert und gleichzeitig den Patienten zusätzliche spezielle BMD-Messungen erspart.

Publications

This cumulative dissertation is based on the following two journal publications (referred to as J-I and J-II), of which preliminary results were presented in related scientific talks (each speaker highlighted with underscore):

J-I **Bone mineral density measurements derived from dual-layer spectral CT enable opportunistic screening for osteoporosis**
Roski F*, Hammel J*, Mei K, Baum T, Kirschke JS, Laugerette A, Kopp FK, Bodden J, Pfeiffer D, Pfeiffer F, Rummeny EJ, Noël PB, Gersing AS and Schwaiger BJ.
** shared first authorship*
European Radiology 2019 May 21 (29, 6355-6363)
doi: 10.1007/s00330-019-06263-z

J-II **Opportunistic osteoporosis screening: contrast-enhanced dual-layer spectral CT provides accurate measurements of vertebral bone mineral density**
Roski F, Hammel J, Mei K, Haller B, Baum T, Kirschke JS, Pfeiffer D, Woertler K, Pfeiffer F, Noël PB, Gersing AS and Schwaiger BJ.
European Radiology 2020 October 14 (31, 3147-3155)
doi: 10.1007/s00330-020-07319-1

Opportunistic osteoporosis screening using hydroxyapatite-specific vertebral bone mineral density measurements derived from dual-layer CT
Bodden J, Roski F, Hammel J, Mei K, Baum T, Laugerette A, Rummeny EJ, Gersing AS, Schwaiger BJ. European Congress of Radiology, Vienna 2019.

Osteoporose-Screening anhand Hydroxylapatit-spezifischer Knochendichtemessungen mittels Dual-Layer CT
Roski F, Hammel J, Mei K, Baum T, Kirschke JS, Laugerette A, Kopp F, Pfeiffer D, Pfeiffer F, Rummeny EJ, Noël P, Gersing AS, Schwaiger BJ. 100. Deutscher Röntgenkongress, Leipzig 2019.

Präzise opportunistische Knochendichtemessungen in der Wirbelsäule basierend auf asynchron kalibrierten, kontrastmittelverstärkten Routineuntersuchungen mittels Dual-Layer Spektral-CT
Roski F, Hammel J, Mei K, Baum T, Kirschke JS, Pfeiffer D, Rummeny EJ, Noël PB, Woertler K, Gersing AS, Schwaiger BJ. 5. Jahrestagung der Deutschen Gesellschaft für muskuloskelettale Radiologie, Berlin 2019.

Declaration of consent from co-authors of journal publications

All co-authors of any or all the journal publications listed below (J-I and/or J-II), gave their written consent to its/their inclusion in the doctoral candidate´s cumulative dissertation as well as its subsequent publication. Furthermore, they confirmed that the respective original articles were composed under the lead of the doctoral candidate.

J-I **Bone mineral density measurements derived from dual-layer spectral CT enable opportunistic screening for osteoporosis**

Roski F*, Hammel J*, Mei K, Baum T, Kirschke JS, Laugerette A, Kopp FK, Bodden J, Pfeiffer D, Pfeiffer F, Rummeny EJ, Noël PB, Gersing AS and Schwaiger BJ.

* shared first authorship

European Radiology 2019 May 21 (29, 6355-6363)

doi: 10.1007/s00330-019-06263-z

J-II **Opportunistic osteoporosis screening: contrast-enhanced dual-layer spectral CT provides accurate measurements of vertebral bone mineral density**

Roski F, Hammel J, Mei K, Haller B, Baum T, Kirschke JS, Pfeiffer D, Woertler K, Pfeiffer F, Noël PB, Gersing AS and Schwaiger BJ.

European Radiology 2020 October 14 (31, 3147-3155)

doi: 10.1007/s00330-020-07319-1

Compliance with ethical standards

All investigations were performed in accordance with the ethical standards of the institutional review board (The Ethics Commission of the Medical Faculty, Technical University of Munich, Germany) and with the 1964 Helsinki declaration and its later amendments.

Abbreviations

aBMD	areal bone mineral density
ACR	American College of Radiology
ADT	androgen deprivation therapy
BMD	bone mineral density
BMI	body mass index
CT	computed tomography
DECT	dual-energy computed tomography
DLCT	dual-layer computed tomography
DSCT	dual-source computed tomography
DXA	dual-energy x-ray absorptiometry
EBM	extracellular bone matrix
FBP	filtered back projection
FEA	finite element analysis
FRAX®	Fracture Risk Assessment Tool
FSU	functional spinal unit
GEE	generalized estimated equation
HA	calcium hydroxyapatite
HR-pQCT	high-resolution peripheral quantitative computed tomography
IR	iterative reconstruction
ISCD	International Society for Clinical Densitometry
HU	Hounsfield Units
MAE	means of absolute error
M-CSF	macrophage colony-stimulating factor
MRI	magnetic resonance imaging
NIH	National Institute of Health (United States of America)
PACS	picture archiving and communication system
PDFF	proton density fat fraction
pDXA	peripheral dual-energy x-ray absorptiometry
pQCT	peripheral quantitative computed tomography
QCT	quantitative computed tomography
QUS	quantitative ultrasound
RANK	Receptor Activator of Nuclear Factor-B
RANKL	Receptor Activator of Nuclear Factor-B ligand
ROI	region of interest
SBI	Spectral Base Image
SD	standard deviation
SERM	selective estrogen-receptor modulator
STIR	short TI inversion recovery
TBS	trabecular bone score
TNC	true non-contrast
vBMD	volumetric bone mineral density
VMI	virtual monoenergetic image
VNC	virtual non-contrast
WHO	World Health Organization

1 Introduction

1.1 Principles of computed tomography

1.1.1 X-ray generation and interaction of photons with matter

The clinical introduction of x-ray computed tomography (CT) in the 1970s has had a radical and lasting impact on the field of radiology since the modality nowadays constitutes a key tool allowing for both numerous diagnostic and — with respect to image-guided interventions — therapeutic possibilities. Imaging with medical CT systems is based on the use of x-rays, a form of high-energy electromagnetic radiation (Pelc, 2014). In contrast to conventional radiographs, they provide cross-sectional images with x-rays penetrating examined structures from various projection angles. In a clinical context, CT has found a broad application for a variety of working diagnoses, particularly relating to neuroimaging (e.g., ischemic stroke, intracranial bleeding), thoracic imaging (e.g., lung pathologies, pulmonary embolism, aortic dissection), abdominal imaging (e.g., intestinal pathologies, tumor screening, urolithiasis), vascular imaging (e.g., aortic aneurysms, peripheral artery occlusive disease) or musculoskeletal imaging (e.g., spinal disorders, articular fractures). Furthermore, short examination times and widespread availability in developed regions qualify the CT for initial orientating imaging of polytraumatized patients in emergency care settings (Aran et al., 2014; Odle, 2020). However, its use is limited by substantial radiation exposure with ionizing, dose-dependent effects of x-rays being responsible for radiation-induced cellular damage (Reisz, Bansal, Qian, Zhao, & Furdui, 2014) and carcinogenic, mutagenic as well as reprotoxic alterations.

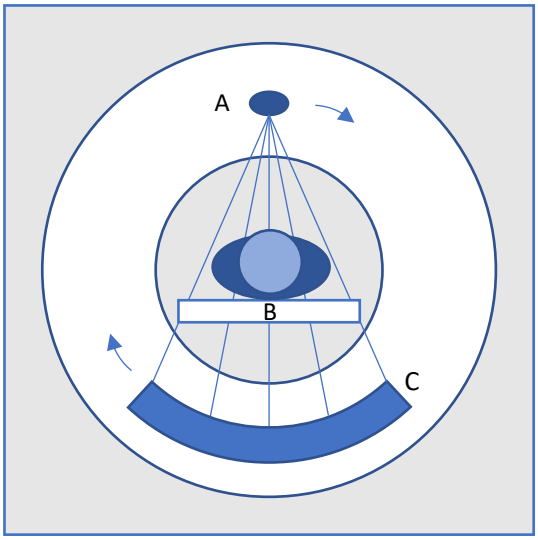

Figure 1: Schematic diagram of the computed tomography scanner setup.

As for the technical setup, a CT scanner essentially consists of an x-ray tube (A) with an opposing detector (C), both integrated in the rotating gantry as well as a patient table (B) that can be continuously moved in the so-called z-axis, i.e., perpendicular to the image plane (Fig. 1). The x-ray tube generates a spectrum of x-ray photons with different energies: First off, an electrically heated cathode thermically emits electrons. A high tube potential of usually 80 to 140 kVp (Withers, 2021) effects and regulates the acceleration of these electrons through the air-evacuated housing towards the anode. When impinging at the focal spot, the electrons interact with the anode material and get abruptly decelerated. Here, a major part of the electrons' kinetic energy converts to heat and a minor part to x-ray photons in form of a continuous spectrum of *bremsstrahlung* as well as intensity peaks of characteristic radiation originating from direct interactions with electrons of the anode material. An adjustable tube-side collimator then confines the dispersion of x-rays at the exit window.

The maximum x-ray photon energy or else the threshold wavelength is predetermined by the kinetic energy of an electron, which in turn depends on the applied tube potential (Withers, 2021). In modern CT systems, an efficient generator is required to supply the electric power in conjunction with a fast and stable tube current and tube potential available in high repetition. Moreover, several constructive elements are needed for sufficient heat dissipation, such as a surrounding cooling liquid and rotational design of the anode to avoid exceeding its heat storage capacity (Ginat & Gupta, 2014).

On the way to the opposed detector, the x-ray photons penetrate the examined regions of the patient's body thereby gradually losing energy. As x-rays interact with matter, e.g., in the form of different body tissues, two principal effects dominate the attenuation of x-ray intensity in the energy range relevant for clinical CT imaging — photoelectric absorption and inelastic scattering (Compton scattering).

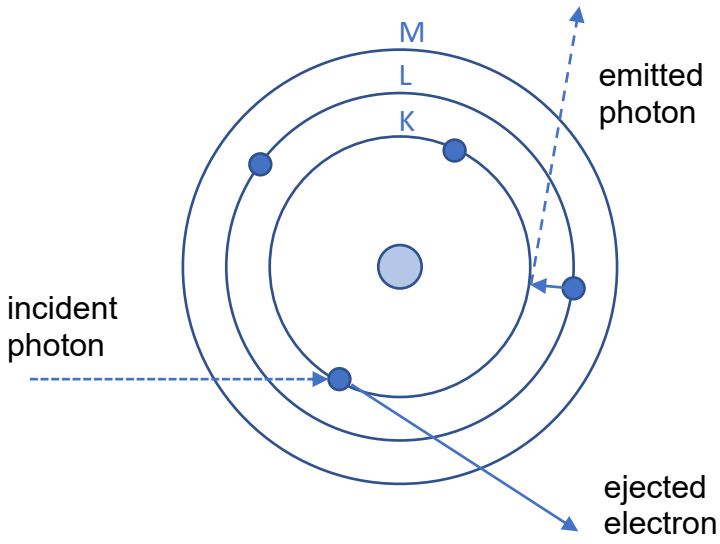

Figure 2: Photoelectric absorption.

Adapted from: "Events in the photoelectric absorption progress" (Alpen, 1998)

As for the photoelectric effect, the entire energy of an incident x-ray photon gets transferred to an inner shell electron, typically of the K-shell, which in turn gets ejected from the atom. To retake the original low-energy state of the atom, an outer shell electron fills up this vacancy of the K-shell, thereby emitting a photon of the respective energy difference (Fig. 2). Photoelectric absorption depends on the atomic number (Z), physical density (ρ) and varies inversely to the photon energy (E), with experimentally derived values being approximately $3 \leq m \leq 4$ and $3 \leq n \leq 3.5$ (Heismann, 2003):

$$photoelectric\ absorption \sim \rho \times \frac{Z^m}{E^n}$$

The Compton effect refers to a form of scattering, in which an incident x-ray photon transfers a part of its energy to a weakly bound outer shell electron. The scattered photon gets deflected and — according to the law of energy conservation — moves on with decreased energy or longer wavelength (Compton shift).

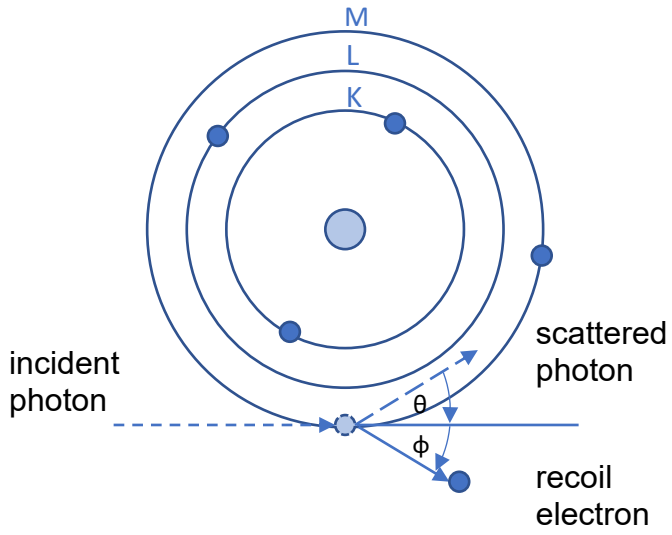

Figure 3: Compton scattering.
Adapted from: “Clinical applications of radiophotoluminescence (RPL) dosimetry in evaluation of patient radiation exposure in Radiology. Determination of absorbed and effective dose” (Manninen, 2014)

By contrast to photoelectric absorption, Compton scattering is independent of a material’s atomic number. Nonetheless, the Compton effect´s contribution to total attenuation is still material-dependent, as more radiation energy gets absorbed in tissues with higher physical density. In contrast to absorbed x-ray photons, all transmitted ones contribute to the image generation at the detector level. As reflected by the above formulae, the Compton effect is less

dependent on photon energy than the photoelectric effect. The energy-dependency of these two subprocesses represents the basis for compositional imaging using advanced CT methods like dual-energy CT (DECT), with the Photoelectric effect being the dominant influence at low energy range, while energy-dependency of Compton effect is markedly less pronounced (Heismann, 2003).

$$Compton\ effect \sim \frac{\rho \times e}{E}$$

The introduction of slip-ring technology facilitated the faster, helical acquisition of modern CT scanners (Ginat & Gupta, 2014) with two synchronous and continuous movements: gantry rotation and table movement. This allows for uncoupling table movement and image reconstruction, thus inducing higher flexibility and fewer motion artifacts. Some applications, however, such as specific cranial CT protocols, still utilize an axial acquisition pattern. This sequential acquisition mode reduces a certain type of scanning artifacts related to incongruencies of spirally acquired image data that are not compensable with z interpolation (helical artifacts) and may arise when attenuation behavior of anatomical structures abruptly changes in z-direction (Barrett & Keat, 2004).

Minimizing radiation exposure is pivotal in clinical CT imaging and there are several essential acquisition protocol parameters relevant for optimal dose management: the tube potential [kVp], the tube current [mA], exposure time [s], the slice collimation, and the pitch factor (Willemink & Noel, 2019). The tube potential between cathode and anode determines the maximum energy of the emitted x-ray spectrum, whereas the product of tube current and exposure time [mAs] determines the quantity of emitted radiation. Both parameters therefore influence radiation dose and affect image quality. Of note, modern CT systems use modulation of tube current to adjust for individual patient anatomy, allowing for substantial reduction of radiation dose (Kalender, Wolf, & Suess, 1999). In theory, any variation in slice collimation can also affect radiation dose by means of overbeaming or overranging effects, however, for smaller slice collimations in clinical practice, increases in spatial resolution outweigh concurrently increased image noise, leading to a dose-adjusted benefit in image quality (Nagel, 2007). In helical CT, the pitch factor is commonly defined as the relation of table movement to slice collimation during a complete gantry rotation. For fixed slice collimation, increasing the pitch factor (e.g., to values between 1,5 and 2) extends the length scanned within a certain time, or conversely reduces exposure time for a defined scan length (Prokop, 2007). Slice collimation refers to the focusing of the x-ray beam and is achieved by a tube-side shutter arrangement as well as a respective selection of active detector elements, thus also determining the acquisition slice thickness along the z-axis (Goldman, 2008).

1.1.2 Data acquisition and image reconstruction

Within the CT detector, transmitted x-rays are being converted to imaging data, thus being the usable image-generating fraction of total radiation. Modern CT scanners use solid-state scintillation detectors consisting of multiple individual detector elements. First, a scintillator absorbs the impinging x-ray photons, thereby transforming their energy to light photons, which in turn are sensed by a subjacent photodiode that translates the registered information into an electric signal corresponding to the absorbed x-ray photon intensity.

Based on the detected intensity of transmitted x-ray photons, the absorption coefficient μ of a certain projection can be calculated by means of the Beer-Lambert law (Hubbell, 1999):

$$I = I_0 \times e^{-\mu \times d}$$

I: attenuated intensity
I_0: initial intensity
μ: absorption coefficient, material- and energy-dependent
d: distance

The entirety of measured attenuated x-ray intensities represents the information on the differential tissue absorption behavior of an examined layer and is the foundation of CT image generation, as the eventual CT images essentially represent a spatial distribution of these attenuation coefficients. With a normalization to the attenuation coefficient of water, the calculated mean attenuation coefficients of the volume elements (voxels) are translated to CT numbers (or Hounsfield Units, HU) (Brooks & Di Chiro, 1976), which are eventually depicted as gray-scale values in a corresponding pixel matrix:

$$HU = \frac{1000 \times (\mu - \mu_{H_2O})}{\mu_{H_2O}}$$

For 12-bit CT images, the scale ranges from -1024 to 3071 HU, with pure air and water at both standard temperature (0 °C) and pressure (10^5 pascals) constituting two benchmarks at -1000 and 0 HU, respectively (Ese, 2019). Brighter voxels represent more attenuating or hyperdense tissues (e.g., bone) whereas less attenuating, hypodense tissues (e.g., fat) are imaged as dark voxels.

Downstream to the data acquisition on the detector level, a high-performance computer processes cross-sectional CT images based on the raw projection data of the examined volume and assigns attenuation values to individual voxels that are eventually integrated within a two-dimensional image matrix.

As for the image reconstruction, filtered back projection (FBP) is a common analytical algorithm for CT image reconstruction. Within an examined slice, all registered x-ray attenuation profiles are projected back for each individual projection angle. Here, the application of high-pass filters prior to the process of back projection into the image domain can effectively reduce the blur of examined objects, e.g., sharp convolution kernels are used to emphasize bone edges. Modern clinical CT systems increasingly draw on iterative reconstruction (IR) methods, which repeatedly approximate an image assumption to the measured dataset, more advanced methods further integrate statistical models (Willemink & Noel, 2019). Contrary to FBP, these methods do require more computational power but also decouple image noise and image sharpness, therefore providing both efficient denoising and substantial dose reduction (Geyer et al., 2015). Overcoming technical limitations pertaining to computation power, IR methods are nowadays routinely applied in clinical care and there is evidence suggesting a superior diagnostic image quality in various clinical scenarios, e.g., improved depiction of coronary anatomy in cardiac CT (Yoo et al., 2013) and effective dose reduction in obese patients (R. Wang et al., 2012).

As individual voxels are irradiated from numerous projections, eventual CT images lack projection-related overlays, which facilitates the spatial delineation of structures in all three dimensions. However, the extensive data acquisition is accompanied by substantial radiation dose and, by now, the relevance of strategies for optimal dose management has been known for a while in the radiological community (Frush, 2004). Although there is no reliable prospective data on biological effects of radiation doses below 100 mSv, diagnostic x-ray imaging and particularly CT accounts for a substantial share in civilizational radiation exposure (Hendee & O'Connor, 2012). This circumstance not only calls for a clear medical indication by a qualified radiologist but also underlines the importance of retrieving maximum diagnostic information from conducted examinations, which is the objective of opportunistic imaging.

1.1.3 Application of contrast media

Even though imaging of soft tissues is free of superimpositions and therefore superior to conventional radiography, low contrast of different soft tissues with similar mass attenuation values is a substantial shortcoming of CT. The application of contrast agents can improve spatial delineation of anatomic structures and pathologies and is therefore regularly used in various clinical situations such as tumor screening or angiography. Contrast agents can be applied via several administration routes: intravenous, oral, rectal, intrathecal, transurethral, etc.

At the molecular level, x-ray contrast media usually contain iodine and therefore are substances with high molecular weight or rather high effective atomic number. In comparison

with most other body tissues, iodinated contrast agents positively enhance image contrast through an intensified attenuation of x-ray photons depending on their concentration (Solbak et al., 2020), which is mainly attributable to photoelectric absorption.

For intravascular application, a contrast agent power injector conduces the administration of a prewarmed medium with a predefined volume and flow rate, hereafter flushing the vascular access with an isotonic saline chaser bolus.

Hypersensitivity reactions including the feeling of heat at the injection site, metallic taste, or local skin reactions can occur after intravascular application as well as contrast extravasation. Furthermore, intravascular contrast agents may evoke adverse clinical events and cause or aggravate renal failure, hyperthyroidism, or allergic reactions (severe skin reaction, bronchospasm, anaphylaxis, circulatory failure) (Beckett, Moriarity, & Langer, 2015; Singh & Daftary, 2008). Thus, the use of iodinated contrast agents is contraindicated in patients with the beforementioned conditions.

1.1.4 Dual-energy computed tomography

Dual-energy computed tomography (DECT) is a particular CT technique using two separate x-ray photon energy spectra for image generation. In contrast to conventional polychromatic CT, DECT exploits the specific attenuation behavior of materials at different x-ray energy levels providing information on differential attenuation of the x-ray spectrum within the patient´s body. Of note, the basic principles of DECT date back to the very early days of CT and have already been described by Godfrey Hounsfield in 1973 — almost simultaneously with the first introduction of CT itself (Hounsfield, 1973):

> *“Two pictures are taken of the same slice, one at 100 kV and the other at 140 kV. […] One picture can then be subtracted from the other by the computer so that areas of high atomic numbers can be enhanced. […] For example, tests carried out to date have shown that iodine (z = 53) can be readily differentiated from calcium (z = 20).”*

Soon after, Alvarez and Macovski developed the mathematical background for material decomposition using line integrals. As already briefly outlined in a previous section, both principal interactions with matter, photoelectric absorption, and Compton effect have different energy dependencies. At a certain energy level, the mass attenuation coefficient of an individual voxel can be regarded as the summation of absorption and scattering (Alvarez & Macovski, 1976):

$$\mu(E, Z, \rho) = (a_{ph}(Z) f_{ph}(E) + a_c(Z) f_c(E)) \times \rho$$

The basic principle of spectral imaging is to exploit this unique energy-dependency of mass attenuation coefficients at different energy levels, which allows for inferences on tissue composition, e.g., differentiation of materials or tissues that otherwise would have similar attenuation values in conventional CT — the basis for advanced applications like material quantification or decomposition. Interestingly, even the potential of DECT for quantification of bone mineral density (BMD) was recognized shortly after its initial description (Genant & Boyd, 1977).

Nevertheless, it took a long time for DECT to become available for clinical applications due to technical barriers. Nowadays, there are various vendor-specific configurations of DECT regarding image acquisition, of which most pursue a source-based approach. Dual-source CT (DSCT), for instance, features two separate x-ray sources of different tube potential (e.g., 80 and 140 kVp) including their associated detector, which are arranged in a nearly perpendicular orientation (McCollough, Leng, Yu, & Fletcher, 2015). Through the spatial offset of both tube-detector-arrangements, a ninety degrees rotation formally suffices for complete data acquisition and both acquisition systems can be adjusted individually. Thus, dual-source CT allows a high temporal resolution, being favorable for examinations of moving organs such as heart imaging (Flohr et al., 2006). However, this set-up also features constructive limitations: the secondary acquisition system is regularly designed with a smaller detector size which results in a reduced field of view for dual-energy use, and in conjunction with a helical acquisition mode, DSCT shows an incongruity of dual-energy raw projection data not allowing for material-decomposition in projection space (Patino et al., 2016). Besides, cross-scatter is another intrinsic drawback referring to misregistration of deflected x-rays on the non-associated detector, which increases noise and requires algorithms for correction (Petersilka, Stierstorfer, Bruder, & Flohr, 2010) and deteriorates separation of x-ray spectra. Contrary to that, rapid-kVp-switching CT refers to a set-up in which one x-ray source quickly alternates between two different tube potentials and high- and low-energy data are acquired in projection space with minimal time offset, but as a downside features technical limitations regarding an overlap of the high- and low-energy spectra (Garnett, 2020). Of note, both acquisition techniques must be selected prior to the examination, implying that opportunistic analyses of already acquired CT data are not possible. A newer technical solution, the detector-based dual-energy technique dual-layer spectral computed tomography (DLCT), is the object of this research work and is therefore addressed in detail in the Methods section of this thesis.

1.2 Clinical background

1.2.1 The human spine: structure and function

Being a central load-bearing element of the axial skeleton, the human spine provides important biomechanical functions regarding statics, the differentiated motion of the trunk as well as protection of neural structures (Galbusera, 2018). For the osseous part, it regularly consists of 24 individually articulating (cervical, thoracic, and lumbar spine) and 8 to 9 fused vertebrae (sacrum and coccyx), representing a complex system of superimposed bones with numerous connecting discoligamentary structures.

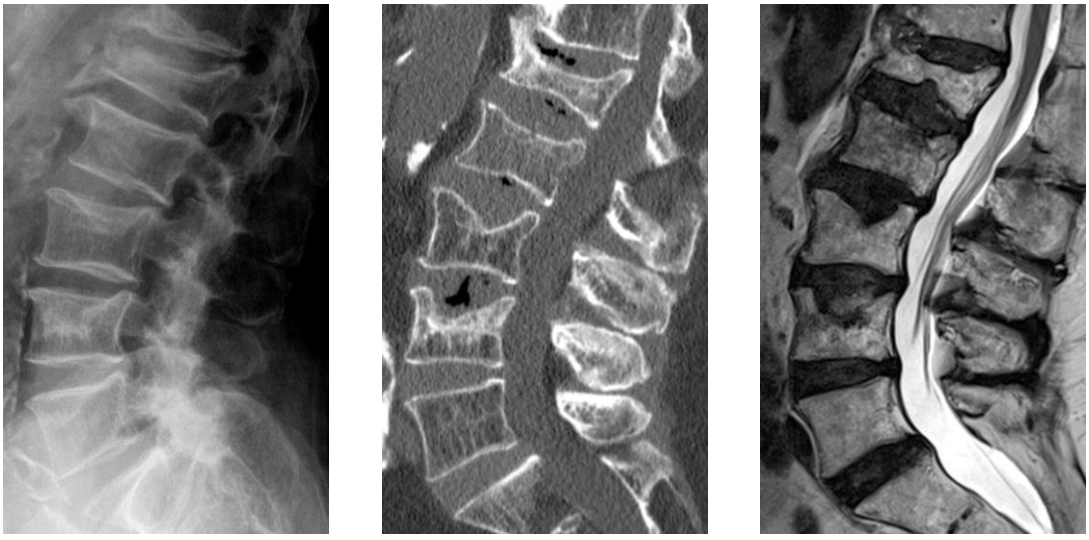

Figure 4: Bone structures of the human spine, conventional x-ray image in lateral view (left), sagittal reformation of computed tomography (middle) and magnetic resonance tomography (right).

Radiological techniques are a major element in the diagnosis of spinal disorders, however, the complexity in its structure and composition make imaging of the vertebral column challenging and often call for multimodal strategies. Macroscopically, a vertebral body features an internal structure of predominantly trabecular bone, a network of bony struts and plates, which is framed by a relatively thin shell of cortical bone, and the space in between being filled up with bone marrow (Briggs, Greig, Wark, Fazzalari, & Bennell, 2004). Generally, bone tissue chemically consists of approximately 60% inorganic (particularly calcium-hydroxyapatite) and 30% organic components (primarily collagen type I of the extracellular bone matrix) as well as 10% water (Feng, 2009); and being a natural composite is the foundation of its biomechanical strength regarding both compressive and tensile forces. Of note, BMD, as well as load, are not

evenly distributed across the vertebral bone: initial findings of ex-vivo studies suggested highly differentiated load-sharing of cortical and trabecular parts (Eswaran, Gupta, Adams, & Keaveny, 2006) as well as pronounced bone loss within rather anterior regions (Antonacci, Hanson, Leblanc, & Heggeness, 1997; Chen, Shoumura, Emura, & Bunai, 2008). Adams et al. explained this observation of reduced BMD in anterior vertebral regions with age-related intervertebral disc degeneration and an associated shift of axial load towards the posterior column, resulting in relative anterior unloading, concomitant net bone loss and structural alterations (M. A. Adams, Pollintine, Tobias, Wakley, & Dolan, 2006).

For biomechanical considerations regarding the spine and respective testing, the functional spinal unit (FSU), also referred to as spinal motion segment, is a well-established model and can be seen as the basic constructive element of the vertebral column. It is commonly defined as the sum of two adjacent vertebrae, the intermediate disc as well as connective ligaments (Iorio, Jakoi, & Singla, 2016). For the transfer of load across a FSU, non-linear relations between load and displacement were observed regarding various movement directions and on different spinal levels (Oxland, 2016). Furthermore, trabecular strength depends on the loading direction and differs for compressive, tensile, and shear forces (Keaveny, Morgan, Niebur, & Yeh, 2001). Exceeding its mechanical stability, however, regularly results in structural failure of an FSU, e.g., a vertebral fracture of the superior endplate. Intervertebral disc degeneration may aggravate this by altered load distribution and further decrease the mechanical capacity pertaining to compression loads (Hansson, Keller, & Spengler, 1987). In this context, the three-column-spine by Denis et al differentiating an anterior, middle, and posterior spine became an established concept in clinical care providing a possibility for a more in-detail vertebral fracture evaluation and pointing out the particular importance of middle column integrity for overall spinal stability (Denis, 1983).

Besides osteoporosis and trauma, the human spine is subject to several other pathologic changes. Age-related degenerative processes (e.g., osteoarthritis, spinal stenosis, intervertebral disc degeneration and herniation) are of tremendous clinical significance and regularly compromise the structural integrity of FSUs, as well being associated with chronic pain, functional impairment, or reduced health-related quality of life (Montazeri, 2010).

1.2.2 Osteoporosis and fragility fractures

A common definition by the US-American National Institute of Health (NIH) focuses on two key aspects of the systemic bone disorder osteoporosis: a compromised bone strength as an expression of both quantitatively reduced bone density and restricted bone quality (e.g., by changes in trabecular architecture, decreased rate of bone turnover or accumulation of

microfractures etc.) as well as a consequential susceptibility for fractures (NIH Consensus Development Panel on Osteoporosis Prevention & Therapy, 2001).

From an epidemiologic perspective, osteoporosis remains a highly morbid disorder with substantial socioeconomic impacts on health care systems. For the European Union (EU27), the prevalence of osteoporosis was estimated at 22 million for women and 5.5 million for men in 2010, accounting for a total societal cost of 37 billion Euro, which in large part is attributable to the treatment of 3.5 million new fragility fractures (Hernlund et al., 2013). Comparable extrapolated data from 2016 revealed a somewhat lower prevalence of 4.4% (3.61 million) for Germany with about 259,000 fractures per year related to osteoporosis as well as a marked treatment gap of 63% (Hadji et al., 2020). Across the globe, approximately 9 million fragility fractures are attributable to osteoporosis, and for Europe, even more disability-adjusted life years are lost due to osteoporosis (2.0 million) rather than colorectal or breast cancer (1.9 and 1.7 million, respectively) (Johnell & Kanis, 2006). Yet it is these incident fragility fractures causing significant excess mortality to affected patients (Cauley, Thompson, Ensrud, Scott, & Black, 2000; Morin et al., 2011). Looking forward, both the predicted growth of the global population and the ageing in developed and developing countries (United Nations, 2019) are likely to aggravate the economic burden on societies by increasing case numbers. Therefore, prevention and management of osteoporosis are expected to gain relevance for health care systems in the future.

In this context, two principal types of osteoporosis are commonly distinguished: Primary osteoporosis occurs in the course of physiological aging processes and refers to both postmenopausal osteoporosis with estrogen deficiency leading to accelerated bone loss and senile osteoporosis being characterized by a gradual age-related loss of bone strength (Herold, 2019). In secondary osteoporosis, excess bone loss arises because of an underlying disease or as an adverse drug effect. Secondary causes for osteoporosis comprise endocrine conditions like hypercortisolism or hypogonadism, malabsorptive conditions (Seo, Kang, & Choe, 2018) as well drug-induced osteoporosis due to long-term above-threshold therapy with glucocorticoids (Baylink, 1983) or proton-pump inhibitors (Fraser et al., 2013; van der Hoorn, Tett, de Vries, Dobson, & Peeters, 2015), aromatase inhibitors (Eastell et al., 2006) or androgen-deprivation therapy (ADT) (Basaria et al., 2002).

Even more than for this variety in types, the individual etiologies of osteoporosis are legion. Multiple clinical risk factors for osteoporosis have been identified causing accelerated bone loss and negatively influence bone strength. These include unmodifiable demographic factors such as age, female sex, and white ethnic origin as well as modifiable nutritive or lifestyle-associated factors, e.g., low body mass index (BMI), low calcium intake, low vitamin D levels, smoking, excessive alcohol consumption or physical inactivity (J. A. Kanis et al., 2005). Various conditions that lead to a deficiency of bone-anabolic sex hormones or to a

reduced duration of exposition contribute to low bone mineral density (Almeida et al., 2017). In turn, estrogen substitution has been shown to significantly reduce hip fracture rates in postmenopausal women (Anderson et al., 2004; Rossouw et al., 2002).

From a histological and cell-biological perspective, human bone tissue features some unique characteristics. Its turnover is mediated by two specific bone cells effecting formation and degradation: osteoblasts and osteoclasts. The biomechanical properties of bone, in particular the mechanical strength towards compressive, shear and torsion stress are in large part reflected by the composition and configuration of the extracellular bone matrix (EBM), which is a composite of organic (type 1 collagen, glycoproteins, proteoglycans and others) and inorganic components, especially crystalline calcium hydroxyapatite (HA; $Ca_{10}[PO_4]_6[OH]_2$) (Lin, Patil, Gao, & Qian, 2020; Ramesh, Moratti, & Dias, 2018). Moreover, bone tissue also plays an important role as a depot for calcium and other mineral ions and, with trabecular parts hosting the bone marrow with its hematopoietic stem cells, as site of blood formation.

It is a well-known principle that the structure of human bone tissue is permanently subjected to adaptive remodeling along principal trajectories of mechanical stress (Wolff, 1892), which is also a key to understand the pathophysiology of osteoporosis: The remodeling is predominantly orchestrated by osteoblasts, which are under the regulating influence of systemic hormones (e.g., sex hormones, parathormone, calcitriol) and in turn mediate bone remodeling via a complex system of paracrine effector molecules, cytokines and growth factors. The membrane-bound proteins Receptor Activator of Nuclear Factor-κB (RANK) and its ligand (RANKL) are expressed by osteoclasts and osteoblasts, respectively, and constitute a fundamental signaling pathway that mediates the activation, differentiation and survival of osteoclasts, therefore promoting bone resorption (Boyle, Simonet, & Lacey, 2003; Jimi et al., 1999). The up-regulation of RANKL on osteoblasts has been shown to play a major role in increased bone resorption following peri- and postmenopausal estrogen-deficiency (Eghbali-Fatourechi et al., 2003). Other soluble factors like the osteoblast-secreted Macrophage colony-stimulating factor (M-CSF) or osteoprotegerin likewise influence osteoclast development and therefore resorptive activity, with the latter acting as a functional antagonist to the RANK/RANKL-pathway (Rachner, Khosla, & Hofbauer, 2011; Simonet et al., 1997). Moreover, osteoclastic activity is supposed to feed back bone formation, conceptually referred to as “coupling”, as the resorption of EBM may release matrix-bound growth factors (Daci et al., 2003). In physiologic state and under steady mechanical load, bone formation and bone resorption are two well-balanced, sequential subprocesses serving the repair of microdamage as well as the regulation of calcium homeostasis (Suttorp, 2020). If bone resorption outweighs bone formation as in osteoporotic patients, a net decrease of bone mass results as well as concomitant structural alterations. The consequentially impaired structural integrity leads to diminished mechanical strength and predisposes patients to fragility fractures. As mentioned

earlier, in-vitro data suggest a substantial spatial intravertebral variability regarding bone mineral density and histomorphometrical parameters (e.g., trabecular thickness, number or separation) along the sagittal and vertical axis, causing a relative structural weakness in the upper and the anterior half of a vertebral body (Banse et al., 2001; Chen et al., 2008). Besides this structural heterogeneity, two further characteristics have to be considered for a more advanced understanding of failure mechanisms and fracture behavior: its anisotropy and asymmetry, i.e. trabecular strength both depends on the loading direction and differs for compressive, tensile and shear forces (Keaveny et al., 2001). Early on, it has been perceived that sole quantification of bone mass cannot fully explain biomechanical competence of trabecular bone: a series of experimental studies with varying approaches indicates that the functional relation between trabecular BMD and bone strength (e.g. approximated as maximum compressive stress) is more of a nonlinear nature (Boehm et al., 2003; McBroom, Hayes, Edwards, Goldberg, & White, 1985; Mosekilde, Mosekilde, & Danielsen, 1987). This points to the multifactorial origin of bone strength and signifies other factors beyond low BMD contributing to bone fragility. Also, a substantial part of fracture burden weighs on non-osteoporotic patients, having either normal BMD or low bone mass above the BMD threshold for osteoporosis (Bliuc, Alarkawi, Nguyen, Eisman, & Center, 2015). Although research efforts aim for a better understanding of pathologic microstructural changes and other determinants of bone strength than BMD: by date, BMD remains the key diagnostic parameter in day-to-day clinical care when it comes to the diagnosis of osteoporosis.

As a great number of patients with osteoporosis has subclinical, asymptomatic fractures, an early and distinct diagnosis of osteoporosis is challenging. First off, a comprehensive osteoporosis work-up comprises the patient's medical history and a proper clinical examination with focus on clinical risk factors, fracture signs and possible neurological deficits. Then, morphological imaging plays a major role in the diagnosis and evaluation of spinal injuries. The significant role of dedicated compositional imaging in the management of osteoporosis, i.e., osteodensitometry, will be described in the next chapter. The initial standard imaging approach to fracture detection is a conventional X-ray study in two planes (anteroposterior and lateral projection). Here, a widely used classification for the evaluation of fracture severity is the Genant semiquantitative method, distinguishing three grades by relative vertebral height loss (Genant, Wu, van Kuijk, & Nevitt, 1993). Vertical striation due to a relatively quicker thinning of horizontal trabeculae (Thomsen, Niklassen, Ebbesen, & Bruel, 2013) may also be present as radiological finding suspicious of low BMD as well as accentuated endplates. When it comes to accurate and comprehensive fracture evaluation regarding preoperative planning, a CT examination with multiplanar reconstruction is an integral component of diagnostic algorithms, allowing for thorough assessment of bony structures, in particular the possible involvement of a vertebral body`s posterior wall. If patients

present with neurological symptoms, magnetic resonance imaging (MRI) allows for better evaluation of spinal soft tissues (e.g., spinal cord injuries, hemorrhage, ligament injuries, ruptured or herniated discs). Due to the high number of sub-clinical fractures, MRI is also regularly used for the differentiation of new and old vertebral fragility fractures when multiple fractures are present and may have occurred asynchronously. New fractures show a diffuse hyperintense signal in fat-suppression-sequences such as short TI inversion recovery (STIR) indicative for bone marrow edema (Link, 2016). Likewise, advanced CT imaging modalities that allow for material decomposition can facilitate the diagnosis of acute vertebral fractures based on dual-energy information (Schwaiger et al., 2018). Laboratory tests of biochemical markers of bone formation (e.g., bone-specific alkaline phosphatase) or bone resorption (e.g., pyridinium crosslinks in the urine) may provide a benefit regarding therapy monitoring but have rather limited clinical value in the diagnosis of primary osteoporosis (Cosman et al., 2014). However, specific laboratory examinations can demarcate differential diagnoses such as malign conditions (e.g., multiple myeloma, bone metastases), osteomalacia and primary hyperparathyroidism or contribute to the evaluation of secondary causes (Herold, 2019). Of note, degenerative changes and inflammatory processes like spondylodiscitis or epidural abscesses should be included in differential-diagnostic considerations as well.

The therapy of osteoporosis is multidimensional and complex. Thus, all aspects exceeding fundamental therapeutic principles, in particular details of pharmacological therapy, go beyond the scope of this thesis. Elemental goals of anti-osteoporosis therapy are the stop of further bone loss and the prevention of fractures. Fundamentally, the therapeutic strategy aims to address modifiable clinical risk factors and comprises both pharmacological and non-pharmacological interventions. First off, concurrently promoting physical activity and reducing fall risk can be challenging in this largely senior patient group. Potential secondary causes for osteoporosis obviously must be considered in therapeutic decisions as well as respective measures (e.g., reduction of glucocorticoids). Appropriate basic measures in osteoporosis therapy also comprise lifestyle changes (e.g., cessation of harmful habits like smoking or alcohol consumption) as well as the combined supplementation of calcium and vitamin D, which are fundamental components in bone formation. However, the results in studies on BMD or anti-fracture efficacy are inconsistent (Avenell, Mak, & O'Connell, 2014; Jackson et al., 2006; Zhao, Zeng, Wang, & Liu, 2017), and although being generally recommended for all postmenopausal women with increased fracture risk (J. A. Kanis et al., 2019), their beneficial effects may only be present in calcium and/or vitamin D deficient individuals. As for the more potent pharmacological mechanisms, osteoprotective medication either takes an antiresorptive or anabolic approach, i.e., through inhibition of bone resorption or induction of bone formation, respectively. The group of bisphosphonates represents the pharmacological first-line therapy in the prevention and treatment of osteoporosis, inhibiting the resorptive

activity of osteoclasts and thereby stopping excess bone loss and increasing BMD. Several phase III clinical trials of alendronate, risedronate and zoledronic acid have proved their ability to increase BMD and reduce the incidence of vertebral and nonvertebral fractures in postmenopausal women with low bone mass (Black et al., 1996; Black et al., 2007; Harris et al., 1999; Liberman et al., 1995). For ibandronate, only a reduction of vertebral fractures has been shown (Chesnut et al., 2004). Potential adverse effects are seen pertaining to the gastrointestinal system (esophagitis, dyspepsia, reflux), atypical fractures (Lenart, Lorich, & Lane, 2008; Shane et al., 2014) and — relatively rare — osteonecrosis of the jaw (Khan et al., 2015). Denosumab is a human monoclonal antibody that inhibits bone resorption by targeting RANKL, thereby increasing both vertebral BMD and hip BMD (Bone et al., 2008). Moreover, in postmenopausal women with low bone mass, denosumab proved its anti-fracture efficacy by reducing the risk for vertebral fractures by 86%, for hip fractures by 40% and for non-vertebral fractures by 20% (Cummings et al., 2009). Other large-scale clinical trials have further shown that denosumab increases the BMD of patients taking aromatase-inhibitors against breast cancer (Ellis et al., 2008) or receive ADT against prostate cancer (Smith et al., 2009). Pharmacological therapy with a selective estrogen-receptor modulator (SERM), e.g., raloxifene can likewise slow down excess bone loss. A risk reduction for vertebral fractures has been shown for raloxifene as well as an increase in vertebral BMD (Ettinger et al., 1999). Its influence on BMD improvement and biomarkers of bone turnover, however, is substantially less pronounced compared to alendronate (P. N. Sambrook et al., 2004). Furthermore, the use of raloxifene is limited by adverse effects such as venous thromboses and fatal cerebrovascular complications (Barrett-Connor et al., 2006), its application therefore may not be compatible in patients with elevated risk for these conditions. Opposed to the above agents, the recombinant N-terminal fragment of human parathyroid hormone (PTH 1-84) teriparatide (rhPTH 1-34) is an osteoanabolic substance that enhances bone formation, with positive effects on BMD and reduction of fracture risk (Neer et al., 2001). However, therapy is limited to 24 months and regularly requires subsequent antiresorptive pharmacotherapy, e.g., with bisphosphonates.

Fractures are the most frequent adverse clinical outcome of osteoporosis. They are regularly causing pain and functional impairments such as constrained range of motion. The typical sites of osteoporosis-associated fractures are the spine, the hip, the distal radius and the proximal humerus (J. A. Kanis et al., 2001), commonly referred to as major osteoporotic fractures. It is a simple, yet remarkable observation that all these sites are predominated by trabecular bone. Vertebral fragility fractures show an exponential rise in the distribution of age-specific incidence for both women and men (P. Sambrook & Cooper, 2006). Besides, they are also commonly associated with adjacent fractures, height loss and progressive kyphotic deformation (Kado 2013, Huang 2014) causing sagittal imbalance, which in turn increases the

tendency to fall. Two principal trauma situations must be distinguished regarding osteoporosis-associated fractures: fragility fractures comprise spinal deformation due to low-energy traumata, i.e., with insignificant trauma kinetics (e.g., fall from less than stand height) and even spontaneous fracture. Owing to the diminished biomechanical capacity of osteoporotic bone, relatively less impact force suffices to induce spinal deformation and fractures are more likely to occur following adequate high-energy traumata (e.g., traffic accident, fall from height). Of note, as these two trauma types represent the ends of a continuum, transitions between both are flowing and distinct classification is therefore often difficult. Still, the leading fracture cause is often pivotal for appropriate treatment. Most osteoporosis-associated fractures affect the thoracolumbar junction (T12-L2) and, to a lesser extent, the middle thoracic spine (T7-T9) (Van der Klift, De Laet, McCloskey, Hofman, & Pols, 2002). Basically, these fractures can be classified according to the AO Spine Thoracolumbar Spine Classification System which assigns spinal injury patterns to three leading trauma mechanisms: compression (type A), distraction (type B) and translation injuries (type C) (Vaccaro et al., 2013). In the course of trauma, individual fracture patterns result from particular force vectors and moments that exceed regional bone strength and biomechanical capabilities of a vertebra (Christiansen & Bouxsein, 2010). Pertaining to fracture treatment, the range of options comprises both non-operative and operative approaches and fracture assessment regarding sufficient biomechanical stability is guiding for the further therapeutic path. Here, the involvement of the vertebral body`s posterior wall is generally considered as a key indicator for instability in spinal type A injuries. Fragility fractures are often a consequence of either traumatic axial compression or hyperflexion with compressive forces acting on the anterior column and concurrent distractive forces on the posterior column. Compression fractures of the subtypes A0 to A2 (non-structural, wedge/impaction, split fracture) are mostly stable injuries and can regularly be addressed with non-operative therapy, multifactorial care concept embracing symptom-oriented analgesia, anti-osteoporotic medication as well as early physiotherapeutic mobilization. In contrast, vertebral fractures of subtypes A3 and A4 are often, type B or C fractures yet by definition, instable injuries requiring surgical treatment. Contrary to trauma of healthy vertebral bone, however, osteoporosis-associated fractures confront medical practitioners with specific biomechanical properties that call for a differentiated therapeutic strategy. Generally, surgical efforts aim for creating a situation of high primary biomechanical stability for both pain relief and early postoperative mobilization. The selection of appropriate treatment options depends on the fracture type, localization, and several patient-related factors (e.g., bone quality, therapy adherence, etc.). Minimally invasive procedures such as vertebroplasty and kyphoplasty accomplish an augmentation of fractured vertebral bodies through bone cement. Spinal instrumentation is usually performed with a system of posteriorly inserted, fixed-angle pedicle screws and longitudinal rods, traversing at least two spinal

segments. As the reduced bone strength in osteoporotic bone results in poorer anchoring of implants, the above-mentioned procedures are sometimes combined to hybrid osteosyntheses to prevent bone-implant interface failures (e.g., screw loosening, cut out), e.g., by additional cement augmentation of pedicle screws.

1.2.3 Fracture risk assessment: Bone densitometry, clinical risk factors and other imaging biomarkers

Quantitative osteoporosis imaging or bone densitometry, i.e., a noninvasive technique to assess bone mineral density, is regularly used in clinico-radiological routine for the detection of excess bone loss, the identification of high-risk individuals for fracture or the monitoring of pharmacological osteoporosis treatment. The diagnosis of osteoporosis is either based on markedly reduced BMD values or on the clinical appearance of fragility fractures in synopsis with risk factors. In a clinical context, dual-energy x-ray absorptiometry (DXA) and, to a lesser extent, quantitative CT (QCT) are the best-established imaging modalities regarding application and availability.

Dual-energy x-ray absorptiometry (DXA) is an imaging technique based on two x-ray spectra of different energy levels and represents a projection-based method that measures BMD as grams of mineral per area (g/cm^2). Typical sites for BMD measurements with central DXA are the lumbar spine (L1-L4) and the proximal femur, each in posteroanterior projection. In 1994, the World Health Organization (WHO) operationally defined an international diagnostic reference standard for osteoporosis in women: BMD values at the femoral neck being 2.5 standard deviations (SD) or more below the mean BMD of a young, healthy, white and female reference population are considered to indicate osteoporosis (WHO, 1994). According to the International Society for Clinical Densitometry (ISCD), osteoporosis may likewise be diagnosed if T-scores derived from the total hip or at the lumbar spine are -2.5 SD or less (ISCD, 2019). T-scores between -1 and -2.5 SD constitute low bone mass and were formerly referred to as osteopenia. For BMD reporting, ISCD guidelines recommend the use of T-scores for postmenopausal women and for men aged 50 years or older, whereas for premenopausal women, younger male adults or children, a Z-score reference database should be used as it allows for age-, gender- and ethnicity-matched BMD comparisons (ISCD, 2019). As for the relative distribution of BMD, the main fracture burden weighs on the patients diagnosed with low bone mass, even though patients with osteoporosis have the highest individual risk for fracture (Schuit et al., 2004; Stone et al., 2003). DXA is the standard technique used tool for BMD assessment in routine clinical care. Besides, additional information can be extracted from DXA scans such as the trabecular bone score (TBS), aiming for textural analysis of the trabecular microstructure (Oei, Koromani, Rivadeneira, Zillikens, & Oei, 2016). Its main benefits are high reproducibility (Lodder et al., 2004; Lohman, Tallroth,

Kettunen, & Marttinen, 2009) and very low effective doses of 3 to 17 μSv (Blake, Naeem, & Boutros, 2006), depending on various factors such as the patients' size, scan length, the tube current, the tube potential, etc. However, DXA is also subjected to inherent limitations constraining its diagnostic value. Due to its projection-based measuring approach, only areal BMD can be obtained, which is prone to bone size and can therefore lead to an overestimation of actual fracture risk in smaller individuals (Link, 2012). Concurrently, degenerative changes of the spine such as osteophytes or soft tissue calcifications, e.g., within the aortic wall, lying in projection of transmitting x-rays can lead to measurement errors that result in falsely high BMD values (Link, 2016). The extent of body fat has also been shown to substantially influence the accuracy and reproducibility of DXA measurements and must be taken into consideration when interpreting respective BMD values (Yu, Thomas, Brown, & Finkelstein, 2012).

Quantitative computed tomography (QCT) is an alternative clinically well-established modality to measure BMD at the spine or hip in a dedicated way with use of x-rays. It generally operates in single-energy mode with a synchronously — i.e., in the same examination — scanned calibration phantom and, using dedicated software for analysis, allows the translation of CT numbers to density values expressed as mass of mineral per bone volume [mg/cm^3] (Brett & Brown, 2015). Contrary to the planimetric approach of DXA, QCT enables exclusively trabecular volumetric BMD (vBMD) measurements in cross-sectional images that are free of superimposition. This focused assessment of the metabolically more active trabecular compartment represents a major advantage of QCT, potentially enabling an early detection of disease- or treatment related BMD changes (J. E. Adams, 2009). As for the spine, the quantitative assessment of bone density usually comprises the segments L1 to L3, with single acquired slices or helical three-dimensional data (3D QCT) (Engelke, 2017). In order to approximate WHO diagnostic categories for DXA, the American College of Radiology (ACR) suggested to classify BMD values of 120 mg/cm^3 or more as normal, values between 120 and 80 mg/cm^3 as osteopenic and those below 80 mg/cm^3 as osteoporotic (ACR, 2018). In many ways, volumetric BMD assessment with QCT overcomes possible measuring inaccuracies of DXA that are caused by dependency of bone size or projection, e.g., influences of spinal or vascular degenerations. Several studies suggested the ability of vBMD at the lumbar spine for predicting incident vertebral fractures and therefore allowing for vertebral risk assessment (Kopperdahl et al., 2014; X. Wang et al., 2012), besides allowing for more advanced assessment of bone strength, e.g., via finite element analysis (FEA) (J. E. Adams, 2009). However, the clinical use of this dedicated quantitative imaging method is still limited by restricted availability, higher examination costs as well as a relatively high radiation exposure levels with effective doses for spinal and femoral 3D volumetric QCT ranging from approximately 1.5 to 3 mSv (Engelke et al., 2008). QCT measurements have been shown to

be less affected by body fat than DXA, albeit a certain fat-associated error were detected here, too (Yu et al., 2012).

Other dedicated approaches to assess either bone density or bone quality are peripheral dual-energy x-ray absorptiometry (pDXA), (high-resolution) peripheral quantitative computed tomography ([HR-]pQCT), and quantitative ultrasonography (QUS). The modalities pDXA and pQCT basically represent the application of above-described x-ray-based BMD measuring techniques at peripheral skeletal sites but have never gained the same degree of establishment in clinical use. HR-pQCT with a special CT scanner type is an imaging method providing a higher spatial resolution (130 – 160 µm) than clinical whole-body CT scanners and enables to concurrently measure BMD as well as assess trabecular architecture in peripheral appendicular bones (e.g., radius, tibia) (J. E. Adams, 2009; Burghardt et al., 2013). Without exposure to radiation, QUS can indicate low bone quality as found in osteoporosis by detecting characteristics such as decreased velocity of ultrasound transmission and increased signal amplitude (Link, 2016). This method is known to provide fracture risk prediction largely independent of BMD (Gluer, 2008). Except for QUS which is applied in some care settings, however, these techniques are currently of very limited relevance in clinical use.

International guidelines recommend BMD screening for all women aged 65 years or older and men aged 70 years or older – younger postmenopausal or perimenopausal women as well as men between 50 and 69 years should be assessed for BMD only in presence of specific clinical risk factors (including low body weight, prior fracture or high-risk medication use); moreover, BMD testing is recommended for all adults with a fragility fracture, any condition or medication use associated with bone loss or low bone mass as well as candidates for pharmacologic therapy or therapy monitoring (ISCD, 2019). German national osteoporosis guidelines propose a risk-based approach and recommend the use of central DXA (spine and hip) as BMD tool along with further basis diagnostics for all individuals exceeding a 10-years-fracture risk of 20% on the base of a self-developed model integrating multiple risk factors (DVO score); they further recommend fracture risk evaluation for all patients of 50 years and above who sustain a fragility fracture as well as those with clinical risk factors (Dachverband der Deutschsprachigen Osteologischen Fachgesellschaften, 2017). Both guidelines generally prefer central DXA measurements as standard technique over vertebral or hip QCT, which are not recommended for routine clinical use, inter alia, due to a lack of prospective studies and standardized reference data (Dachverband der Deutschsprachigen Osteologischen Fachgesellschaften, 2017; ISCD, 2019).

Contrary to the above-mentioned imaging approaches dedicated to osteodensitometry, opportunistic osteoporosis CT imaging refers to the use of body CT examinations originally performed for other clinical indications. In the context of osteoporosis imaging, the term opportunistic screening subsumes a wide range of methodical approaches, whose common

ground is the absence of an in-scan calibration phantom for converting CT attenuation to BMD values by means of materials with known densities. Asynchronous external calibration refers to BMD assessment in which the CT scans of the calibration phantom and the clinical patient scans are temporarily separated (Brown et al., 2017), in part with phantom measurements averaged over multiple scans. With this method, CT attenuation values of trabecular bone are calibrated to prespecified reference materials of known densities comparable to dedicated volumetric QCT, briefly called HU-to-BMD conversion. Although overall measurement precision has been shown to be on a par with formal QCT (Kaesmacher, Liebl, Baum, & Kirschke, 2017), the time interval between BMD measurement and calibration may open the possibility for measurement inaccuracies related to CT scanner instabilities (Engelke et al., 2015). As for vertebral density measurements, internal calibration methods employ CT attenuation values of closely adjacent soft tissues (commonly paraspinal muscle and subcutaneous fat) for calibration purposes regarding BMD, using information derived from analysis of histogram peaks (Boden et al., 1989; Mueller et al., 2011). Pickhardt et al concluded a promising potential as a diagnostic tool to screen for low BMD with the internal calibration method a in the context of CT colonography, using DXA as reference standard (Pickhardt et al., 2011). However, a study by Mueller et al. suggest inferiority compared to phantom-based approaches regarding reproducibility of measurements (Mueller et al., 2011). Intravascular iodine contrast application influences both above-mentioned screening approaches as attenuation values of measured vertebral regions of interest (ROI) will increase and therefore lead to incorrect BMD values as ROIs for calibration remain either unaffected (asynchronous calibration) or presumably change unequally (internal calibration), suggesting the need to adjust for iodine contrast effects (Kaesmacher et al., 2017). Overall evidence on the clinical value of internal calibration is still rather limited with a thorough analysis of Engelke et al. addressing several uncertainties regarding dependence of the calibration method on certain CT protocol parameters, possible inaccuracies attributable to tissue alterations such as muscle atrophy or fat as well as lack of validation data with external cohorts (Engelke et al., 2015).

Opportunistic CT-based screening methods for low BMD also comprise the plain use of HU values, e.g., of the first lumbar vertebral body (L1), representing a very simple and practicable approach. Even though attenuation values of whole-body CT scanners across different manufacturers and devices are calibrated to water as standard, considerable variation in CT attenuation values was found regarding measurements of identical HA inserts (Engelke et al., 2015). A study by Pickhardt et al. investigated L1 attenuation as surrogate for lumbar BMD and concluded HU to be an effective method to screen for low BMD using DXA as standard of reference (Pickhardt et al., 2011). Recently, a large study investigating more than 20,000 CT examinations in adults provides reference data on L1 attenuation values at 120 kV for different age groups; it is ambiguous, however, that a considerable sub-cohort of 4263

patients with contrast-enhanced examinations did not show significant differences in attenuation values, particularly in older age subgroups (Jang et al., 2019), although intravascular contrast has previously been shown to increase L1 attenuation (Pickhardt et al., 2016). Other data from 1966 adults older than 65 years suggest an association of L1 attenuation to vertebral fractures with values lower than 90 HU being indicative for high fracture risk (Graffy, Lee, Ziemlewicz, & Pickhardt, 2017). In general, the requirement of scanner-specific comparative data for HU values currently limits broad clinical application. Despite, international guidelines list simple HU measurements of the first lumbar vertebra as an option to facilitate clinical decision-making with regard to the need of further bone assessment, with HU < 100 and HU > 150 representing the relevant cut-off values for indicating high or low fracture risk (ISCD, 2019). Yet, practical implications for patients with intermediate HU measurements remain unclear. A thorough review on HU-based screening for low BMD remains critical on the lack of consistency across different CT scanners and missing data on predicting fracture risk for approximating bone quality (Gausden, Nwachukwu, Schreiber, Lorich, & Lane, 2017). Still, the method could prove valuable when applied as a screening tool to at-risk populations, given that all physicians involved are aware of the intrinsic limitations (Schwaiger, 2022).

For a more comprehensive evaluation of fracture risk beyond that provided by BMD measurements, the integration of easily obtainable and independent clinical risk factors proved to enhance the overall prediction accuracy regarding fracture incidence (J. A. Kanis et al., 2007). In this context, the Fracture Risk Assessment Tool (FRAX®) has become a commonly used model for fracture risk prediction and provides clinicians with an absolute 10-year risk of either hip fracture or major osteoporotic fracture (clinical vertebral, distal forearm, hip or humerus) with or without BMD measurement. It was validated with country-specific fracture databases and aims to guide clinical decision making, respectively, regarding therapeutic or preventive initiation of pharmacological intervention. For this, the algorithm includes inter alia: patient age, sex category, prior history of fragility fracture, low body mass index, life habits like current smoking status and excess consumption of alcohol as well as chronic use of glucocorticoids. Being constructed from population-based cohorts, however, this estimation model is subject to inherent limitations that may lead to misestimation of fracture risk or restricted applicability: dose-dependent risk factors such as smoking, alcohol consumption or glucocorticoid use and continuous variables as for multiple sustained fractures are only modelled in binary categories (J. A. Kanis, Johnell, Oden, Johansson, & McCloskey, 2008; Van Staa et al., 2003), the known influence of the vertebral fracture severity on future fracture risk is not accounted for (Delmas et al., 2003), there is lack of validation in certain ethnic minorities within a population (J.A. Kanis, 2007) and the FRAX® tool is restricted to femoral neck BMD or T score measured with DXA as an input variable – implying that adjustments

must be made for clinical cases with large offset between lumbar and femoral neck BMD (International Society for Clinial Densitometry, 2010).

Apart from sheer morphological imaging using tomography, magnetic resonance imaging (MRI) further provides more advanced quantitative techniques for musculoskeletal applications that may be useful for advanced diagnostics of bone loss and associated changes in bone marrow composition (Karampinos et al., 2018). In this context, magnetic resonance sequences like proton density fat fraction (PDFF) or T2* mapping are rapidly evolving and increasingly investigated in scientific studies. Although not yet established in clinical practice, these tools can help investigating tissues with a significant fat fraction such as vertebral bone. In individuals with low bone mass, for example, PDFF maps of the vertebral bone marrow can be created employing chemical shift encoding-based water-fat separation and suggest providing additional information on vertebral bone strength beyond BMD (Gassert et al., 2022). Another imaging-based surrogate biomarker using chemical shift encoding-based water-fat separation is bone marrow T2*, which has shown significant correlations with trabecular parameters of bone microarchitecture and therefore may be helpful in a quantitative analysis of lumbar osteoporosis as well as respective fragility fractures (Leonhardt et al., 2021).

1.3 Thesis purpose

Over the last decade, significant advancements were made in the field of dual-energy computed tomography. Novel imaging techniques like DLCT may facilitate BMD assessment by combining the advantages of dual-energy and volumetric measurements. Beforehand phantom studies demonstrated the potential of DLCT for accurate BMD measurements without the need for synchronous in-scan calibration (Mei et al., 2017; van Hamersvelt et al., 2017), paving the way for opportunistic screening for low BMD. However, its significance for osteoporosis assessment *in vivo* in patients acquired during day-to-day clinical care remained largely indeterminate and — with BMD still being the major diagnostic parameter for osteoporosis (Lochmuller et al., 2008) — the focus of this research work was to evaluate this novel dual-energy CT technique in a clinical context for possible application regarding quantitative musculoskeletal imaging. In detail, the objective of the conducted studies was to assess the clinical utility of DLCT regarding opportunistic screening for patients with low BMD of the spine. In this connection, opportunistic osteoporosis screening refers to the use of pre-existing clinical CT scans for the diagnosis of low BMD and consequentially increased susceptibility for fracture. Hence, opportunistic BMD testing could spare patients additional radiation exposure caused by dedicated examinations, which would be particularly relevant for patients that undergo serial BMD measurements. Accordingly, making use of opportunistic BMD may be beneficial in various clinical situations such as screening in at-risk cohorts, longitudinal assessment of age- or disease-related BMD changes, also as part of therapy monitoring, since treatment-related BMD changes were demonstrated to be a surrogate for fracture risk reduction (Black et al., 2020). Likewise, other clinical scenarios, e.g., patients with traumatic vertebral fracture and suspect bone strength being preoperatively planned for spinal instrumentation, may benefit from the opportunity of post-hoc BMD testing based on CT studies that are not specifically dedicated to osteodensitometry. This is based on the premise that opportunistic DLCT-based measurements support clinical radiologists in reaching an accurate diagnosis of conditions with low BMD, thus providing an additional diagnostic value and help optimizing the management of musculoskeletal disorders. Both presented journal publications are intended to evaluate the clinical potential of non-dedicated DLCT imaging for opportunistic BMD measurements in patients recruited during clinical routine. Hence, investigating the accuracy and diagnostic value of this approach to quantitative BMD assessment has been the leading objective interconnecting both research articles. Thereby, the first article (J-I) focuses on the translation from pre-clinical phantom studies to native *in-vivo* measurements based on phantomless non-dedicated, non-contrast-enhanced DLCT examinations and their comparison with volumetric QCT osteodensitometry. Building on this, the second article (J-II) evaluates the potential of DLCT for a quantitative phantomless BMD assessment with contrast-enhanced examinations, integrating a correction for the influence of intravascular iodinated contrast agent.

2 Methods

2.1 Dual-layer spectral computed tomography

Over the past decades, particularly CT imaging has seen considerable improvements in scanner performance and image quality. The clinical introduction of a novel detector technology using two superimposed detector elements in 2016 marked a milestone in the development of dual-energy CT. Since all imaging data included in this research project was generated on a commercially available dual-layer spectral CT scanner (Philips IQon Spectral CT, Philips Healthcare, Best, The Netherlands), a conceptual overview of its basic setup and functional principles is outlined in the following.

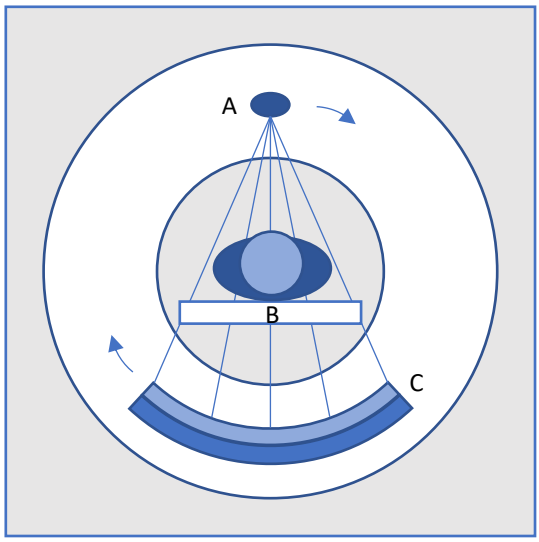

Figure 5: Schematic diagram of the dual-layer computed tomography scanner setup.

Spectral DLCT imaging is an advanced CT technology using a single x-ray source (120 or 140 keV), distinguishing itself from conventional CT particularly by its layered detector setup (Fig. 5, C) with different energy-sensitivities being reflected by different material properties: The top layer detector, which is closer to the x-ray tube, features a yttrium-based scintillator and predominantly registers low-energy photons whereas those with high energy mostly penetrate to hit the bottom-layer scintillator made of gadolinium-oxysulfide, each one coupled to a separate photodiode (Rassouli, Etesami, Dhanantwari, & Rajiah, 2017) (Fig. 5). Comparable to other DECT implementations such as dual-source or rapid kVp-switching CT, there is no absolute spectral separation in DLCT: scanning a 32-cm water absorber with a prototype scanner, Shefer et al. reported mean energies for both the low-energy and the high-energy spectrum of 73 keV and 95 keV (ΔkeV = 22 keV) at 140 kVp (Shefer, 2013), with graphical

representation of x-ray spectra indicating a certain spectral overlap. As for DLCT, however, the separation of the entire tube-side emitted x-ray spectrum into a low- and high-energy spectrum is made on the detector level. This offers in-depth information on x-ray attenuation beyond mass attenuation coefficients of conventional CT. The computational processing of the spectral information obtained thereby generates Spectral Base Images (SBI). On this base, the post-processing of spectral DLCT imaging allows for both computation of conventional polychromatic images as well as more advanced images using spectral information. Image series can be reconstructed in several ways for spectral visualization or analysis such as: virtual monoenergetic images (VMI) at x-ray energy levels from 40 to 200 keV and material decomposition images, e.g., virtual non-contrast images, iodine density maps (suppression of all non-iodine-containing-tissues, e.g. for iodine quantification) or effective Z maps (Romman, 2015). For the spectral reconstructions, the conceptual basis is to exploit the different energy-dependencies of photoelectric absorption and Compton effect. In detail, two separate basis images are reconstructed from low-energy (photoelectric effect) and high-energy raw data (Compton scattering) in the first place; afterwards, the basis images are linearly combined for the generation of VMIs, so that resulting images are analogous in image impression to those generated with a truly monoenergetic x-ray beam (Rassouli et al., 2017). Briefly, VMIs of the low-energy range accentuate the contribution of the photoelectric effect whereas reconstructed VMIs of the high-energy range lay emphasis on the part of image raw data originating from Compton scattering. Other spectral image types such as virtual non-contrast images (VNC) or iodine density maps, for instance, are based on the decomposition of the material basis pair water–iodine and either operate by suppression or quantitative visualization of iodine-containing voxels, respectively (Rajiah, Abbara, & Halliburton, 2017).

The key advantages of this detector-based approach to spectral imaging are evidently resulting from its specific detector setup: the spectral separation itself is only made after the x-rays transmitted the examined subject and, more to the point, without a relevant temporal or spatial offset. Amid awareness that mismatched raw data sets are detrimental in previous DECT realizations and need to be overcome (Maass, Baer, & Kachelriess, 2009), the simultaneous acquisition of spectral imaging data in the same projection solves this issue constructively by providing excellent alignment of recorded raw projection data (Patino et al., 2016). Due to the invariable acquisition of spectral information on the detector level, specifying a spectral CT protocol beforehand like in source-based DECT is not required by DLCT for individual clinical queries (Garnett, 2020), which facilitates clinicoradiological workflow. Moreover, the reconstruction and analysis of spectral information is always feasible retrospectively (Rassouli et al., 2017), forming the very basis on which opportunistic imaging concepts can take root in the field of DECT imaging. With dose management always being a critical issue in clinical radiology, the potential savings in patient exposure by reducing the

number of whole re-examinations or just single CT scan phases, e.g., by replacing true non-contrast (TNC) images with VNC images derived from contrast-enhanced DLCT (Ananthakrishnan et al., 2017) could be an additional benefit, that would also decrease diagnosis-associated expenses. Likewise, spectral imaging with DLCT features a substantial potential for dose reduction of applied iodinated contrast agent at a similar contrast-to-noise ratio by using low-energy VMIs (Nagayama et al., 2018; Tsang et al., 2017).

Specific spectral applications for musculoskeletal disorders meet a range of clinical enquiries, of which some have been traditionally challenging for unimodal imaging concepts. DLCT enables the detection of bone marrow edema for the evaluation of acute vertebral fractures as well as their differentiation from old fractures using MRI as standard of reference (Neuhaus 2018, Schwaiger 2018), suggesting its potential for sparing additional MRI scans as well as associated examination time and costs. Another domain of DLCT is to improve image quality by reducing metal or beam hardening artifacts with use of high-energy VMIs, e.g., for orthopedic hardware (Dangelmaier et al., 2018; Grosse Hokamp et al., 2018; Wellenberg et al., 2017), but also cardiovascular implants such as coronay artery stents (Hickethier et al., 2017; Qin et al., 2019) or port catheter systems (Laukamp et al., 2019). As for its advantages regarding the enhancement of vascular contrast and the reduction of radiation dose, dual-layer spectral detector technology might also be beneficial in other cardiovascular scenarios such as CT assessment prior to transcatheter aortic valve implantation or diagnosis or pulmonary embolism (Rajiah et al., 2017). Particularly relevant for its therapeutic implications, the evaluation of urinary calculi (Mansouri et al., 2015) is another common example and among the earliest clinical applications for material characterization with dual-energy CT. More recent studies have focused on the use of DLCT for the differentiation of intracranial hemorrhage vs. iodine contrast agent (Bernsen et al., 2021; Riederer et al., 2021).

2.2 Opportunistic phantomless in-vivo BMD measurements and iodine quantification

For a phantomless quantification of BMD, virtual monoenergetic images (VMI) were created at energy levels of 50 and 200 keV, using the dedicated software suite IntelliSpace Portal 10.1.0 (Philips Healthcare, Best, The Netherlands). Here, this wide spread of energy levels was chosen to ensure a clear split of spectral information in generated images, providing a low-energy dataset emphasizing photoelectric absorption and a high energy data set with dominant influence of the Compton effect. Energy-specific mass attenuation coefficients derived from these VMIs (E50 and E200) are the foundation of BMD calculation using DLCT, which was performed via calibration with an established BMD phantom (European Spine Phantom, serial no. 040, QRM GmbH, Möhrendorf, Germany), which contains HA of different specified concentrations and is used for quality control and standardization in DXA and QCT

measurements (Pearson et al., 1995). Spectral absorption characteristics of HA were assessed with a high-dose calibration scan with 1000 mAs. Afterwards, the accuracy of measurements was again determined in a phantom model for different scan parameters as well as patient-sided factors such as varying patient positioning and simulated patient size, as these are also likely to occur in clinical CT examinations. Dual-energy data was then presented in a E50/E200-plot, integrating beforementioned possible confounders in an experimentally derived projection angle of 32° towards the HA calibration line, which in turn features a simple linear relation to BMD. For the first *in-vivo* application in J-I, QCT-based BMD was measured with a clinical in-scan calibration phantom and dedicated software (QCT Pro, Mindways Software, Inc.) for comparative purposes. Analogous to ISCD recommendations regarding asynchronous calibration for BMD measurements at the hip or spine, the in-scan calibration phantom was then waived for subsequent patient examinations in J-II (Engelke et al., 2015).

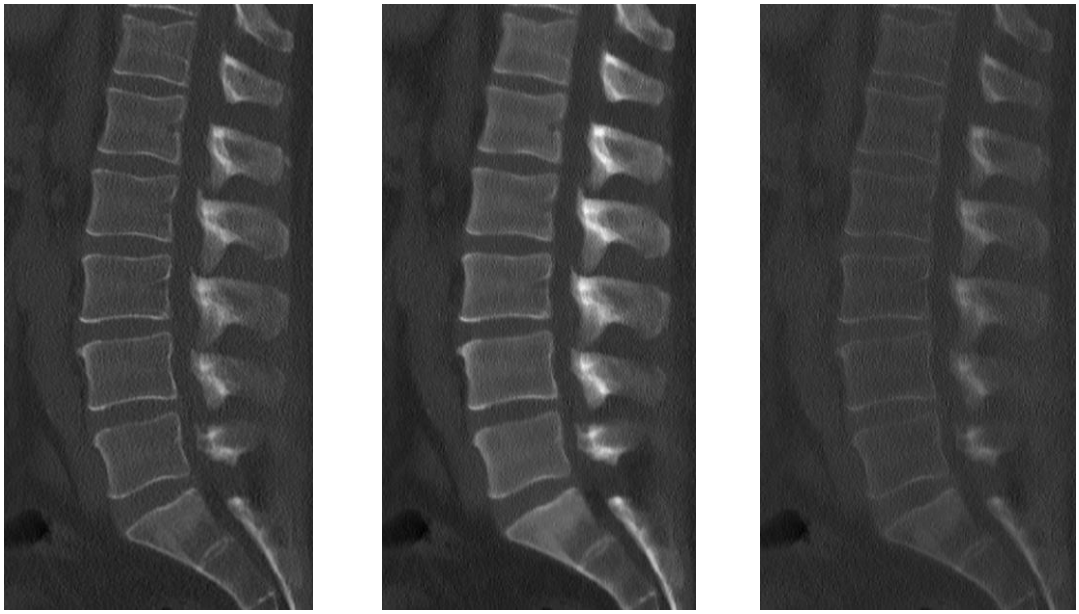

Figure 6: Sagittal reformation of dual-layer spectral CT imaging of the spine. Conventional (left) and virtual monoenergetic images at 50 (middle) and 200 keV (right).

As for the iodine quantification J-II, a commercially available software tool for the two-material decomposition of the basis pair water and iodine was applied, that is embedded in the software package also previously used for the spectral analyses of vertebral bone (IntelliSpace Portal 10.1.0, Philips Healthcare, Best, The Netherlands). Thus, material-specific density maps can be reconstructed which visualize iodine distribution by virtual subtraction of non-iodine-containing voxels in a greyscale matrix and enable iodine quantification based on derived values for iodine concentration [mg/ml] (Rassouli et al., 2017).

2.3 Study designs

Both research projects, J-I and J-II, represent prospective, cross-sectional, mono-center studies of previously acquired imaging data that aim for the optimization and application of opportunistic DLCT imaging in the context of bone loss diagnostics, as well as its evaluation regarding diagnostic accuracy. The study protocol of J-I included CT examinations with acquisition of native clinical DLCT imaging data of the thoracolumbar spinal region, a complete SBI dataset as well as a synchronously scanned QCT phantom (Mindways QCT Pro, Mindways Software, Inc., Austin, Texas, U.S.A.). The study protocol of J-II requires the inclusion of CT examinations with acquisition of triphasic contrast-enhanced DLCT imaging data including the thoracolumbar spine on condition that the SBI dataset is complete. This particularly involves abdominal CT-A scans and cardiovascular studies with a native, arterially triggered contrast phase and a portal-venous phase with 70-sec delay.

Relevant CT data was retrieved employing data search in the institute´s picture archiving and communication system (PACS). All included examinations originated from day-to-day clinical care and were exclusively performed on one DLCT scanner (Philips IQon Spectral CT, Philips Healthcare, Best, Netherlands) at the Department of Diagnostic and Interventional Radiology (Klinikum rechts der Isar, Munich, Germany).

The Institutional Review Board (The Ethics Commission of the Medical Faculty, Technical University of Munich, Germany) approved both study protocols, J-I and J-II, in advance and waived written informed consent on account of the opportunistic approach with post-hoc utilization of already acquired clinical data (project-numbers 5278/12 and 27/19 S-SR, respectively).

2.4 Patient collectives and DLCT imaging protocols

Within the scope of J-I, appropriate DLCT scans meeting the requirements of the study-design were available for 33 patients examined between November 2016 and February 2018, including a total of 174 scanned vertebrae. As for J-II, relevant DLCT scans in accordance with the predefined selection criteria were available for 132 patients scanned between September 2016 and October 2018.

All patient scans were performed using routine clinical CT protocols with a fixed tube-potential of 120 kVp and tube current modulation. For J-I, mean exposure averaged over all examinations was 84 ± 61 mAs (mean ± SD) and mean CT dose indices ($CTDI_{vol}$) were 7.7 ± 5.5 mGy. Here, SBI datasets were reconstructed using standard and bone filter kernels (B, YB, YC), with a slice thickness of 0.9 mm. For J-II, native scans had a mean exposure of 107 ± 49 mAs (mean ± SD) and a mean CT dose index ($CTDI_{vol}$) of 9.7 ± 4.5 mGy. Contrast-

enhanced scans had a similar exposure of 110 ± 43 mAs (mean $CTDI_{vol}$: 10.0 ± 3.9 mGy). SBI datasets were reconstructed using only the standard kernel (B), as well selecting a slice thickness of 0.9 mm.

2.5 Image analyses for in-vivo BMD measurements and iodine quantification

For all spinal BMD measurements, circular ROIs with a diameter of one third of the respective vertebral body´s height were manually placed in sagittal reformations of the thoracolumbar spine. The reconstructed slice thickness was 10 mm for all patient scans. Spinal ROIs were positioned in the ventral halves of the vertebral body to avoid possible measurement errors introduced by including basivertebral veins. Furthermore, the effect of other potential confounding factors was minimized by excluding vertebral bodies with severe degenerative alterations, fractures, or other significant pathologies. For calculating DLCT-based BMD, mean attenuation values from virtual monoenergetic images at different energy levels (50 and 200 keV) were extracted and respective BMD quantification was carried out with the conversion formula derived from preclinical phantom measurements outlined above. Patient-based BMD was subsequently determined by averaging single BMD values across multiple vertebral bodies. For determination of vascular iodine contrast in different contrast phases, circular ROIs were centrally positioned in the vascular lumen of the investigated large vessels (abdominal aorta, inferior vena cava, portal vein) with the aid of either axial or multiplanar reformations and measured iodine concentrations were subsequently used for adjusting respective BMD values derived from contrast-enhanced examinations.

2.6 Statistical analyses

For approaching the selected patient collectives, first off, epidemiologic data was summarized expressing relevant descriptive baseline characteristics like age distribution (mean age ± SD), absolute or relative frequencies for sex ratio as well as absolute frequency of excluded patients, categorized by the respective exclusion criterion. For a simple quantitative comparison of two measurements, means of differences were used to compare BMD data obtained from DLCT or QCT (J-I) and means of absolute errors (MAE) were calculated to check BMD derived from contrast-enhanced scans against their native references (J-II). The statistical evaluation of BMD agreement was further realized with a graphical presentation using the Bland–Altman method (Bland & Altman, 1999). The association of selected quantitative parameters was illustrated in scatter plots (e.g., DLCT- vs. QCT-based BMD in J-II, arterial and portal-venous vs. native DLCT-BMD in J-II) and bivariate correlation of eligible parameters was quantified by using Pearson´s *r*. For J-II, the patient collective was split up in

two datasets (training and test cohort) and functional relations were phase-specifically analyzed using multivariable linear regressions with forward selection of independent variables and – for an analysis independent of retrieved contrast-phase – generalized estimated equations (GEE). Aiming for a reasonable tradeoff between comprehensiveness and complexity, the latter was chosen instead of linear regressions to set up a lean but robust statistical model for analyzing correlated data. Based on data of the training cohort, statistic modeling with linear regressions and GEE was carried out for DLCT-based and conventional BMD data in two separate computational pipelines. Eventually, the statistical models were validated with data of the test cohort. A two-sided P value of less than 0.05 was considered to indicate a statistically significant difference. All statistical calculations and analyses were performed using the software program SPSS version 23 or 25 (IBM Corp., Armonk, N.Y., U.S.A.).

3 Discussion

The two presented journal publications assessed the clinical potential of non-dedicated BMD measurements based on DLCT. The key finding of J-I is that using spectral information in non-contrast-enhanced clinical DLCT examinations provides incremental benefits for BMD testing as measurements showed a high consistency with QCT-derived BMD quantification in the clinically relevant range of BMD while prospective selection of patients eligible for bone densitometry is no longer required. Beforehand, phantom measurements analogously showed comparable results in comparative studies on measurement precision using a spine phantom. As for J-II, we found sufficient evidence that BMD can also be accurately determined in contrast-enhanced DLCT scans, irrespective of the underlying contrast phase, when adequate adjustments for vascular iodine contrast are made.

Early phantom studies with DLCT have investigated the accuracy of phantomless HA quantification and suggested its consideration for further evaluation in clinical contexts. Using a variety of acquisitive and reconstructive parameters as well as two different tube voltages, van Hamersvelt et al. found average measurement errors of -5.6 ± 5.7 mg/cm^3 (-3.6 ± 3.2%) at 120 kVp as well as a high linear correlation with DXA (van Hamersvelt et al., 2017). A different methodical approach for quantifying HA pixel-by-pixel reported high precision for phantom measurements (-1.3 to 4.8% for exposures of 125 mAs and above) and showed substantial correlations and agreement with QCT for vertebral *ex vivo* specimen, that were cleared of soft tissue (Pearson`s r: 0.96 – 0.99), while simulating different grades of obesity (Mei et al., 2017). To date, only few other studies have evaluated the role of DLCT for measuring BMD in patients. Van Hedent et al. examined the measuring precision of DCLT using a K_2PO_4 phantom (-12.3 ± 4.3 mg/cm^3 or -2.2 ± 6.6% for standard protocol) and showed an excellent sensitivity of 100% and a moderate specificity of 73% compared with ap-DXA as a gold standard *in vivo* (Van Hedent et al., 2019). A major drawback of this study, however, is a substantial part of included DLCT scans with contrast-enhancement, which were converted according to a formula based on phantomless BMD measurements with internal calibration derived from several different non-DLCT systems. A further approach to opportunistic screening with DLCT is the use of routine DLCT scout scans, that enable semi-automatic aBMD measurements highly correlating with DXA (Laugerette et al., 2019).

The continuation in evaluating this BMD measurement technique for clinical application encompassed a potential use of contrast-enhanced DLCT examinations for opportunistic BMD screening. The administration of intravenous contrast agent generally limits the applicability of CT scans for non-dedicated BMD screening through an elevation of attenuation values and consequently incorrect measurements (Pompe et al., 2015; Toelly et al., 2017). Thus, the effects of intravascular iodine contrast agent on the precision of measurements were assessed

and consequently adjusted for by integrating a correction based on spectral iodine quantification. The potential extension in retrievable CT examinations in view of contrast-enhanced scans distinctly enhances the applicability of this method and may therefore provide an adjunctive diagnostic value as well as help optimizing the management of osteoporosis. A considerable body of literature exists suggesting a high accuracy of iodine quantification with DLCT in phantom studies with average relative measurement errors in the range of about 3.4 (Ehn et al., 2018; Sauter et al., 2018) to 6% (Ozguner et al., 2018) and, if any, minimal effects of tube voltage, exposure level within the diagnostic range or different spectral iterative reconstruction levels (Kim et al., 2018; Lu et al., 2019). For two-material decompositions, elements with in-between atomic number are partially attributed to each of the basis pair materials (Patino et al., 2016). The material separation of HA and iodine *in vivo*, however, is challenging and may be associated with the immediate physical proximity of intravascular iodine and trabecular bone. Difficulties in reliable identification of HA were also encountered in a study by Ding et al. showing that L1 HU values measured in VNC images derived from DLCT underestimate HU in true non-contrast images (Ding, Richter, Stiller, Kauczor, & Weber, 2019), which might indicate a misidentification of bone minerals for iodine, but anyway likewise reveals the difficulties of adequate separation pertaining iodine quantification within osseous structures. Varying degrees of physical density may contribute to this disparate and limit material separation of bone and iodine despite principal distinguishability pertaining to effective atomic number as well as spectral absorption characteristics. Therefore, a different, non-osseous measurement location was required to better adjust for the influence of systemic iodine contrast agent. In a prospective study, HU measurements in soft tissues such as liver, spleen, kidney, or muscle as well as vascular measurements showed similar CT attenuation values in VNC and TNC image series and over various contrast phases, except for subcutaneous fat (Ananthakrishnan et al., 2017). For iodine adjustment of BMD in contrast-enhanced examinations, the vascular compartment appeared likely to be the most appropriate measuring site. Hence, a dual use of spectral analyses for both BMD and vessel iodine concentrations in major vessels was the methodic approach of J-II and results not only suggest that iodine contrast agents substantially affect measured BMD values, but also that adjusting for vascular iodine quantification derived from iodine density maps – particularly measured within the portal vein – improves BMD accuracy and DLCT-derived BMD values tend to be more robust than conventional ones. In this context, a key base of our considerations was to further build a computation model that is independent of the respective contrast phase as previous studies also shown the influence of scan timing on measured attenuation values in contrast-enhanced phases (Acu, Scheel, & Issever, 2014; Pompe et al., 2015). Other approaches like conversion equations to QCT-BMD or T scores previously proved feasibility

for opportunistic screening for low BMD in contrast-enhanced CT scans as well showing their potential for fracture risk stratification (Baum et al., 2012; Gruber et al., 2013).

Opportunistic imaging for BMD quantification is clinically relevant. Given the fact that clinical CT sees a steadily increasing utilization, with an approximate increase of 50% in CT examinations within the 10-year-period from 2007 to 2017 in Germany (OECD, 2019), DLCT may substantially enhance the clinical applicability by overcoming the need for in-scan calibration phantoms or prospective choice of specific scan protocols and extending the number of CT examinations potentially retrievable for BMD assessment by accessing contrast-enhanced examinations. Several studies have suggested the clinical value of opportunistic BMD screening, particularly in high-risk collectives like cancer patients, who are at increased risk for fracture related to both malignancy and oncological therapy (Wild, Dankerl, Hammon, Uder, & Janka, 2016): In a uro-oncological cohort, for instance, quantitative vertebral bone assessment with positron emission tomography – computed tomography (PET-CT) was on a par with BMD derived from routine clinical CT (Schwaiger et al., 2017), which may be beneficial for monitoring therapy or guiding fracture prevention (e.g., for lack of therapy response, further BMD loss or fragility fractures despite therapy). Assessing the use of opportunistic vertebral BMD converted by scanner-specific equations, a prospective clinical trial indicated superiority over DXA for predicting the risk for incident fractures in a three-year follow up of a gynecological cohort (Leonhardt et al., 2020).

Several limitations were encountered in the presented studies. First off, the WHO definition as well as related diagnostic classifications of osteoporosis are based on DXA and formally apply only to respective measurements at the femoral neck, total femur, lumbar spine, or one-third radius. Thus, broad clinical application of opportunistic BMD screening would require a re-definition of osteoporosis, to enable direct diagnosis with other, non-dedicated imaging modalities in accordance with WHO positions. Moreover, the proposed method for BMD assessment is based on scanner specific calibration, that may account for unknown system-inherent factors. In the context of opportunistic CT imaging, however, international guidelines call for “validated machine-specific cutoff values and scanner stability” (ISCD 2019) to opportunistically screen for patients with low BMD or compromised bone strength. Consequently, asynchronous calibration presumes CT scanner stability or quality control measures to assess a potential need for intermittent re-calibration. Yet, this was not yet specifically addressed in our studies, and it remains to be investigated, if results are directly transferable to other DLCT scanners. Being the standard tube potential in most clinical scans, all CT examinations were performed with 120 kVp and a closer examination of the influence of tube potential *in vivo*, was not within the scope of this thesis. The same applies for a thorough analysis of intravenous contrast protocols or circulatory parameters that may affect contrast distribution (e.g., no systemic variation in volume of contrast load (Habashy, Yan,

Brown, Xiong, & Kaste, 2011), scan timing (Acu et al., 2014) or assessment of circulatory parameters). The possible influence of these parameters was not specifically addressed in this work due to the post-hoc analysis of routine clinical imaging data.

The present research work can be considered to establish a baseline for the clinical use of spectral information regarding the detection of conditions with low BMD in DLCT. However, further research is needed to bridge gaps in evidence: First, well-designed prospective trials with sufficiently large patient populations are essential to generate data for the validation of DLCT´s potential for fracture-risk prediction and could also shed light on medium-term re-test reliability through longitudinal data. Then, additional applications pertaining to the assessment of trabecular microstructure such as morphometry or finite-element analysis should be specifically evaluated for possible additional benefits regarding a comprehensive assessment of bone integrity with DLCT. In addition, spectral overlap is an issue inherent in all dual-energy CT set-ups. Multi-energy CT imaging with energy-resolving photon-counting detectors may improve spectral resolution by using several predefined energy-bins (Willemink, Persson, Pourmorteza, Pelc, & Fleischmann, 2018) and should be investigated for their clinical potential regarding the accuracy of bone densitometry.

To conclude, the results of the present research work demonstrate that dual-layer spectral CT allows for BMD assessment in routine clinical examinations without the need for an in-scan calibration phantom, thus enabling a truly opportunistic post-hoc analysis of previously acquired imaging data. Essentially, contrast enhanced DLCT examinations can be used for this as well, but acquired measurements must undergo subsequent conversion with adjustments for vascular iodine contrast, which however can be conducted independent of contrast phase. It seems reasonable to preferably use non-enhanced DLCT data, when available. Providing more in-depth clinical insight by using dual-energy information, opportunistic use of DLCT for BMD measurements may enhance applicability and support radiologists in reaching an accurate diagnosis of conditions with low BMD and eventually may spare patients additional dedicated BMD assessment. Thus, it may help optimizing patient care, particularly for patients with secondary or therapy-associated causes for osteoporosis.

4 Summary of Journal Publications

4.1 J-I: Bone mineral density measurements derived from dual-layer spectral CT enable opportunistic screening for osteoporosis

This original research article was published in European Radiology on 2 May 2019. The first authorship is shared with Johannes Hammel. The co-authors are Kai Mei, Thomas Baum, Jan S. Kirschke, Alexis Laugerette, Felix K. Kopp, Jannis Bodden, Daniela Pfeiffer, Franz Pfeiffer, Ernst J. Rummeny, Peter B. Noël, Alexandra S. Gersing and Benedikt J. Schwaiger.

4.1.1 Summary of J-I

The aim of this study was to evaluate the clinical applicability of hydroxyapatite-calibrated bone mineral density measurements derived from native dual-layer spectral CT examinations. In the first place, spectral data from three artificial vertebral bodies of different HA densities was used for BMD calibration with DLCT, simulating several different grades of obesity and varying patient positioning. Quantitative CT (QCT) was used as standard of reference. BMD was calculated from virtual monoenergetic images at energy levels of 50 and 200 keV. In total, 33 patients (66 ± 18 years; 33% women) were enrolled and 174 individual vertebral bodies were measured for HA-calibrated BMD in non-contrast routine DLCT as well as QCT. The main finding of this study is that *in-vivo* measurements showed marked correlations between DLCT and QCT ($r = 0.987$ [95% confidence interval, 0.963–1.000]; $p < 0.001$) as well as notable agreement of BMD measurements. In conclusion, HA-calibrated BMD measurements derived from DLCT were similar to QCT in *in-vivo* analyses. This finding suggests that opportunistic DLCT-based BMD measurements are an alternative to QCT, without the need for in-scan phantoms or dedicated protocols.

4.1.2 Author's individual contribution to J-I

The doctoral candidate contributed substantially and independently to originality, innovativeness, scientific and clinical relevance of the research project this publication was based on. In particular, he set up the experimental study protocol including phantom measurements as well as definition of inclusion criteria for in-vivo examinations. Moreover, Mr. Roski independently performed phantom examinations and measurements in clinical imaging data, conducted quality assurance and reproducibility tests and applied and validated post-processing steps, the latter together in close interprofessional cooperation with Mr. Hammel

and Mr. Laugerette of the TUM Chair of Biomedical Physics. The candidate independently carried out formal analyses, selected and applied all mentioned statistical techniques for both phantom and patient data, and assumed a leading role in the ensuing interpretation of the results and their evaluation in the scientific context. Mr. Roski was also in the lead regarding the drafting, editing, and revising of the manuscript. Supervision and guidance were provided by senior members of our workgroup, as is good clinical and scientific practice.

Rationale of shared first authorship

Being situated at the transition from preclinical phantom studies to actual in-vivo BMD measurements, the development and realization of research project J-I required in-depth expertise both in the fields of CT physics and clinical musculoskeletal radiology. The present publication is a result of this successful cooperation of biomedical physicists and clinical scientists. Consequently, the shared first authorship of Ferdinand Roski and Johannes Hammel reflects this duality inherent in this research topic as both authors made substantial contributions to the resulting publication.

4.2 J-II: Opportunistic osteoporosis screening: contrast-enhanced dual-layer spectral CT provides accurate measurements of vertebral volumetric bone mineral density

This original research article was published in European Radiology on 14 October 2020. The co-authors are Johannes Hammel, Kai Mei, Bernhard Haller, Thomas Baum, Jan S. Kirschke, Daniela Pfeiffer, Klaus Woertler, Franz Pfeiffer, Peter B. Noël, Alexandra S. Gersing and Benedikt J. Schwaiger.

4.2.1 Summary of J-II

The main objective of this study was to evaluate whether opportunistic BMD measurements with dual-layer spectral CT (DLCT) can be accurately derived from non-dedicated examinations enhanced with iodine-based intravenous contrast agent. Vertebral BMD was determined in triphasic (native, arterial, and portal-venous scan phase) DLCT examinations for 132 patients (63 ± 16 years; 32% women) based on virtual monoenergetic images (50 and 200 keV). An asynchronous QCT phantom calibration served as standard of reference. Further, vascular iodine densities of three major vessels (aorta, inferior vena cava, portal vein) were determined using a commercially available iodine quantification tool and measurements were used to evaluate precision of DLCT-BMD as well as for iodine-adjustment purposes in multivariable linear regressions. BMD measurements from contrast enhanced DLCT scan phases featured substantial agreement with non-enhanced measurements, when adjusted with vascular iodine concentrations of the portal vein and/or the abdominal aorta, and mean absolute errors tended to be lower compared with BMD derived from conventional QCT phantom calibration. Overall, this investigation showed that converted BMD from contrast enhanced DLCT showed high agreement with non-enhanced DLCT-BMD, when adjusted for vascular iodine concentrations. The results suggest feasibility of opportunistic BMD measurements in routine contrast enhanced DLCT scans and therefore constitute a huge potential for expansion of clinical applicability.

4.2.2 Author's individual contribution to J-II

The doctoral candidate contributed substantially and independently to originality, innovativeness, scientific and clinical relevance of the research project this publication was based on. In particular, after thorough literature research and discussion in our interdisciplinary workgroup, he set up a feasible and targeted study protocol comprising inclusion and exclusion criteria as well as an experimental work program to select appropriate imaging data and to perform tissue measurements. Mr. Roski then independently implemented patient selection

and performed experimental work as described above. Again, he selected and applied all described statistical techniques – for more advanced statistical applications, particularly generalized estimated equations, guidance was provided by an experienced statistician (Bernhard Haller from TUM Institute of Medical Informatics, Statistics and Epidemiology). The doctoral candidate assumed a leading role in the ensuing interpretation of the results and their evaluation in the scientific context. Mr. Roski was also in the lead regarding the drafting, editing, and revising of the manuscript, and created all tables and figures. Supervision and guidance were provided by senior members of our workgroup, as is good clinical and scientific practice.

Approval for inclusion of journal publications and secondary publication in doctoral dissertation

Both included journal publications were published according to European Radiology`s open-access policy under the Creative Commons Attribution 4.0 International License (CC BY). The publishers copyright conditions explicitly specify that the copyright remains with the group of authors. Consequently, a distinct written reprint permission cannot be issued by the publisher house. Still, the fact that explicit written permission from the publisher is not required for reproduction was recorded in personal correspondence with the Editorial Board of European Radiology. Any and all co-authors who contributed to either of the two included journal publications explicitly approved the inclusion of the respective journal publication in Mr. Roski´s cumulative doctoral dissertation, confirmed that the respective journal publication was primarily drafted under the leadership of the doctoral candidate and furthermore explicitly consented to the publication of his doctoral thesis in written form.

List of Figures

Acknowledgements

In developing this work, I received a lot of assistance and support from various people, starting from the conception to the final proofreading.

First and foremost, I would like to express my sincere gratitude to my academic supervisor PD Dr. med. Benedikt J. Schwaiger, who introduced me in the field of clinical radiology and its scientific environment with great dedication and personal effort. Thank you for your committed guidance, thorough advice, and insightful feedback throughout the last four years and all the enriching ideas you shared with me both personally and professionally.

Hereafter, I would also like to thank PD Dr. med. Thomas Baum for his appreciated work as my mentor, sharing his rich experience as well as his continuous support through all our common research projects.

I would also like to thank Johannes Hammel from the department of biomedical physics for the fruitful and enjoyable cooperation regarding our joint scientific work.

Besides, I would like to acknowledge PD Dr. med. Alexandra S. Gersing, Prof. Dr. med. Jan S. Kirschke, Prof. Dr. rer. nat. Peter B. Noël and Prof. Dr. med. Klaus Wörtler for their constructive input and their valuable contributions to our scientific projects.

In addition, special thanks are due to David Jany and Felix Gebser for their excellent and steady technical support, whenever any kind of technology was temporarily underperforming.

I am also grateful to Prof. Dr. med. Ernst J. Rummeny and Prof. Dr. med. Claus Zimmer for giving me the opportunity to work in such an enriching environment at the Departments of Radiology and Neuroradiology, facilitating these exciting scientific efforts.

Finally, I want to thank my family and friends for their patience and encouragement. I really am appreciative to have such supportive and reliable people around me with whom to share so many enjoyable moments.

References

ACR. (2018). *ACR–SPR–SSR practice parameter for the performance of muskuloskeletal quantitative computed tomography (QCT)*. Retrieved from

Acu, K., Scheel, M., & Issever, A. S. (2014). Time dependency of bone density estimation from computed tomography with intravenous contrast agent administration. *Osteoporos Int, 25*(2), 535-542. doi:10.1007/s00198-013-2440-4

Adams, J. E. (2009). Quantitative computed tomography. *Eur J Radiol, 71*(3), 415-424. doi:10.1016/j.ejrad.2009.04.074

Adams, M. A., Pollintine, P., Tobias, J. H., Wakley, G. K., & Dolan, P. (2006). Intervertebral disc degeneration can predispose to anterior vertebral fractures in the thoracolumbar spine. *J Bone Miner Res, 21*(9), 1409-1416. doi:10.1359/jbmr.060609

Almeida, M., Laurent, M. R., Dubois, V., Claessens, F., O'Brien, C. A., Bouillon, R., . . . Manolagas, S. C. (2017). Estrogens and Androgens in Skeletal Physiology and Pathophysiology. *Physiol Rev, 97*(1), 135-187. doi:10.1152/physrev.00033.2015

Alvarez, R. E., & Macovski, A. (1976). Energy-selective reconstructions in X-ray computerized tomography. *Phys Med Biol, 21*(5), 733-744. doi:10.1088/0031-9155/21/5/002

Ananthakrishnan, L., Rajiah, P., Ahn, R., Rassouli, N., Xi, Y., Soesbe, T. C., . . . Abbara, S. (2017). Spectral detector CT-derived virtual non-contrast images: comparison of attenuation values with unenhanced CT. *Abdom Radiol (NY), 42*(3), 702-709. doi:10.1007/s00261-016-1036-9

Anderson, G. L., Limacher, M., Assaf, A. R., Bassford, T., Beresford, S. A., Black, H., . . . Women's Health Initiative Steering, C. (2004). Effects of conjugated equine estrogen in postmenopausal women with hysterectomy: the Women's Health Initiative randomized controlled trial. *JAMA, 291*(14), 1701-1712. doi:10.1001/jama.291.14.1701

Antonacci, M. D., Hanson, D. S., Leblanc, A., & Heggeness, M. H. (1997). Regional variation in vertebral bone density and trabecular architecture are influenced by osteoarthritic change and osteoporosis. *Spine (Phila Pa 1976), 22*(20), 2393-2401; discussion 2401-2392. doi:10.1097/00007632-199710150-00014

Aran, S., Daftari Besheli, L., Karcaaltincaba, M., Gupta, R., Flores, E. J., & Abujudeh, H. H. (2014). Applications of dual-energy CT in emergency radiology. *AJR Am J Roentgenol, 202*(4), W314-324. doi:10.2214/AJR.13.11682

Avenell, A., Mak, J. C., & O'Connell, D. (2014). Vitamin D and vitamin D analogues for preventing fractures in post-menopausal women and older men. *Cochrane Database Syst Rev*(4), CD000227. doi:10.1002/14651858.CD000227.pub4

Banse, X., Devogelaer, J. P., Munting, E., Delloye, C., Cornu, O., & Grynpas, M. (2001). Inhomogeneity of human vertebral cancellous bone: systematic density and structure patterns inside the vertebral body. *Bone, 28*(5), 563-571. doi:10.1016/s8756-3282(01)00425-2

Barrett, J. F., & Keat, N. (2004). Artifacts in CT: recognition and avoidance. *Radiographics, 24*(6), 1679-1691. doi:10.1148/rg.246045065

Barrett-Connor, E., Mosca, L., Collins, P., Geiger, M. J., Grady, D., Kornitzer, M., . . . Raloxifene Use for The Heart Trial, I. (2006). Effects of raloxifene on cardiovascular events and breast cancer in postmenopausal women. *N Engl J Med, 355*(2), 125-137. doi:10.1056/NEJMoa062462

Basaria, S., Lieb, J., 2nd, Tang, A. M., DeWeese, T., Carducci, M., Eisenberger, M., & Dobs, A. S. (2002). Long-term effects of androgen deprivation therapy in prostate cancer patients. *Clin Endocrinol (Oxf), 56*(6), 779-786. doi:10.1046/j.1365-2265.2002.01551.x

Baum, T., Muller, D., Dobritz, M., Wolf, P., Rummeny, E. J., Link, T. M., & Bauer, J. S. (2012). Converted lumbar BMD values derived from sagittal reformations of contrast-enhanced MDCT predict incidental osteoporotic vertebral fractures. *Calcif Tissue Int, 90*(6), 481-487. doi:10.1007/s00223-012-9596-3

Baylink, D. J. (1983). Glucocorticoid-induced osteoporosis. *N Engl J Med, 309*(5), 306-308. doi:10.1056/NEJM198308043090509

Beckett, K. R., Moriarity, A. K., & Langer, J. M. (2015). Safe Use of Contrast Media: What the Radiologist Needs to Know. *Radiographics, 35*(6), 1738-1750. doi:10.1148/rg.2015150033

Bernsen, M. L. E., Veendrick, P. B., Martens, J. M., Pijl, M. E. J., Hofmeijer, J., & van Gorp, M. J. (2021). Initial experience with dual-layer detector spectral CT for diagnosis of blood or contrast after endovascular treatment for ischemic stroke. *Neuroradiology*. doi:10.1007/s00234-021-02736-5

Black, D. M., Bauer, D. C., Vittinghoff, E., Lui, L. Y., Grauer, A., Marin, F., . . . Foundation for the National Institutes of Health Bone Quality, P. (2020). Treatment-related changes in bone mineral density as a surrogate biomarker for fracture risk reduction: meta-regression analyses of individual patient data from multiple randomised controlled trials. *Lancet Diabetes Endocrinol, 8*(8), 672-682. doi:10.1016/S2213-8587(20)30159-5

Black, D. M., Cummings, S. R., Karpf, D. B., Cauley, J. A., Thompson, D. E., Nevitt, M. C., . . . Ensrud, K. E. (1996). Randomised trial of effect of alendronate on risk of fracture in women with existing vertebral fractures. Fracture Intervention Trial Research Group. *Lancet, 348*(9041), 1535-1541. doi:10.1016/s0140-6736(96)07088-2

Black, D. M., Delmas, P. D., Eastell, R., Reid, I. R., Boonen, S., Cauley, J. A., . . . Trial, H. P. F. (2007). Once-yearly zoledronic acid for treatment of postmenopausal osteoporosis. *N Engl J Med, 356*(18), 1809-1822. doi:10.1056/NEJMoa067312

Blake, G. M., Naeem, M., & Boutros, M. (2006). Comparison of effective dose to children and adults from dual X-ray absorptiometry examinations. *Bone, 38*(6), 935-942. doi:10.1016/j.bone.2005.11.007

Bland, J. M., & Altman, D. G. (1999). Measuring agreement in method comparison studies. *Stat Methods Med Res, 8*(2), 135-160. doi:10.1177/096228029900800204

Bliuc, D., Alarkawi, D., Nguyen, T. V., Eisman, J. A., & Center, J. R. (2015). Risk of subsequent fractures and mortality in elderly women and men with fragility fractures with and without osteoporotic bone density: the Dubbo Osteoporosis Epidemiology Study. *J Bone Miner Res, 30*(4), 637-646. doi:10.1002/jbmr.2393

Boden, S. D., Goodenough, D. J., Stockham, C. D., Jacobs, E., Dina, T., & Allman, R. M. (1989). Precise measurement of vertebral bone density using computed tomography without the use of an external reference phantom. *J Digit Imaging, 2*(1), 31-38. doi:10.1007/BF03168013

Boehm, H. F., Raeth, C., Monetti, R. A., Mueller, D., Newitt, D., Majumdar, S., . . . Link, T. M. (2003). Local 3D scaling properties for the analysis of trabecular bone extracted from high-resolution magnetic resonance imaging of human trabecular bone: comparison with bone mineral density in the prediction of biomechanical strength in vitro. *Invest Radiol, 38*(5), 269-280. doi:10.1097/01.RLI.0000064782.94757.0f

Bone, H. G., Bolognese, M. A., Yuen, C. K., Kendler, D. L., Wang, H., Liu, Y., & San Martin, J. (2008). Effects of denosumab on bone mineral density and bone turnover in postmenopausal women. *J Clin Endocrinol Metab, 93*(6), 2149-2157. doi:10.1210/jc.2007-2814

Boyle, W. J., Simonet, W. S., & Lacey, D. L. (2003). Osteoclast differentiation and activation. *Nature, 423*(6937), 337-342. doi:10.1038/nature01658

Brett, A. D., & Brown, J. K. (2015). Quantitative computed tomography and opportunistic bone density screening by dual use of computed tomography scans. *J Orthop Translat, 3*(4), 178-184. doi:10.1016/j.jot.2015.08.006

Briggs, A. M., Greig, A. M., Wark, J. D., Fazzalari, N. L., & Bennell, K. L. (2004). A review of anatomical and mechanical factors affecting vertebral body integrity. *Int J Med Sci, 1*(3), 170-180. doi:10.7150/ijms.1.170

Brooks, R. A., & Di Chiro, G. (1976). Principles of computer assisted tomography (CAT) in radiographic and radioisotopic imaging. *Phys Med Biol, 21*(5), 689-732. doi:10.1088/0031-9155/21/5/001

Brown, J. K., Timm, W., Bodeen, G., Chason, A., Perry, M., Vernacchia, F., & DeJournett, R. (2017). Asynchronously Calibrated Quantitative Bone Densitometry. *J Clin Densitom, 20*(2), 216-225. doi:10.1016/j.jocd.2015.11.001

Burghardt, A. J., Pialat, J. B., Kazakia, G. J., Boutroy, S., Engelke, K., Patsch, J. M., . . . Majumdar, S. (2013). Multicenter precision of cortical and trabecular bone quality measures assessed by high-resolution peripheral quantitative computed tomography. *J Bone Miner Res, 28*(3), 524-536. doi:10.1002/jbmr.1795

Cauley, J. A., Thompson, D. E., Ensrud, K. C., Scott, J. C., & Black, D. (2000). Risk of mortality following clinical fractures. *Osteoporos Int, 11*(7), 556-561. doi:10.1007/s001980070075

Chen, H., Shoumura, S., Emura, S., & Bunai, Y. (2008). Regional variations of vertebral trabecular bone microstructure with age and gender. *Osteoporos Int, 19*(10), 1473-1483. doi:10.1007/s00198-008-0593-3

Chesnut, C. H., 3rd, Skag, A., Christiansen, C., Recker, R., Stakkestad, J. A., Hoiseth, A., . . . Europe. (2004). Effects of oral ibandronate administered daily or intermittently on fracture risk in postmenopausal osteoporosis. *J Bone Miner Res, 19*(8), 1241-1249. doi:10.1359/JBMR.040325

Christiansen, B. A., & Bouxsein, M. L. (2010). Biomechanics of vertebral fractures and the vertebral fracture cascade. *Curr Osteoporos Rep, 8*(4), 198-204. doi:10.1007/s11914-010-0031-2

Cosman, F., de Beur, S. J., LeBoff, M. S., Lewiecki, E. M., Tanner, B., Randall, S., . . . National Osteoporosis, F. (2014). Clinician's Guide to Prevention and Treatment of Osteoporosis. *Osteoporos Int, 25*(10), 2359-2381. doi:10.1007/s00198-014-2794-2

Cummings, S. R., San Martin, J., McClung, M. R., Siris, E. S., Eastell, R., Reid, I. R., . . . Trial, F. (2009). Denosumab for prevention of fractures in postmenopausal women with osteoporosis. *N Engl J Med, 361*(8), 756-765. doi:10.1056/NEJMoa0809493

Dachverband der Deutschsprachigen Osteologischen Fachgesellschaften, D. (2017). *Leitlinie: Prophylaxe, Diagnostik und Therapie der Osteoporose bei postmenopausalen Frauen und bei Männern*.

Daci, E., Everts, V., Torrekens, S., Van Herck, E., Tigchelaar-Gutterr, W., Bouillon, R., & Carmeliet, G. (2003). Increased bone formation in mice lacking plasminogen activators. *J Bone Miner Res, 18*(7), 1167-1176. doi:10.1359/jbmr.2003.18.7.1167

Delmas, P. D., Genant, H. K., Crans, G. G., Stock, J. L., Wong, M., Siris, E., & Adachi, J. D. (2003). Severity of prevalent vertebral fractures and the risk of subsequent vertebral and nonvertebral fractures: results from the MORE trial. *Bone, 33*(4), 522-532. doi:10.1016/s8756-3282(03)00241-2

Denis, F. (1983). The three column spine and its significance in the classification of acute thoracolumbar spinal injuries. *Spine (Phila Pa 1976), 8*(8), 817-831. doi:10.1097/00007632-198311000-00003

Ding, Y., Richter, A., Stiller, W., Kauczor, H. U., & Weber, T. F. (2019). Association between true non-contrast and virtual non-contrast vertebral bone CT attenuation values determined using dual-layer spectral detector CT. *Eur J Radiol, 121*, 108740. doi:10.1016/j.ejrad.2019.108740

Eastell, R., Hannon, R. A., Cuzick, J., Dowsett, M., Clack, G., Adams, J. E., & group, A. T. (2006). Effect of an aromatase inhibitor on bmd and bone turnover markers: 2-year results of the Anastrozole, Tamoxifen, Alone or in Combination (ATAC) trial (18233230). *J Bone Miner Res, 21*(8), 1215-1223. doi:10.1359/jbmr.060508

Eghbali-Fatourechi, G., Khosla, S., Sanyal, A., Boyle, W. J., Lacey, D. L., & Riggs, B. L. (2003). Role of RANK ligand in mediating increased bone resorption in early postmenopausal women. *J Clin Invest, 111*(8), 1221-1230. doi:10.1172/JCI17215

Ehn, S., Sellerer, T., Muenzel, D., Fingerle, A. A., Kopp, F., Duda, M., . . . Noel, P. B. (2018). Assessment of quantification accuracy and image quality of a full-body dual-layer spectral CT system. *J Appl Clin Med Phys, 19*(1), 204-217. doi:10.1002/acm2.12243

Ellis, G. K., Bone, H. G., Chlebowski, R., Paul, D., Spadafora, S., Smith, J., . . . Jun, S. (2008). Randomized trial of denosumab in patients receiving adjuvant aromatase inhibitors for

nonmetastatic breast cancer. *J Clin Oncol, 26*(30), 4875-4882. doi:10.1200/JCO.2008.16.3832

Engelke, K. (2017). Quantitative Computed Tomography-Current Status and New Developments. *J Clin Densitom, 20*(3), 309-321. doi:10.1016/j.jocd.2017.06.017

Engelke, K., Adams, J. E., Armbrecht, G., Augat, P., Bogado, C. E., Bouxsein, M. L., . . . Lewiecki, E. M. (2008). Clinical use of quantitative computed tomography and peripheral quantitative computed tomography in the management of osteoporosis in adults: the 2007 ISCD Official Positions. *J Clin Densitom, 11*(1), 123-162. doi:10.1016/j.jocd.2007.12.010

Engelke, K., Lang, T., Khosla, S., Qin, L., Zysset, P., Leslie, W. D., . . . Shousboe, J. T. (2015). Clinical Use of Quantitative Computed Tomography-Based Advanced Techniques in the Management of Osteoporosis in Adults: the 2015 ISCD Official Positions-Part III. *J Clin Densitom, 18*(3), 393-407. doi:10.1016/j.jocd.2015.06.010

Ese, Z. Z., W. (2019). Influence of 12-bit and 16-bit CT values of metals on dose calculation in radiotherapy using PRIMO, a Monte Carlo code for clinical linear accelerators. *Current Directions in Biomedical Engineering, 5*(1), 597-600. doi:10.1515/cdbme-2019-0150

Eswaran, S. K., Gupta, A., Adams, M. F., & Keaveny, T. M. (2006). Cortical and trabecular load sharing in the human vertebral body. *J Bone Miner Res, 21*(2), 307-314. doi:10.1359/jbmr.2006.21.2.307

Ettinger, B., Black, D. M., Mitlak, B. H., Knickerbocker, R. K., Nickelsen, T., Genant, H. K., . . . Cummings, S. R. (1999). Reduction of vertebral fracture risk in postmenopausal women with osteoporosis treated with raloxifene: results from a 3-year randomized clinical trial. Multiple Outcomes of Raloxifene Evaluation (MORE) Investigators. *JAMA, 282*(7), 637-645. doi:10.1001/jama.282.7.637

Feng, X. (2009). Chemical and Biochemical Basis of Cell-Bone Matrix Interaction in Health and Disease. *Curr Chem Biol, 3*(2), 189-196. doi:10.2174/187231309788166398

Flohr, T. G., McCollough, C. H., Bruder, H., Petersilka, M., Gruber, K., Suss, C., . . . Ohnesorge, B. M. (2006). First performance evaluation of a dual-source CT (DSCT) system. *Eur Radiol, 16*(2), 256-268. doi:10.1007/s00330-005-2919-2

Fraser, L. A., Leslie, W. D., Targownik, L. E., Papaioannou, A., Adachi, J. D., & CaMos Research, G. (2013). The effect of proton pump inhibitors on fracture risk: report from the Canadian Multicenter Osteoporosis Study. *Osteoporos Int, 24*(4), 1161-1168. doi:10.1007/s00198-012-2112-9

Frush, D. P. (2004). Review of radiation issues for computed tomography. *Semin Ultrasound CT MR, 25*(1), 17-24. doi:10.1053/j.sult.2003.10.001

Galbusera, F. (2018). The Human Spine. In F. Galbusera (Ed.), *Biomechanics of the Spine : Basic Concepts, Spinal Disorders and Treatments* (pp. 6-7): Elsevier Science & Technology.

Garnett, R. (2020). A comprehensive review of dual-energy and multi-spectral computed tomography. *Clin Imaging, 67*, 160-169. doi:10.1016/j.clinimag.2020.07.030

Gassert, F. T., Kufner, A., Gassert, F. G., Leonhardt, Y., Kronthaler, S., Schwaiger, B. J., . . . Gersing, A. S. (2022). MR-based proton density fat fraction (PDFF) of the vertebral bone marrow differentiates between patients with and without osteoporotic vertebral fractures. *Osteoporos Int, 33*(2), 487-496. doi:10.1007/s00198-021-06147-3

Gausden, E. B., Nwachukwu, B. U., Schreiber, J. J., Lorich, D. G., & Lane, J. M. (2017). Opportunistic Use of CT Imaging for Osteoporosis Screening and Bone Density Assessment: A Qualitative Systematic Review. *J Bone Joint Surg Am, 99*(18), 1580-1590. doi:10.2106/JBJS.16.00749

Genant, H. K., & Boyd, D. (1977). Quantitative bone mineral analysis using dual energy computed tomography. *Invest Radiol, 12*(6), 545-551. doi:10.1097/00004424-197711000-00015

Genant, H. K., Wu, C. Y., van Kuijk, C., & Nevitt, M. C. (1993). Vertebral fracture assessment using a semiquantitative technique. *J Bone Miner Res, 8*(9), 1137-1148. doi:10.1002/jbmr.5650080915

Geyer, L. L., Schoepf, U. J., Meinel, F. G., Nance, J. W., Jr., Bastarrika, G., Leipsic, J. A., . . . De Cecco, C. N. (2015). State of the Art: Iterative CT Reconstruction Techniques. *Radiology, 276*(2), 339-357. doi:10.1148/radiol.2015132766

Ginat, D. T., & Gupta, R. (2014). Advances in computed tomography imaging technology. *Annu Rev Biomed Eng, 16*, 431-453. doi:10.1146/annurev-bioeng-121813-113601

Gluer, C. C. (2008). A new quality of bone ultrasound research. *IEEE Trans Ultrason Ferroelectr Freq Control, 55*(7), 1524-1528. doi:10.1109/TUFFC.2008.828

Goldman, L. W. (2008). Principles of CT: multislice CT. *J Nucl Med Technol, 36*(2), 57-68; quiz 75-56. doi:10.2967/jnmt.107.044826

Graffy, P. M., Lee, S. J., Ziemlewicz, T. J., & Pickhardt, P. J. (2017). Prevalence of Vertebral Compression Fractures on Routine CT Scans According to L1 Trabecular Attenuation: Determining Relevant Thresholds for Opportunistic Osteoporosis Screening. *AJR Am J Roentgenol, 209*(3), 491-496. doi:10.2214/AJR.17.17853

Gruber, M., Bauer, J. S., Dobritz, M., Beer, A. J., Wolf, P., Woertler, K., . . . Baum, T. (2013). Bone mineral density measurements of the proximal femur from routine contrast-enhanced MDCT data sets correlate with dual-energy X-ray absorptiometry. *Eur Radiol, 23*(2), 505-512. doi:10.1007/s00330-012-2629-5

Habashy, A. H., Yan, X., Brown, J. K., Xiong, X., & Kaste, S. C. (2011). Estimation of bone mineral density in children from diagnostic CT images: a comparison of methods with and without an internal calibration standard. *Bone, 48*(5), 1087-1094. doi:10.1016/j.bone.2010.12.012

Hadji, P., Hardtstock, F., Wilke, T., Joeres, L., Toth, E., Mockel, L., & Gille, P. (2020). Estimated epidemiology of osteoporosis diagnoses and osteoporosis-related high fracture risk in Germany: a German claims data analysis. *Arch Osteoporos, 15*(1), 127. doi:10.1007/s11657-020-00800-w

Hansson, T. H., Keller, T. S., & Spengler, D. M. (1987). Mechanical behavior of the human lumbar spine. II. Fatigue strength during dynamic compressive loading. *J Orthop Res, 5*(4), 479-487. doi:10.1002/jor.1100050403

Harris, S. T., Watts, N. B., Genant, H. K., McKeever, C. D., Hangartner, T., Keller, M., . . . Miller, P. D. (1999). Effects of risedronate treatment on vertebral and nonvertebral fractures in women with postmenopausal osteoporosis: a randomized controlled trial. Vertebral Efficacy With Risedronate Therapy (VERT) Study Group. *JAMA, 282*(14), 1344-1352. doi:10.1001/jama.282.14.1344

Heismann, B. J. L., J.; Stierstorfer, K. . (2003). Density and atomic number measurements with spectral x-ray attenuation method. *Journal of Applied Physics, 94*(3), 2073-2079. doi:10.1063/1.1586963

Hendee, W. R., & O'Connor, M. K. (2012). Radiation risks of medical imaging: separating fact from fantasy. *Radiology, 264*(2), 312-321. doi:10.1148/radiol.12112678

Hernlund, E., Svedbom, A., Ivergard, M., Compston, J., Cooper, C., Stenmark, J., . . . Kanis, J. A. (2013). Osteoporosis in the European Union: medical management, epidemiology and economic burden. A report prepared in collaboration with the International Osteoporosis Foundation (IOF) and the European Federation of Pharmaceutical Industry Associations (EFPIA). *Arch Osteoporos, 8*, 136. doi:10.1007/s11657-013-0136-1

Herold, G. (2019). *Innere Medizin 2020*: Gerd Herold.

Hounsfield, G. N. (1973). Computerized transverse axial scanning (tomography). 1. Description of system. *Br J Radiol, 46*(552), 1016-1022. doi:10.1259/0007-1285-46-552-1016

Hubbell, J. H. (1999). Review of photon interaction cross section data in the medical and biological context. *Phys Med Biol, 44*(1), R1-22. doi:10.1088/0031-9155/44/1/001

International Society for Clinial Densitometry, I. O. F. (2010). 2010 Official Positions on FRAX(R).

Iorio, J. A., Jakoi, A. M., & Singla, A. (2016). Biomechanics of Degenerative Spinal Disorders. *Asian Spine J, 10*(2), 377-384. doi:10.4184/asj.2016.10.2.377

ISCD. (2019). *2019 ISCD Official Positions Adult.* Paper presented at the Position Development Conference.

Jackson, R. D., LaCroix, A. Z., Gass, M., Wallace, R. B., Robbins, J., Lewis, C. E., . . . Women's Health Initiative, I. (2006). Calcium plus vitamin D supplementation and the risk of fractures. *N Engl J Med, 354*(7), 669-683. doi:10.1056/NEJMoa055218

Jang, S., Graffy, P. M., Ziemlewicz, T. J., Lee, S. J., Summers, R. M., & Pickhardt, P. J. (2019). Opportunistic Osteoporosis Screening at Routine Abdominal and Thoracic CT: Normative L1 Trabecular Attenuation Values in More than 20 000 Adults. *Radiology, 291*(2), 360-367. doi:10.1148/radiol.2019181648

Jimi, E., Akiyama, S., Tsurukai, T., Okahashi, N., Kobayashi, K., Udagawa, N., . . . Suda, T. (1999). Osteoclast differentiation factor acts as a multifunctional regulator in murine osteoclast differentiation and function. *J Immunol, 163*(1), 434-442.

Johnell, O., & Kanis, J. A. (2006). An estimate of the worldwide prevalence and disability associated with osteoporotic fractures. *Osteoporos Int, 17*(12), 1726-1733. doi:10.1007/s00198-006-0172-4

Kaesmacher, J., Liebl, H., Baum, T., & Kirschke, J. S. (2017). Bone Mineral Density Estimations From Routine Multidetector Computed Tomography: A Comparative Study of Contrast and Calibration Effects. *J Comput Assist Tomogr, 41*(2), 217-223. doi:10.1097/RCT.0000000000000518

Kalender, W. A., Wolf, H., & Suess, C. (1999). Dose reduction in CT by anatomically adapted tube current modulation. II. Phantom measurements. *Med Phys, 26*(11), 2248-2253. doi:10.1118/1.598738

Kanis, J. A. (2007). On behalf of the World Health Organization scientific group: Assessment of Osteoporosis at the Primary Health-Care Level. Technical Report. *Printed by the University of Sheffield, Edited by the World Health Organization Collaborating Centre for Metabolic Bone Diseases.*

Kanis, J. A., Borgstrom, F., De Laet, C., Johansson, H., Johnell, O., Jonsson, B., . . . Khaltaev, N. (2005). Assessment of fracture risk. *Osteoporos Int, 16*(6), 581-589. doi:10.1007/s00198-004-1780-5

Kanis, J. A., Cooper, C., Rizzoli, R., Reginster, J. Y., Scientific Advisory Board of the European Society for, C., Economic Aspects of, O., . . . National Societies of the International Osteoporosis, F. (2019). European guidance for the diagnosis and management of osteoporosis in postmenopausal women. *Osteoporos Int, 30*(1), 3-44. doi:10.1007/s00198-018-4704-5

Kanis, J. A., Johnell, O., Oden, A., Dawson, A., De Laet, C., & Jonsson, B. (2001). Ten year probabilities of osteoporotic fractures according to BMD and diagnostic thresholds. *Osteoporos Int, 12*(12), 989-995. doi:10.1007/s001980170006

Kanis, J. A., Johnell, O., Oden, A., Johansson, H., & McCloskey, E. (2008). FRAX and the assessment of fracture probability in men and women from the UK. *Osteoporos Int, 19*(4), 385-397. doi:10.1007/s00198-007-0543-5

Kanis, J. A., Oden, A., Johnell, O., Johansson, H., De Laet, C., Brown, J., . . . Yoshimura, N. (2007). The use of clinical risk factors enhances the performance of BMD in the prediction of hip and osteoporotic fractures in men and women. *Osteoporos Int, 18*(8), 1033-1046. doi:10.1007/s00198-007-0343-y

Karampinos, D. C., Ruschke, S., Dieckmeyer, M., Diefenbach, M., Franz, D., Gersing, A. S., . . . Baum, T. (2018). Quantitative MRI and spectroscopy of bone marrow. *J Magn Reson Imaging, 47*(2), 332-353. doi:10.1002/jmri.25769

Keaveny, T. M., Morgan, E. F., Niebur, G. L., & Yeh, O. C. (2001). Biomechanics of trabecular bone. *Annu Rev Biomed Eng, 3*, 307-333. doi:10.1146/annurev.bioeng.3.1.307

Khan, A. A., Morrison, A., Hanley, D. A., Felsenberg, D., McCauley, L. K., O'Ryan, F., . . . International Task Force on Osteonecrosis of the, J. (2015). Diagnosis and management of osteonecrosis of the jaw: a systematic review and international consensus. *J Bone Miner Res, 30*(1), 3-23. doi:10.1002/jbmr.2405

Kim, H., Park, C. M., Kang, C. K., Yoon, J., Chae, K. J., & Goo, J. M. (2018). Effect of CT Acquisition Parameters on Iodine Density Measurement at Dual-Layer Spectral CT. *AJR Am J Roentgenol, 211*(4), 748-754. doi:10.2214/AJR.17.19381

Kopperdahl, D. L., Aspelund, T., Hoffmann, P. F., Sigurdsson, S., Siggeirsdottir, K., Harris, T. B., . . . Keaveny, T. M. (2014). Assessment of incident spine and hip fractures in women

and men using finite element analysis of CT scans. *J Bone Miner Res, 29*(3), 570-580. doi:10.1002/jbmr.2069

Laugerette, A., Schwaiger, B. J., Brown, K., Frerking, L. C., Kopp, F. K., Mei, K., . . . Pfeiffer, F. (2019). DXA-equivalent quantification of bone mineral density using dual-layer spectral CT scout scans. *Eur Radiol, 29*(9), 4624-4634. doi:10.1007/s00330-019-6005-6

Lenart, B. A., Lorich, D. G., & Lane, J. M. (2008). Atypical fractures of the femoral diaphysis in postmenopausal women taking alendronate. *N Engl J Med, 358*(12), 1304-1306. doi:10.1056/NEJMc0707493

Leonhardt, Y., Gassert, F. T., Feuerriegel, G., Gassert, F. G., Kronthaler, S., Boehm, C., . . . Gersing, A. S. (2021). Vertebral bone marrow T2* mapping using chemical shift encoding-based water-fat separation in the quantitative analysis of lumbar osteoporosis and osteoporotic fractures. *Quant Imaging Med Surg, 11*(8), 3715-3725. doi:10.21037/qims-20-1373

Leonhardt, Y., May, P., Gordijenko, O., Koeppen-Ursic, V. A., Brandhorst, H., Zimmer, C., . . . Schwaiger, B. J. (2020). Opportunistic QCT Bone Mineral Density Measurements Predicting Osteoporotic Fractures: A Use Case in a Prospective Clinical Cohort. *Front Endocrinol (Lausanne), 11*, 586352. doi:10.3389/fendo.2020.586352

Liberman, U. A., Weiss, S. R., Broll, J., Minne, H. W., Quan, H., Bell, N. H., . . . Favus, M. (1995). Effect of oral alendronate on bone mineral density and the incidence of fractures in postmenopausal osteoporosis. The Alendronate Phase III Osteoporosis Treatment Study Group. *N Engl J Med, 333*(22), 1437-1443. doi:10.1056/NEJM199511303332201

Lin, X., Patil, S., Gao, Y. G., & Qian, A. (2020). The Bone Extracellular Matrix in Bone Formation and Regeneration. *Front Pharmacol, 11*, 757. doi:10.3389/fphar.2020.00757

Link, T. M. (2012). Osteoporosis imaging: state of the art and advanced imaging. *Radiology, 263*(1), 3-17. doi:10.1148/radiol.12110462

Link, T. M. (2016). Radiology of Osteoporosis. *Can Assoc Radiol J, 67*(1), 28-40. doi:10.1016/j.carj.2015.02.002

Lochmuller, E. M., Poschl, K., Wurstlin, L., Matsuura, M., Muller, R., Link, T. M., & Eckstein, F. (2008). Does thoracic or lumbar spine bone architecture predict vertebral failure strength more accurately than density? *Osteoporos Int, 19*(4), 537-545. doi:10.1007/s00198-007-0478-x

Lodder, M. C., Lems, W. F., Ader, H. J., Marthinsen, A. E., van Coeverden, S. C., Lips, P., . . . Roos, J. C. (2004). Reproducibility of bone mineral density measurement in daily practice. *Ann Rheum Dis, 63*(3), 285-289. doi:10.1136/ard.2002.005678

Lohman, M., Tallroth, K., Kettunen, J. A., & Marttinen, M. T. (2009). Reproducibility of dual-energy x-ray absorptiometry total and regional body composition measurements using different scanning positions and definitions of regions. *Metabolism, 58*(11), 1663-1668. doi:10.1016/j.metabol.2009.05.023

Lu, X., Lu, Z., Yin, J., Gao, Y., Chen, X., & Guo, Q. (2019). Effects of radiation dose levels and spectral iterative reconstruction levels on the accuracy of iodine quantification and virtual monochromatic CT numbers in dual-layer spectral detector CT: an iodine phantom study. *Quant Imaging Med Surg, 9*(2), 188-200. doi:10.21037/qims.2018.11.12

Maass, C., Baer, M., & Kachelriess, M. (2009). Image-based dual energy CT using optimized precorrection functions: a practical new approach of material decomposition in image domain. *Med Phys, 36*(8), 3818-3829. doi:10.1118/1.3157235

Mansouri, M., Aran, S., Singh, A., Kambadakone, A. R., Sahani, D. V., Lev, M. H., & Abujudeh, H. H. (2015). Dual-Energy Computed Tomography Characterization of Urinary Calculi: Basic Principles, Applications and Concerns. *Curr Probl Diagn Radiol, 44*(6), 496-500. doi:10.1067/j.cpradiol.2015.04.003

McBroom, R. J., Hayes, W. C., Edwards, W. T., Goldberg, R. P., & White, A. A., 3rd. (1985). Prediction of vertebral body compressive fracture using quantitative computed tomography. *J Bone Joint Surg Am, 67*(8), 1206-1214.

McCollough, C. H., Leng, S., Yu, L., & Fletcher, J. G. (2015). Dual- and Multi-Energy CT: Principles, Technical Approaches, and Clinical Applications. *Radiology, 276*(3), 637-653. doi:10.1148/radiol.2015142631

Mei, K., Schwaiger, B. J., Kopp, F. K., Ehn, S., Gersing, A. S., Kirschke, J. S., . . . Noel, P. B. (2017). Bone mineral density measurements in vertebral specimens and phantoms using dual-layer spectral computed tomography. *Sci Rep, 7*(1), 17519. doi:10.1038/s41598-017-17855-4

Montazeri, A. M., S.J. (2010). Quality of Life and Low Back Pain *Handbook of Disease Burdens and Quality of Life Measures* (pp. 3979-3994). New York, NY: Springer.

Morin, S., Lix, L. M., Azimaee, M., Metge, C., Caetano, P., & Leslie, W. D. (2011). Mortality rates after incident non-traumatic fractures in older men and women. *Osteoporos Int, 22*(9), 2439-2448. doi:10.1007/s00198-010-1480-2

Mosekilde, L., Mosekilde, L., & Danielsen, C. C. (1987). Biomechanical competence of vertebral trabecular bone in relation to ash density and age in normal individuals. *Bone, 8*(2), 79-85. doi:10.1016/8756-3282(87)90074-3

Mueller, D. K., Kutscherenko, A., Bartel, H., Vlassenbroek, A., Ourednicek, P., & Erckenbrecht, J. (2011). Phantom-less QCT BMD system as screening tool for osteoporosis without additional radiation. *Eur J Radiol, 79*(3), 375-381. doi:10.1016/j.ejrad.2010.02.008

Nagayama, Y., Nakaura, T., Oda, S., Utsunomiya, D., Funama, Y., Iyama, Y., . . . Yamashita, Y. (2018). Dual-layer DECT for multiphasic hepatic CT with 50 percent iodine load: a matched-pair comparison with a 120 kVp protocol. *Eur Radiol, 28*(4), 1719-1730. doi:10.1007/s00330-017-5114-3

Nagel, H. D. (2007). CT Parameters that Influence the Radiation Dose. In D. G. Tack, P. A. (Ed.), *Radiation Dose from Adult and Pediatric Multidetector Computed Tomography* (1 ed., pp. 51-78). Berlin, Heidelberg: Springer.

Neer, R. M., Arnaud, C. D., Zanchetta, J. R., Prince, R., Gaich, G. A., Reginster, J. Y., . . . Mitlak, B. H. (2001). Effect of parathyroid hormone (1-34) on fractures and bone mineral density in postmenopausal women with osteoporosis. *N Engl J Med, 344*(19), 1434-1441. doi:10.1056/NEJM200105103441904

NIH Consensus Development Panel on Osteoporosis Prevention, D., & Therapy. (2001, Feb 14). *Osteoporosis prevention, diagnosis, and therapy*.

Odle, T. (2020). Emergency Computed Tomography. *Radiol Technol, 91*(3), 267CT-287CT.

OECD. (2019). *Health at a Glance 2019: OECD Indicators*. Retrieved from

Oei, L., Koromani, F., Rivadeneira, F., Zillikens, M. C., & Oei, E. H. (2016). Quantitative imaging methods in osteoporosis. *Quant Imaging Med Surg, 6*(6), 680-698. doi:10.21037/qims.2016.12.13

Oxland, T. R. (2016). Fundamental biomechanics of the spine--What we have learned in the past 25 years and future directions. *J Biomech, 49*(6), 817-832. doi:10.1016/j.jbiomech.2015.10.035

Ozguner, O., Dhanantwari, A., Halliburton, S., Wen, G., Utrup, S., & Jordan, D. (2018). Objective image characterization of a spectral CT scanner with dual-layer detector. *Phys Med Biol, 63*(2), 025027. doi:10.1088/1361-6560/aa9e1b

Patino, M., Prochowski, A., Agrawal, M. D., Simeone, F. J., Gupta, R., Hahn, P. F., & Sahani, D. V. (2016). Material Separation Using Dual-Energy CT: Current and Emerging Applications. *Radiographics, 36*(4), 1087-1105. doi:10.1148/rg.2016150220

Pearson, J., Dequeker, J., Henley, M., Bright, J., Reeve, J., Kalender, W., . . . et al. (1995). European semi-anthropomorphic spine phantom for the calibration of bone densitometers: assessment of precision, stability and accuracy. The European Quantitation of Osteoporosis Study Group. *Osteoporos Int, 5*(3), 174-184. doi:10.1007/BF02106097

Pelc, N. J. (2014). Recent and future directions in CT imaging. *Ann Biomed Eng, 42*(2), 260-268. doi:10.1007/s10439-014-0974-z

Petersilka, M., Stierstorfer, K., Bruder, H., & Flohr, T. (2010). Strategies for scatter correction in dual source CT. *Med Phys, 37*(11), 5971-5992. doi:10.1118/1.3504606

Pickhardt, P. J., Lauder, T., Pooler, B. D., Munoz Del Rio, A., Rosas, H., Bruce, R. J., & Binkley, N. (2016). Effect of IV contrast on lumbar trabecular attenuation at routine abdominal

CT: correlation with DXA and implications for opportunistic osteoporosis screening. *Osteoporos Int, 27*(1), 147-152. doi:10.1007/s00198-015-3224-9

Pickhardt, P. J., Lee, L. J., del Rio, A. M., Lauder, T., Bruce, R. J., Summers, R. M., . . . Binkley, N. (2011). Simultaneous screening for osteoporosis at CT colonography: bone mineral density assessment using MDCT attenuation techniques compared with the DXA reference standard. *J Bone Miner Res, 26*(9), 2194-2203. doi:10.1002/jbmr.428

Pompe, E., Willemink, M. J., Dijkhuis, G. R., Verhaar, H. J., Mohamed Hoesein, F. A., & de Jong, P. A. (2015). Intravenous contrast injection significantly affects bone mineral density measured on CT. *Eur Radiol, 25*(2), 283-289. doi:10.1007/s00330-014-3408-2

Prokop, M. G., M.; Schaefer-Prokop, C.; van der Molen, A. J. (2007). Ganzkörper-Computertomographie. Spiral- und Multislice-CT. In U. Mödder (Ed.), *Referenz-Reihe Radiologie* (Vol. 2, pp. 15). Stuttgart, New York: Georg Thieme Verlag.

Rachner, T. D., Khosla, S., & Hofbauer, L. C. (2011). Osteoporosis: now and the future. *Lancet, 377*(9773), 1276-1287. doi:10.1016/S0140-6736(10)62349-5

Rajiah, P., Abbara, S., & Halliburton, S. S. (2017). Spectral detector CT for cardiovascular applications. *Diagn Interv Radiol, 23*(3), 187-193. doi:10.5152/dir.2016.16255

Ramesh, N., Moratti, S. C., & Dias, G. J. (2018). Hydroxyapatite-polymer biocomposites for bone regeneration: A review of current trends. *J Biomed Mater Res B Appl Biomater, 106*(5), 2046-2057. doi:10.1002/jbm.b.33950

Rassouli, N., Etesami, M., Dhanantwari, A., & Rajiah, P. (2017). Detector-based spectral CT with a novel dual-layer technology: principles and applications. *Insights Imaging, 8*(6), 589-598. doi:10.1007/s13244-017-0571-4

Reisz, J. A., Bansal, N., Qian, J., Zhao, W., & Furdui, C. M. (2014). Effects of ionizing radiation on biological molecules--mechanisms of damage and emerging methods of detection. *Antioxid Redox Signal, 21*(2), 260-292. doi:10.1089/ars.2013.5489

Riederer, I., Fingerle, A. A., Zimmer, C., Noel, P. B., Makowski, M. R., & Pfeiffer, D. (2021). Potential of dual-layer spectral CT for the differentiation between hemorrhage and iodinated contrast medium in the brain after endovascular treatment of ischemic stroke patients. *Clin Imaging, 79*, 158-164. doi:10.1016/j.clinimag.2021.04.020

Romman, Z. U., I.; Yagil, Y.; Finzi, D.; Wainer, N.; Milstein, D. (2015). Philips IQon Spectral CT. The Netherlands: Philips Healthcare.

Rossouw, J. E., Anderson, G. L., Prentice, R. L., LaCroix, A. Z., Kooperberg, C., Stefanick, M. L., . . . Writing Group for the Women's Health Initiative, I. (2002). Risks and benefits of estrogen plus progestin in healthy postmenopausal women: principal results From the Women's Health Initiative randomized controlled trial. *JAMA, 288*(3), 321-333. doi:10.1001/jama.288.3.321

Sambrook, P., & Cooper, C. (2006). Osteoporosis. *Lancet, 367*(9527), 2010-2018. doi:10.1016/S0140-6736(06)68891-0

Sambrook, P. N., Geusens, P., Ribot, C., Solimano, J. A., Ferrer-Barriendos, J., Gaines, K., . . . Melton, M. E. (2004). Alendronate produces greater effects than raloxifene on bone density and bone turnover in postmenopausal women with low bone density: results of EFFECT (Efficacy of FOSAMAX versus EVISTA Comparison Trial) International. *J Intern Med, 255*(4), 503-511. doi:10.1111/j.1365-2796.2004.01317.x

Sauter, A. P., Kopp, F. K., Munzel, D., Dangelmaier, J., Renz, M., Renger, B., . . . Noel, P. B. (2018). Accuracy of iodine quantification in dual-layer spectral CT: Influence of iterative reconstruction, patient habitus and tube parameters. *Eur J Radiol, 102*, 83-88. doi:10.1016/j.ejrad.2018.03.009

Schuit, S. C., van der Klift, M., Weel, A. E., de Laet, C. E., Burger, H., Seeman, E., . . . Pols, H. A. (2004). Fracture incidence and association with bone mineral density in elderly men and women: the Rotterdam Study. *Bone, 34*(1), 195-202. doi:10.1016/j.bone.2003.10.001

Schwaiger, B. J. (2022). Closing the diagnostic gap: increasing recognition of bone mineral density loss after treatment of lymphoma. *Leuk Lymphoma, 63*(2), 261-262. doi:10.1080/10428194.2021.1984461

Schwaiger, B. J., Gersing, A. S., Hammel, J., Mei, K., Kopp, F. K., Kirschke, J. S., . . . Noel, P. B. (2018). Three-material decomposition with dual-layer spectral CT compared to MRI

for the detection of bone marrow edema in patients with acute vertebral fractures. *Skeletal Radiol, 47*(11), 1533-1540. doi:10.1007/s00256-018-2981-x

Schwaiger, B. J., Kopperdahl, D. L., Nardo, L., Facchetti, L., Gersing, A. S., Neumann, J., . . . Link, T. M. (2017). Vertebral and femoral bone mineral density and bone strength in prostate cancer patients assessed in phantomless PET/CT examinations. *Bone, 101*, 62-69. doi:10.1016/j.bone.2017.04.008

Seo, G. H., Kang, H. Y., & Choe, E. K. (2018). Osteoporosis and fracture after gastrectomy for stomach cancer: A nationwide claims study. *Medicine (Baltimore), 97*(17), e0532. doi:10.1097/MD.0000000000010532

Shane, E., Burr, D., Abrahamsen, B., Adler, R. A., Brown, T. D., Cheung, A. M., . . . Whyte, M. P. (2014). Atypical subtrochanteric and diaphyseal femoral fractures: second report of a task force of the American Society for Bone and Mineral Research. *J Bone Miner Res, 29*(1), 1-23. doi:10.1002/jbmr.1998

Shefer, E. A., A.; Behling, R.; Goshen, R.; Gregorian, L.; Roterman, Y.; Uman, I.; Wainer, N.; Yagil, Y.; Zarchin, O. . (2013). State of the Art of CT Detectors and Sources: A Literature Review. *Curr Radiol Rep, 1*(1), 76-91. doi:10.1007/s40134-012-0006-4

Simonet, W. S., Lacey, D. L., Dunstan, C. R., Kelley, M., Chang, M. S., Luthy, R., . . . Boyle, W. J. (1997). Osteoprotegerin: a novel secreted protein involved in the regulation of bone density. *Cell, 89*(2), 309-319. doi:10.1016/s0092-8674(00)80209-3

Singh, J., & Daftary, A. (2008). Iodinated contrast media and their adverse reactions. *J Nucl Med Technol, 36*(2), 69-74; quiz 76-67. doi:10.2967/jnmt.107.047621

Smith, M. R., Egerdie, B., Hernandez Toriz, N., Feldman, R., Tammela, T. L., Saad, F., . . . Denosumab, H. P. C. S. G. (2009). Denosumab in men receiving androgen-deprivation therapy for prostate cancer. *N Engl J Med, 361*(8), 745-755. doi:10.1056/NEJMoa0809003

Solbak, M. S., Henning, M. K., England, A., Martinsen, A. C., Aalokken, T. M., & Johansen, S. (2020). Impact of iodine concentration and scan parameters on image quality, contrast enhancement and radiation dose in thoracic CT. *Eur Radiol Exp, 4*(1), 57. doi:10.1186/s41747-020-00184-z

Stone, K. L., Seeley, D. G., Lui, L. Y., Cauley, J. A., Ensrud, K., Browner, W. S., . . . Osteoporotic Fractures Research, G. (2003). BMD at multiple sites and risk of fracture of multiple types: long-term results from the Study of Osteoporotic Fractures. *J Bone Miner Res, 18*(11), 1947-1954. doi:10.1359/jbmr.2003.18.11.1947

Suttorp, N. M., M.; Siegmund, B.; Dietel, M. (2020). Harrisons Innere Medizin (Vol. 20, pp. 3647). Stuttgart: Thieme (Verlag).

Thomsen, J. S., Niklassen, A. S., Ebbesen, E. N., & Bruel, A. (2013). Age-related changes of vertical and horizontal lumbar vertebral trabecular 3D bone microstructure is different in women and men. *Bone, 57*(1), 47-55. doi:10.1016/j.bone.2013.07.025

Toelly, A., Bardach, C., Weber, M., Gong, R., Lai, Y., Wang, P., . . . Gruber, M. (2017). Influence of Contrast Media on Bone Mineral Density (BMD) Measurements from Routine Contrast-Enhanced MDCT Datasets using a Phantom-less BMD Measurement Tool. *Rofo, 189*(6), 537-543. doi:10.1055/s-0043-102941

Tsang, D. S., Merchant, T. E., Merchant, S. E., Smith, H., Yagil, Y., & Hua, C. H. (2017). Quantifying potential reduction in contrast dose with monoenergetic images synthesized from dual-layer detector spectral CT. *Br J Radiol, 90*(1078), 20170290. doi:10.1259/bjr.20170290

United Nations, D. o. E. a. S. A., Population Division. (2019). World Population Prospects 2019: Highlights. *(ST/ESA/SER.A/423)*.

Vaccaro, A. R., Oner, C., Kepler, C. K., Dvorak, M., Schnake, K., Bellabarba, C., . . . Trauma Knowledge, F. (2013). AOSpine thoracolumbar spine injury classification system: fracture description, neurological status, and key modifiers. *Spine (Phila Pa 1976), 38*(23), 2028-2037. doi:10.1097/BRS.0b013e3182a8a381

van der Hoorn, M. M. C., Tett, S. E., de Vries, O. J., Dobson, A. J., & Peeters, G. (2015). The effect of dose and type of proton pump inhibitor use on risk of fractures and osteoporosis treatment in older Australian women: A prospective cohort study. *Bone, 81*, 675-682. doi:10.1016/j.bone.2015.08.024

Van der Klift, M., De Laet, C. E., McCloskey, E. V., Hofman, A., & Pols, H. A. (2002). The incidence of vertebral fractures in men and women: the Rotterdam Study. *J Bone Miner Res, 17*(6), 1051-1056. doi:10.1359/jbmr.2002.17.6.1051

van Hamersvelt, R. W., Schilham, A. M. R., Engelke, K., den Harder, A. M., de Keizer, B., Verhaar, H. J., . . . Willemink, M. J. (2017). Accuracy of bone mineral density quantification using dual-layer spectral detector CT: a phantom study. *Eur Radiol, 27*(10), 4351-4359. doi:10.1007/s00330-017-4801-4

Van Hedent, S., Su, K. H., Jordan, D. W., Eck, B., Liang, F., Kessner, R., . . . Muzic, R. F., Jr. (2019). Improving Bone Mineral Density Assessment Using Spectral Detector CT. *J Clin Densitom, 22*(3), 374-381. doi:10.1016/j.jocd.2018.10.004

Van Staa, T. P., Laan, R. F., Barton, I. P., Cohen, S., Reid, D. M., & Cooper, C. (2003). Bone density threshold and other predictors of vertebral fracture in patients receiving oral glucocorticoid therapy. *Arthritis Rheum, 48*(11), 3224-3229. doi:10.1002/art.11283

Wang, R., Schoepf, U. J., Wu, R., Reddy, R. P., Zhang, C., Yu, W., . . . Zhang, Z. (2012). Image quality and radiation dose of low dose coronary CT angiography in obese patients: sinogram affirmed iterative reconstruction versus filtered back projection. *Eur J Radiol, 81*(11), 3141-3145. doi:10.1016/j.ejrad.2012.04.012

Wang, X., Sanyal, A., Cawthon, P. M., Palermo, L., Jekir, M., Christensen, J., . . . Keaveny, T. M. (2012). Prediction of new clinical vertebral fractures in elderly men using finite element analysis of CT scans. *J Bone Miner Res, 27*(4), 808-816. doi:10.1002/jbmr.1539

WHO. (1994). *Assessment of fracture risk and its application to screening for postmenopausal osteoporosis. Report of a WHO Study Group.* Paper presented at the World Health Organ Tech Rep Ser.

Wild, M., Dankerl, P., Hammon, M., Uder, M., & Janka, R. (2016). Vertebral body fractures of unknown origin in cancer patients receiving MDCT: reporting by radiologists and awareness by clinicians. *Springerplus, 5*, 450. doi:10.1186/s40064-016-2097-5

Willemink, M. J., & Noel, P. B. (2019). The evolution of image reconstruction for CT-from filtered back projection to artificial intelligence. *Eur Radiol, 29*(5), 2185-2195. doi:10.1007/s00330-018-5810-7

Willemink, M. J., Persson, M., Pourmorteza, A., Pelc, N. J., & Fleischmann, D. (2018). Photon-counting CT: Technical Principles and Clinical Prospects. *Radiology, 289*(2), 293-312. doi:10.1148/radiol.2018172656

Withers, P. J. B., C.; Carmignato, S.; Cnudde, V.; Grimaldi, D.; Hagen, C.K.; Maire, E.; Manley, M.; Du Plessis, A.; Stock, S.R. (2021). X-ray computed tomography. *Nature Reviews Methods Primers, 1*(1). doi:10.1038/s43586-021-00015-4

Wolff, J. (1892). *Das Gesetz der Transformation der Knochen*. Berlin: A. Hirschwald.

Yoo, R. E., Park, E. A., Lee, W., Shim, H., Kim, Y. K., Chung, J. W., & Park, J. H. (2013). Image quality of adaptive iterative dose reduction 3D of coronary CT angiography of 640-slice CT: comparison with filtered back-projection. *Int J Cardiovasc Imaging, 29*(3), 669-676. doi:10.1007/s10554-012-0113-6

Yu, E. W., Thomas, B. J., Brown, J. K., & Finkelstein, J. S. (2012). Simulated increases in body fat and errors in bone mineral density measurements by DXA and QCT. *J Bone Miner Res, 27*(1), 119-124. doi:10.1002/jbmr.506

Zhao, J. G., Zeng, X. T., Wang, J., & Liu, L. (2017). Association Between Calcium or Vitamin D Supplementation and Fracture Incidence in Community-Dwelling Older Adults: A Systematic Review and Meta-analysis. *JAMA, 318*(24), 2466-2482. doi:10.1001/jama.2017.19344

European Radiology
https://doi.org/10.1007/s00330-019-06263-z

MUSCULOSKELETAL

Bone mineral density measurements derived from dual-layer spectral CT enable opportunistic screening for osteoporosis

Ferdinand Roski[1] · Johannes Hammel[1,2] · Kai Mei[1] · Thomas Baum[3] · Jan S. Kirschke[3] · Alexis Laugerette[1,2] · Felix K. Kopp[1] · Jannis Bodden[1] · Daniela Pfeiffer[1] · Franz Pfeiffer[2] · Ernst J. Rummeny[1] · Peter B. Noël[1,4] · Alexandra S. Gersing[1] · Benedikt J. Schwaiger[1]

Received: 26 February 2019 / Revised: 22 April 2019 / Accepted: 2 May 2019

Abstract

Objective To investigate the in vivo applicability of non-contrast-enhanced hydroxyapatite (HA)-specific bone mineral density (BMD) measurements based on dual-layer CT (DLCT).

Methods A spine phantom containing three artificial vertebral bodies with known HA densities was measured to obtain spectral data using DLCT and quantitative CT (QCT), simulating different patient positions and grades of obesity. BMD was calculated from virtual monoenergetic images at 50 and 200 keV. HA-specific BMD values of 174 vertebrae in 33 patients (66 ± 18 years; 33% women) were determined in non-contrast routine DLCT and compared with corresponding QCT-based BMD values.

Results Examining the phantom, HA-specific BMD measurements were on a par with QCT measurements. In vivo measurements revealed strong correlations between DLCT and QCT ($r = 0.987$ [95% confidence interval, 0.963–1.000]; $p < 0.001$) and substantial agreement in a Bland–Altman plot.

Conclusion DLCT-based HA-specific BMD measurements were comparable with QCT measurements in in vivo analyses. This suggests that opportunistic DLCT-based BMD measurements are an alternative to QCT, without requiring phantoms and specific protocols.

Key Points

- *DLCT-based hydroxyapatite-specific BMD measurements show a substantial agreement with QCT-based BMD measurements in vivo.*
- *DLCT-based hydroxyapatite-specific measurements are on a par with QCT in spine phantom measurements.*
- *Opportunistic DLCT-based BMD measurements may be a feasible alternative for QCT, without requiring dedicated examination protocols or a phantom.*

Keywords Bone density · Osteoporosis · Tomography, x-ray computed

Ferdinand Roski and Johannes Hammel contributed equally to this work.

✉ Ferdinand Roski
ferdinand.roski@tum.de

[1] Department of Radiology, Klinikum rechts der Isar, School of Medicine, Technical University of Munich, Ismaninger Strasse 22, 81675 Munich, Germany

[2] Biomedical Physics & Munich School of BioEngineering, Technical University of Munich, 85748 Garching, Germany

[3] Department of Neuroradiology, Klinikum rechts der Isar, School of Medicine, Technical University of Munich, Ismaninger Strasse 22, 81675 Munich, Germany

[4] Department of Radiology, Perelman School of Medicine, University of Pennsylvania, 3400 Spruce St., 1 Silverstein, Philadelphia, PA 19104, USA

Published online: 21 May 2019

Abbreviations

BMD	Bone mineral density
DECT	Dual-energy computed tomography
DLCT	Dual-layer computed tomography
DSCT	Dual-source computed tomography
DXA	Dual-energy x-ray absorptiometry
ESP	European Spine Phantom
HA	Hydroxyapatite
MonoE	Virtual monoenergetic
QCT	Quantitative CT
SBI	Spectral base image

Introduction

Fragility fractures are the main symptom of osteoporosis and frequently occur in the thoracic and lumbar spine. Osteoporotic fractures affect the individual patient and are considered to be a relevant public health issue: they substantially contribute to the health care costs [1] and are associated with reduced health-related quality of life [2]. Ultimately, prevalent vertebral and hip fractures lead to an increased risk of mortality for up to 5 and 10 years after fracture event, respectively [3, 4].

Dual-energy x-ray absorptiometry (DXA) and quantitative CT (QCT), the current clinical standards, are known to have limitations such as high susceptibility to confounders like body size or vascular calcifications and limited availability or relatively high radiation doses, respectively [5].

Furthermore, these methods are under-used with participation rates for DXA of only 30% and 4% in eligible women and men over 65 years, respectively [6]. Consequently, opportunistic imaging is particularly promising for spinal osteodensitometry, as many patients undergo diagnostic CT of the chest or abdomen for a variety of indications and these scans mostly also include the spinal column [7, 8]. Since osteoporosis is considered to be an underdiagnosed and undertreated condition [1], opportunistic screening would enhance the identification of individuals with low BMD being at risk for spinal fractures and thus would enable the prevention of major fragility fractures by an early initiation of therapy, e.g., with pharmacological treatment.

For material-specific measurements and other applications, dual-layer CT (DLCT) has gained growing attention: This special approach of dual-energy CT (DECT) was only recently introduced in clinical routine and uses two scintillator elements, one superimposed on the other, coupled to a photodiode. Both layers have sensitivity maxima in two different parts of the x-ray spectrum and therefore provide spectral information [9]. This information can be used to decompose attenuation values and derive material-specific density information, thus combining volumetric measurements specifically for calcium hydroxyapatite (HA) with a morphological assessment [10].

Of note, the basic concept of dual-energy imaging is not a new one in osteodensitometry. Dual-energy techniques have been introduced more than 30 years ago, both in the context of projectional radiography [11–13] and computed tomography [14, 15]. Especially for DECT, an early application in bone mineral quantification was to reduce measuring inaccuracies of conventional single-energy CT that are caused by beam hardening artifacts or vertebral bone marrow fat [16, 17].

Other current approaches to DECT imaging, acquiring spectral information, are dual-source CT (DSCT) and single-source CT with fast kV-switching. While the former uses two x-ray sources and two detectors in a nearly perpendicular set-up, the latter employs one x-ray source with rapid tube voltage switching and one detector [10].

Contrary to these source-based DECT setups, DLCT only requires one x-ray source and both detector layers are always "ON" in all examinations. Therefore, dual-energy information is available from every routine clinical examination whereas in contrast, in dual-source or rapid kV-switching systems, examinations are often performed in single-energy mode only, and dual-energy information are collected only if prescribed prior to the examination. Due to its simultaneous data acquisition of the low- and high-energy data sets, DLCT, however, continuously allows for additional analyses in already-acquired imaging data such as BMD measurements in non-dedicated examinations.

This opportunistic approach could help reduce the gap in the detection of patients with low BMD and consequently pave the way for establishing appropriate treatment. The first ex vivo studies, in which HA-specific BMD measurements were assessed in hydroxyapatite-containing phantoms and vertebral specimens, demonstrated the high accuracy of HA-specific BMD measurements [18, 19].

Therefore, the purpose of this study was to investigate the clinical applicability of non-contrast-enhanced DLCT-based HA-specific BMD quantification in vivo by evaluating its accuracy compared with phantom-calibrated QCT-based BMD measurements.

Methods

Ex vivo calibration and measurements in a standardized phantom

CT images were acquired with one DLCT scanner (IQon Spectral CT, Philips Healthcare).

A standardized spine phantom (European Spine Phantom (ESP), serial number ESP-040, QRM GmbH) consisting of water-equivalent plastic and HA inserts simulating trabecular bone densities of 50.0 (HA50), 98.4 (HA100), and 197.6 (HA200) mg/ml HA was measured. It should be noted that the exact HA densities as specified by the manufacturer were used for all calculations and analyses, whereas the nominal

values were used only for illustrational purposes in tables and figures. The ESP is a tool for standard quality control in DXA and QCT [20–22]. To determine the precise spectral absorption behavior of the ESP, an ultra-high-dose examination protocol with a fixed tube voltage of 120 kVp and an exposure of 1000 mAs was used. Spectral base image (SBI) data was reconstructed using a standard bone filter kernel (YB) with axial slice thickness of 0.9 mm. The measured data was averaged over cylindrical regions of interest (ROIs) of 10.0 mm (height) × 100 mm^2 (base area) to reduce noise.

SBI data contains information on energy-dependent attenuation behavior, extracted with the use of dual-layer detector technology [23]. This information can be used to create virtual monochromatic (MonoE) images, which are equivalent to images acquired with a monoenergetic x-ray source [24]. These images were generated with IntelliSpace Portal 10.1.0 (Philips Healthcare).

In addition to the calibration scan, 18 scans were performed using different scan parameter combinations with the following variations in patient size, table height, and exposure, to simulate various patient setups:

- Fat-equivalent extension rings (QRM GmbH) (for the simulation of different degrees of obesity): no ring, ring size S, and ring size M (50 mm and 100 mm thick fat-equivalent ring, respectively)
- Centered and off-centered (patient positioning table was moved 43 mm away from the field of view center) table positions
- 50, 100, and 200 mAs exposure
- Tube voltage of 120 kVp

CT numbers from monoenergetic images at 50 and 200 keV were used for BMD quantification: Projection points along the optimal regression line are calculated by applying a projection with an angle of 32° to the calibration line to all scan setups. Via the known BMD values of the ESP, every point on the calibration line can be assigned to a specific BMD using the linear relation

$$BMD\left[\frac{mg}{ml}\right] = MonoE_{projection}(50)\,[HU] \times u + v.$$

u and v are the slope and intercept of a linear regression between the MonoE(50) values of the calibration scan and the manufacturer-specified BMDs. Finally, for comparison purposes, the ESP scans as specified above were repeated using routine QCT examination parameters. QCT-based BMD values were calculated using a clinical QCT phantom and its corresponding software (QCT Pro, Mindways Software, Inc.).

Patient cohort for in vivo BMD measurements

Institutional Review Board approval was obtained previously to this study (Ethics Commission of the Medical Faculty, Technical University of Munich, Germany). Written informed consent was waived for this retrospective analysis of routinely acquired imaging data.

In our institutional PACS, patients who underwent a QCT examination on the DLCT scanner between November 2016 and February 2018 were retrospectively identified. All examination data had to contain spectral information, and the thoracolumbar spine had to be examined in the presence of a standardized QCT-phantom as specified above. Patients with intravenous contrast ($n = 39$) or metal implants in the thoracolumbar spine or close vicinity (e.g., spondylodeses, aortic stent grafts; $n = 36$) were excluded. A total number of $n = 33$ subjects (mean ± SD; 66 ± 18 years; 11 women, 57 ± 22 years; 22 men, 69 ± 13 years) were used for the comparison of DLCT- and QCT-based BMD measurements with a total of 174 vertebral bodies.

DLCT imaging protocols and post-processing

All CT images were acquired with the same DLCT scanner as used for phantom measurements during clinical routine.

Routine protocols with tube voltage fixed at 120 kVp were used for all scans. Here, patient exposures varied between 20 and 294 mAs, with a mean exposure of 84 ± 61 mAs (mean ± SD). Mean CT dose indices ($CTDI_{vol}$) were 7.7 ± 5.5 mGy over all patients. SBI data sets were reconstructed using standard and bone filter kernels (B, YB, YC), with a slice thickness of 0.9 mm. The distance between the top of the patient table and the center of rotation was 151 mm ± 34 mm.

Under the supervision of a radiologist with 7 years of experience in spine imaging (BJS), a trained researcher (FR) manually placed circular ROIs onto sagittal reformations (slice thickness, 10 mm) of the thoracolumbar spine as these reformations allow best for synchronous morphological assessment including fractures that may be missed in original axial imaging data (e.g., height loss of vertebrae). ROIs had a diameter of exactly one-third of the particular vertebral body's height and were positioned in the ventral halves of the trabecular compartment of the vertebrae (Fig. 1). On average, five vertebrae per patient were measured (preferably T12, L1, and L2; range T10 to L5). Vertebral bodies with substantial degenerative changes (e.g., severe osteochondrosis with adjacent sclerosis), fractures, or other pathologies such as hemangioma were excluded and the BMD measurements were consequently obtained from the adjacent vertebrae that were not excluded due to a pathology.

Mean CT numbers for both conventional and corresponding virtual monochromatic images at 50 and 200 keV were extracted from ROIs. HA-specific BMD quantification of all patients was computed using reconstructions of virtual monochromatic images at 50 and 200 keV as described for phantom measurements. For comparison, BMD assessment was also performed by using the QCT Pro calibration phantom

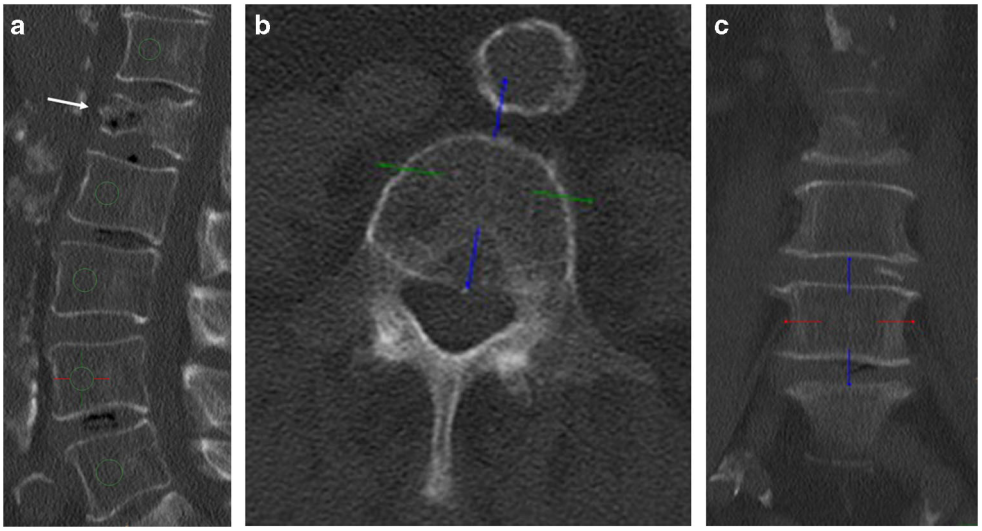

Fig. 1 Sagittal (**a**), axial (**b**), and coronal (**c**) reformation of dual-layer spectral CT imaging of a 77-year-old male patient after history of falling. ROIs are positioned in ventral halves of T12 and L2–L5; L1 was excluded due to a compression fracture (white arrow)

(Mindways Software, Inc.) with BMD being calculated in accordance with the conventional QCT method and clinical standards.

Statistical analysis

For the inter-method comparison of ex vivo phantom measurements, means of differences between the scan and manufacturer-specified BMDs were assessed for DLCT versus QCT scans with identical examination parameters, respectively, using a two-sided paired samples *t* test.

On a vertebral-body-base, Pearson's *r* was determined to assess the correlation of DLCT- and QCT-based BMD. A Bland–Altman plot was used to evaluate the agreement of both measurements [25].

To assess the intrareader agreement of HA-specific BMD measurements, the same researcher repeated measurements in 20% of the vertebral bodies ($n = 35$) after 4 months, blinded for previous results, and two-way mixed intraclass correlation coefficients (ICC) were calculated.

Statistical analyses were performed with SPSS 25 (IBM). A two-sided p value of less than 0.05 was considered to indicate a statistically significant difference.

Results

Ex vivo DLCT-based phantom measurements

The spectral data obtained from the calibration scan and the scans simulating different patient setups were plotted separately for three artificial vertebral bodies (Fig. 2), and a projection calibration was executed, defining projection angles of $\alpha = 29.9°$, $\beta = 29.1°$, and $\gamma = 32.0°$ for vertebral bodies containing 50.0, 98.4, and 197.6 mg/ml HA, respectively. These projection angles represent the angles between the linear regression line of the high-dose calibration scan for different BMDs and the linear regression of the 18 scans in different setups for each BMD. Deviations from the calibration line are mainly caused by different patient sizes, while different table heights and exposure only cause minor aberrations. For our algorithm, an angle of $\gamma = 32.0°$ was used, as this projection calibration sets the highest correlation coefficient ($r = -0.947$).

In phantom measurements, means of differences between BMD scan results and manufacturer-specified values averaged for all different scan settings tended to be lower for DLCT (3.9 mg/ml HA) compared with those of QCT (4.8 mg/ml HA) (Table 1), although this difference was not statistically significant ($p = 0.152$).

In vivo DLCT-based BMD measurements

BMD values derived from the DLCT-based method and from QCT were highly correlated ($r = 0.987$ [95% confidence interval, 0.963–1.000]; $p < 0.001$; Fig. 3). The corresponding Bland–Altman plot shows a substantial agreement between both methods (Fig. 4). DLCT-based BMD measurements show a mean difference from QCT measurements of $\overline{d} = 2.81$ mg/ml (95% confidence interval, 1.64–3.99 mg/ml) with a standard deviation of differences of $s_d = 7.89$ mg/ml. The 95% limits of agreement subsequently are − 12.66 mg/ml and + 18.29 mg/ml.

The intrareader agreement for DLCT-based BMD measurements was excellent (ICC, 0.997 [95% CI, 0.994–0.998]).

Discussion

In this study, opportunistic HA-specific BMD measurements derived from clinical DLCT examinations showed an excellent correlation with QCT-based BMD measurements.

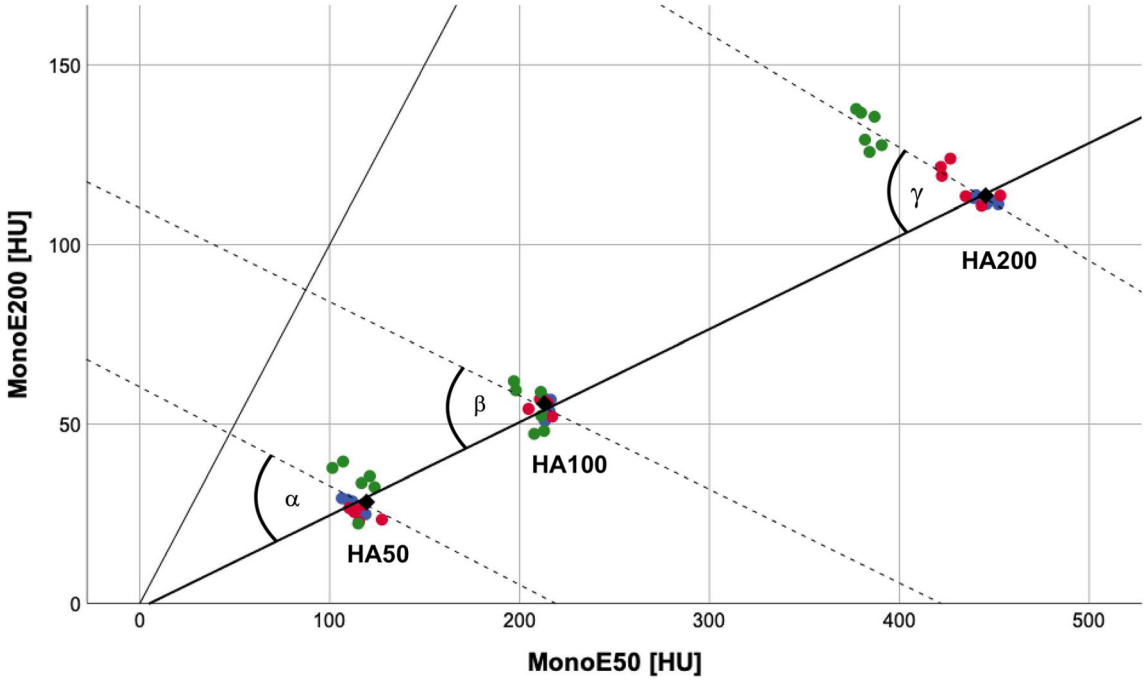

Fig. 2 Scatter plot showing phantom measurement results of calibration scans with different simulated setups in terms of patient size (blue represents "no extension ring", red represents ring size S, green represents ring size M), table position, and exposure for three artificial vertebral bodies of prespecified HA densities (50.0 (HA50), 98.4 (HA100), and 197.6 (HA200) mg/ml HA). The thick black line represents the regression line of the ultra-high-dose calibration scan (1000 mAs exposure), the thin black line represents the bisecting line, and broken lines are the regression lines for measurements of individual HA inserts. Projection angles are $\alpha = 29.9°$, $\beta = 29.1°$, and $\gamma = 32.0°$

Table 1 Differences between measurements (QCT/DLCT) and manufacturer-specified BMD. Means of differences (MOD) are calculated from the absolute deviations from manufacturer's specifications of 50.0, 98.4, and 197.6 mg/ml HA densities (HA50, HA100, HA200, respectively)

Ring size	Table position	Exposure (mAs)	QCT			DLCT			MOD (QCT)	MOD (DLCT)
			HA50	HA100	HA200	HA50	HA100	HA200		
No ring	Centered	50	47.3	95.6	201.6	46.8	93.0	194.7	3.2	3.8
		100	47.3	98.6	201.4	46.6	94.6	196.0	2.2	2.9
		200	47.3	96.6	199.6	47.7	95.1	195.9	2.2	2.4
	Off-centered	50	45.3	96.2	203.3	47.9	90.2	194.1	4.2	4.6
		100	50.3	96.4	199.0	47.4	95.6	194.4	1.2	2.9
		200	46.1	94.4	200.5	47.2	94.0	195.0	3.6	3.3
S	Centered	50	52.9	99.5	199.7	46.1	90.8	193.5	2.0	5.2
		100	45.7	97.5	196.2	45.9	94.6	198.1	2.2	2.8
		200	46.0	94.5	199.8	48.7	94.3	196.6	3.4	2.1
	Off-centered	50	49.0	94.5	195.4	44.3	92.2	193.5	2.4	5.3
		100	49.1	96.2	201.1	47.8	94.5	199.7	2.2	2.7
		200	46.3	94.8	194.7	46.3	94.4	194.8	3.4	3.5
M	Centered	50	54.5	93.7	192.3	53.9	86.1	198.1	4.8	5.6
		100	45.6	104.4	190.3	55.6	93.2	199.0	5.9	4.1
		200	46.3	97.1	189.9	53.1	94.9	198.3	4.2	2.4
	Off-centered	50	40.9	88.8	179.6	43.9	88.0	190.7	12.2	7.8
		100	35.4	86.8	179.0	52.6	91.0	193.7	14.9	4.6
		200	41.3	87.1	182.5	55.3	96.1	192.7	11.7	4.2
Overall			46.5	95.2	194.8	48.7	92.9	195.5	4.8	3.9

Explicit results and means of differences between measurements and manufacturer's specifications (MOD) given in mg/ml

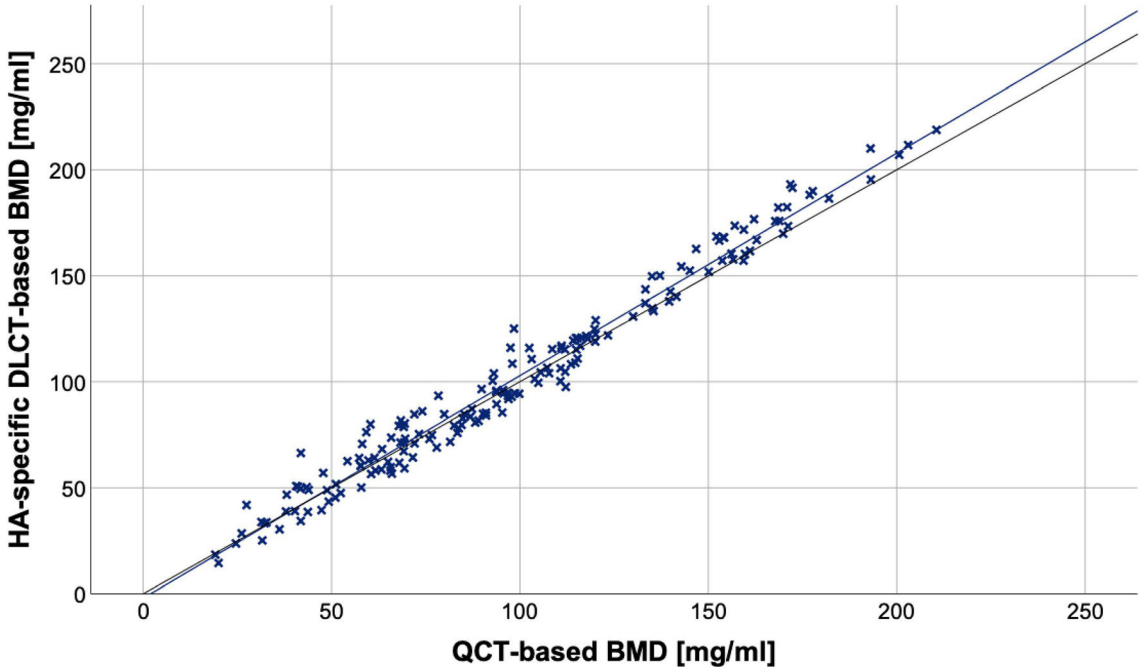

Fig. 3 Scatter plot showing BMD values of 174 vertebral bodies from 33 patients, BMD values obtained by phantomless DLCT (*y*-axis) and phantom-based QCT (*x*-axis); the blue line represents the linear regression line, and the black line represents the bisecting line. A significant correlation between both measurement methods can be identified ($r = 0.987$ [95% confidence interval, 0.963–1.000]; $p < 0.001$)

Furthermore, measurements in the standardized ESP suggest that the presented DLCT-based method is on a par with those from QCT.

In a clinical assessment, the American College of Radiology lists the following BMD ranges for use to approximately assign QCT-based BMD to the WHO diagnostic categories "osteopenia" and "osteoporosis", which are actually exclusively established for DXA measurements: for osteopenia, BMD values range between 80 and 120 mg/ml and for osteoporosis, BMD values are < 80 mg/ml [26]. In this clinically relevant range, both methods showed a substantial agreement in in vivo measurements. Here, a slight but significant systematic difference can be observed with DLCT consistently yielding higher BMD than QCT. Larger deviations between the two methods at higher BMD values mainly result from the introduced projection angle, taking the influence of simulated abdominal fat tissue into consideration. Of note, over all simulated measurement setups, phantom measurements deviated less from known HA densities in the ESP for the DLCT-based method than for QCT.

This may be caused by the so-called fat error affecting non-HA-specific QCT measurements: several studies have identified a high bone marrow fat fraction as a source of error in osteodensitometry, which is associated with an underestimation of BMD in QCT-based measurements by using magnetic resonance spectroscopy [27, 28] or chemical analysis [29, 30] as standard of reference. Of note, the determination of ash density values in vertebral specimens demonstrated a reduction of the fat-related error with DECT [30].

In a different DECT approach, Booz et al showed the feasibility of phantomless in vivo BMD assessment using DSCT [31]. DSCT, however, has inherent limitations compared with the dual-layer setup used in this study. The nearly perpendicular arrangement of both x-ray sources is not only responsible for an asynchronous detection of congruent projections and therefore does not allow material decomposition in projection space, but it is also the cause of scatter radiation on respective radiation fields with the need for correction [10].

The method for DLCT-based BMD quantification as used in this study is similar to a previous ex vivo study by Mei et al [19]. In this previous study, different degrees of obesity were not found to influence HA-specific BMD measurements significantly within the range of clinical examination parameters. While differences between DLCT-based measurements and known HA densities of the ESP in suboptimal examination setups were still within acceptable dimensions, we decided to additionally introduce a projection calibration step as described above to further increase accuracy of measurements. Of note, this step only needs to be performed once on the CT scanner after measuring the ESP.

DLCT data is acquired without preselected examination protocols and can therefore be used for different opportunistic analyses, e.g., to reduce artifacts from metallic hardware [32] or to create virtual non-contrast images from contrast-enhanced examinations [33]. In the detection of low BMD, opportunistic use of already-available imaging data has recently received a lot of attention [7, 8, 34–36] for several reasons: Many patients at risk for fractures due to impaired

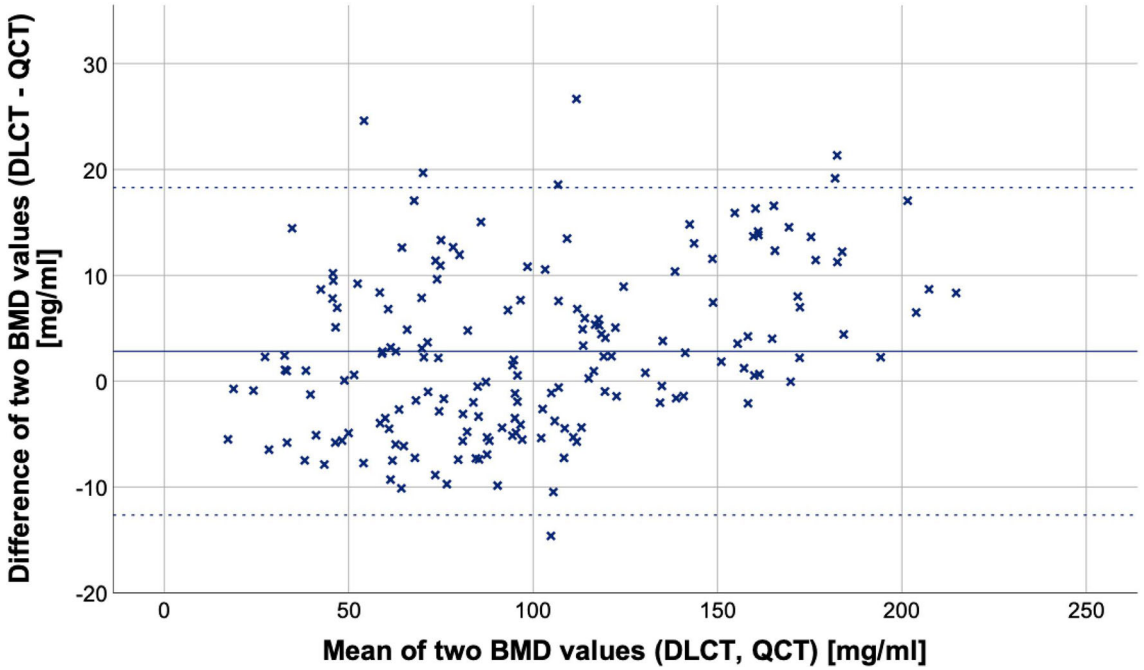

Fig. 4 Bland–Altman plot showing data of 174 vertebral bodies from 33 patients, solid line indicating the mean BMD difference, dotted lines indicating the 95% limits of agreement (mean difference ± 1.96 SD). The plot shows means of DLCT- and QCT-based BMD values on the *x*-axis and differences of both measurements (DLCT- minus QCT-based BMD) on the *y*-axis. The mean difference is $\overline{d}$ = 2.81 mg/ml (95% confidence interval, 1.64–3.99 mg/ml) with a standard deviation of differences of s_d = 7.89 mg/ml. The 95% limits of agreement subsequently are − 12.66 mg/ml and + 18.29 mg/ml. This indicates a substantial agreement between both measurement methods

bone stability undergo CT imaging for other reasons such as vertebral fracture assessment in patients with primary osteoporosis, but also CT staging examinations e.g. in the presence of malignant conditions. Using these images for BMD analyses would provide an accurate biomarker without additional radiation doses, examination time, and costs, thus potentially closing the diagnostic gap for individuals at increased fracture risk.

This study has limitations. First, the patient population was rather small since for the inter-method comparison, DLCT and QCT examinations performed on the same scanner were required for this study population. In addition, strict exclusion criteria regarding patients with metal implants in adjacent structures (e.g., spondylodeses, aortic stent grafts) were applied to avoid possible measurement errors by reason of beam hardening artifacts. Comparison of both CT techniques in quantifying bone mineral density was therefore performed on a base of single vertebral bodies (n = 174). As measurements in the standardized phantom suggest, the results of the DLCT-based method tally with those obtained by QCT. However, before final conclusions are drawn, both methods should be objectively compared using a third method as standard of reference. This could be determining the BMD with both methods in vertebral specimens which are then burned and chemically analyzed for their HA density, which, however, is not applicable in vivo.

Besides, BMD has shown to be only one of several parameters for fracture risk evaluation, with trabecular bone microstructure being another relevant factor. Whether microstructure assessment based on DLCT and QCT may generate different results should also be assessed in the future. Finally, in this analysis, only non-contrast-enhanced CT examinations were included. Since many clinical examinations are performed with intravenous contrast (e.g., staging examinations), the feasibility of measurements in those contrast-enhanced examinations should be investigated in future studies.

In conclusion, opportunistic HA-specific BMD measurements derived from clinical DLCT examinations were highly correlated and showed a substantial agreement with QCT-based BMD measurements. Moreover, phantom measurements suggest that the presented DLCT-based method is on a par with QCT. This suggests that opportunistic HA-specific measurements may be an adequate alternative for early detecting patients with low bone mineral density in clinical routine and may support optimal individual therapeutic decisions.

Funding This study has received funding by the European Research Council (ERC-StG-2014 637164; H2020, AdG 695045), by the German Federal Ministry of Education and Research (BMBF) under grant IMEDO (13GW0072C), by the German Research Foundation (as part of the Gottfried Wilhelm Leibniz program), and by the TUM Institute for Advanced Study, funded by the German Excellence Initiative.

Compliance with ethical standards

Guarantor The scientific guarantor of this publication is Dr. Benedikt J. Schwaiger, MD.

Conflict of interest The authors of this manuscript declare no relationships with any companies whose products or services may be related to the subject matter of the article.

Statistics and biometry No complex statistical methods were necessary for this paper.

Informed consent Written informed consent was waived by the Institutional Review Board.

Ethical approval Institutional Review Board approval was obtained.

Methodology
- Retrospective
- Diagnostic or prognostic study
- Performed at one institution

References

1. Haussler B, Gothe H, Göl D, Glaeske G, Pientka L, Felsenberg D (2007) Epidemiology, treatment and costs of osteoporosis in Germany–the BoneEVA Study. Osteoporos Int 18:77–84
2. Hallberg I, Bachrach-Lindstrom M, Hammerby S, Toss G, Ek AC (2009) Health-related quality of life after vertebral or hip fracture: a seven-year follow-up study. BMC Musculoskelet Disord 10:135
3. Bliuc D, Nguyen ND, Milch VE, Nguyen TV, Eisman JA, Center JR (2009) Mortality risk associated with low-trauma osteoporotic fracture and subsequent fracture in men and women. JAMA 301:513–521
4. Ioannidis G, Papaioannou A, Hopman WM et al (2009) Relation between fractures and mortality: results from the Canadian multicentre osteoporosis study. CMAJ 181:265–271
5. Link TM (2012) Osteoporosis imaging: state of the art and advanced imaging. Radiology 263:3–17
6. Curtis JR, Carbone L, Cheng H et al (2008) Longitudinal trends in use of bone mass measurement among older Americans, 1999-2005. J Bone Miner Res 23:1061–1067
7. Fidler JL, Murthy NS, Khosla S et al (2016) Comprehensive assessment of osteoporosis and bone fragility with CT colonography. Radiology 278:172–180
8. Pickhardt PJ, Pooler BD, Lauder T, del Rio AM, Bruce RJ, Binkley N (2013) Opportunistic screening for osteoporosis using abdominal computed tomography scans obtained for other indications. Ann Intern Med 158:588–595
9. Rassouli N, Etesami M, Dhanantwari A, Rajiah P (2017) Detector-based spectral CT with a novel dual-layer technology: principles and applications. Insights Imaging 8:589–598
10. Patino M, Prochowski A, Agrawal MD et al (2016) Material separation using dual-energy CT: current and emerging applications. Radiographics 36:1087–1105
11. Brody WR, Butt G, Hall A, Macovski A (1981) A method for selective tissue and bone visualization using dual energy scanned projection radiography. Med Phys 8:353–357
12. Katoh T, Sakamaki K, Nakamura T (1981) A new method for measurement of bone mineral deposition pattern–using dual energy radiographic densitometry method in a single exposure. Bull Tokyo Med Dent Univ 28:91–98
13. Sartoris DJ, Sommer FG, Kosek J, Gies A, Carter D (1985) Dual-energy projection radiography in the evaluation of femoral neck strength, density, and mineralization. Invest Radiol 20:476–485
14. Genant HK, Boyd D (1977) Quantitative bone mineral analysis using dual energy computed tomography. Invest Radiol 12:545–551
15. Goodsitt MM, Rosenthal DI, Reinus WR, Coumas J (1987) Two postprocessing CT techniques for determining the composition of trabecular bone. Invest Radiol 22:209–215
16. Adams JE, Chen SZ, Adams PH, Isherwood I (1982) Measurement of trabecular bone mineral by dual energy computed tomography. J Comput Assist Tomogr 6:601–607
17. Laval-Jeantet AM, Cann CE, Roger B, Dallant P (1984) A postprocessing dual energy technique for vertebral CT densitometry. J Comput Assist Tomogr 8:1164–1167
18. van Hamersvelt RW, Schilham AMR, Engelke K et al (2017) Accuracy of bone mineral density quantification using dual-layer spectral detector CT: a phantom study. Eur Radiol 27:4351–4359
19. Mei K, Schwaiger BJ, Kopp FK et al (2017) Bone mineral density measurements in vertebral specimens and phantoms using dual-layer spectral computed tomography. Sci Rep 7:17519
20. Kalender WA, Perman WH, Vetter JR, Klotz E (1986) Evaluation of a prototype dual-energy computed tomographic apparatus. I. Phantom studies. Med Phys 13:334–339
21. Kalender WA, Seissler W, Klotz E, Vock P (1990) Spiral volumetric CT with single-breath-hold technique, continuous transport, and continuous scanner rotation. Radiology 176:181–183
22. Genant HK (1995) Universal standardization for dual X-ray absorptiometry: patient and phantom cross-calibration results. J Bone Miner Res 10:997–998
23. Ehn S, Sellerer T, Muenzel D et al (2018) Assessment of quantification accuracy and image quality of a full-body dual-layer spectral CT system. J Appl Clin Med Phys 19:204–217
24. Yu L, Leng S, McCollough CH (2012) Dual-energy CT-based monochromatic imaging. AJR Am J Roentgenol 199:S9–S15
25. Bland JM, Altman DG (1999) Measuring agreement in method comparison studies. Stat Methods Med Res 8:135–160
26. American College of Radiology (2018) ACR–SPR–SSR practice parameter for the performance of musculoskeletal quantitative computed tomography (QCT). Available via https://www.acr.org/-/media/ACR/Files/Practice-Parameters/qct.pdf?la=en. Accessed 19 July 2018
27. Baum T, Yap SP, Karampinos DC et al (2012) Does vertebral bone marrow fat content correlate with abdominal adipose tissue, lumbar spine bone mineral density, and blood biomarkers in women with type 2 diabetes mellitus? J Magn Reson Imaging 35:117–124
28. Bredella MA, Daley SM, Kalra MK, Brown JK, Miller KK, Torriani M (2015) Marrow adipose tissue quantification of the lumbar spine by using dual-energy CT and single-voxel (1)H MR spectroscopy: a feasibility study. Radiology 277:230–235
29. Kuiper JW, van Kuijk C, Grashuis JL, Ederveen AG, Schütte HE (1996) Accuracy and the influence of marrow fat on quantitative CT and dual-energy X-ray absorptiometry measurements of the femoral neck in vitro. Osteoporos Int 6:25–30
30. Laval-Jeantet AM, Roger B, Bouysee S, Bergot C, Mazess RB (1986) Influence of vertebral fat content on quantitative CT density. Radiology 159:463–466

31. Booz C, Hofmann PC, Sedlmair M et al (2017) Evaluation of bone mineral density of the lumbar spine using a novel phantomless dual-energy CT post-processing algorithm in comparison with dual-energy X-ray absorptiometry. Eur Radiol Exp 1:11
32. Dangelmaier J, Schwaiger BJ, Gersing AS et al (2018) Dual layer computed tomography: reduction of metal artefacts from posterior spinal fusion using virtual monoenergetic imaging. Eur J Radiol 105:195–203
33. Riederer I, Fingerle AA, Baum T et al (2018) Acute infarction after mechanical thrombectomy is better delineable in virtual non-contrast compared to conventional images using a dual-layer spectral CT. Sci Rep 8:9329
34. Pickhardt PJ, Lee LJ, del Rio AM et al (2011) Simultaneous screening for osteoporosis at CT colonography: bone mineral density assessment using MDCT attenuation techniques compared with the DXA reference standard. J Bone Miner Res 26:2194–2203
35. Lee SJ, Binkley N, Lubner MG, Bruce RJ, Ziemlewicz TJ, Pickhardt PJ (2016) Opportunistic screening for osteoporosis using the sagittal reconstruction from routine abdominal CT for combined assessment of vertebral fractures and density. Osteoporos Int 27:1131–1136
36. Schwaiger BJ, Kopperdahl DL, Nardo L et al (2017) Vertebral and femoral bone mineral density and bone strength in prostate cancer patients assessed in phantomless PET/CT examinations. Bone 101: 62–69

European Radiology
https://doi.org/10.1007/s00330-020-07319-1

COMPUTED TOMOGRAPHY

Opportunistic osteoporosis screening: contrast-enhanced dual-layer spectral CT provides accurate measurements of vertebral bone mineral density

Ferdinand Roski[1] · Johannes Hammel[1,2] · Kai Mei[1,3] · Bernhard Haller[4] · Thomas Baum[5] · Jan S. Kirschke[5] · Daniela Pfeiffer[1] · Klaus Woertler[1] · Franz Pfeiffer[2] · Peter B. Noël[3] · Alexandra S. Gersing[1] · Benedikt J. Schwaiger[1,5]

Received: 2 July 2020 / Revised: 4 August 2020 / Accepted: 17 September 2020

Abstract

Objectives Osteoporosis remains under-diagnosed, which may be improved by opportunistic bone mineral density (BMD) measurements on CT. However, correcting for the influence of intravenous iodine-based contrast agent is challenging. The purpose of this study was to assess the diagnostic accuracy of iodine-corrected vertebral BMD measurements derived from non-dedicated contrast-enhanced phantomless dual-layer spectral CT (DLCT) examinations.

Methods Vertebral volumetric DLCT-BMD was measured in native, arterial, and portal-venous scans of 132 patients (63 ± 16 years; 32% women) using virtual monoenergetic images (50 and 200 keV). For comparison, conventional BMD was determined using an asynchronous QCT calibration. Additionally, iodine densities were measured in the abdominal aorta (AA), inferior vena cava, and vena portae (VP) on each CT phase to adjust for iodine-related measurement errors in multivariable linear regressions and a generalized estimated equation, and conversion equations were calculated.

Results BMD values derived from contrast-enhanced phases using conversion equations adjusted for individual vessel iodine concentrations of VP and/or AA showed a high agreement with those from non-enhanced scans in Bland-Altman plots. Mean absolute errors (MAE) of DLCT-BMD were 3.57 mg/ml for the arterial ($R^2 = 0.989$) and 3.69 mg/ml for the portal-venous phase ($R^2 = 0.987$) (conventional BMD: 4.70 [$R^2 = 0.983$] and 5.15 mg/ml [$R^2 = 0.981$]). In the phase-independent analysis, MAE was 4.49 mg/ml for DLCT ($R^2 = 0.989$) (conventional BMD: 4.82 mg/ml [$R^2 = 0.981$]).

Conclusions Converted BMD derived from contrast-enhanced DLCT examinations and adjusted for individual vessel iodine concentrations showed a high agreement with non-enhanced DLCT-BMD, suggesting that opportunistic BMD measurements are feasible even in non-dedicated contrast-enhanced DLCT examinations.

Key Points

- *Accurate BMD values can be converted from contrast-enhanced DLCT scans, independent from the used scan phase.*
- *DLCT-BMD measurements from contrast-enhanced scans should be adjusted with iodine concentrations of portal vein and/or abdominal aorta, which significantly improves the goodness-of-fit of conversion models.*

Keywords Bone density · Contrast media · Osteoporosis · Tomography, X-ray computed

✉ Ferdinand Roski
ferdinand.roski@tum.de

[1] Department of Radiology, Klinikum rechts der Isar, School of Medicine, Technical University of Munich, Ismaninger Str. 22, 81675 Munich, Germany

[2] Biomedical Physics & Munich School of BioEngineering, Technical University of Munich, 85748 Garching, Germany

[3] Department of Radiology, Perelman School of Medicine, University of Pennsylvania, Philadelphia, PA 19104, USA

[4] Institute of Medical Statistics and Epidemiology, Klinikum rechts der Isar, School of Medicine, Technical University of Munich, 81675 Munich, Germany

[5] Department of Neuroradiology, Klinikum rechts der Isar, School of Medicine, Technical University of Munich, 81675 Munich, Germany

Published online: 14 October 2020

Abbreviations

AA	Aorta abdominalis
ADT	Androgen deprivation therapy
AR	Arterial scan phase
BMD	Bone mineral density
cBMD	Converted BMD
CE	Contrast-enhanced
$CTDI_{vol}$	CT dose index
DECT	Dual-energy computed tomography
DLCT	Dual-layer spectral computed tomography
DXA	Dual-energy x-ray absorptiometry
GEE	Generalized estimated equations
HA	Calcium hydroxyapatite
IVC	Inferior vena cava
MAE	Mean absolute error
MDCT	Multidetector computed tomography
PI	Phase-independent
PV	Portal-venous scan phase
QCT	Quantitative computed tomography
R^2c	Change of R^2
VFFs	Vertebral fragility fractures
VMI	Virtual monoenergetic image
VOI	Volume of interest
VP	Vena portae

Introduction

Osteopenia and osteoporosis remain a severe challenge in health care, not only from a clinical perspective—the treatment gap is estimated at 59% of women and 57% of men in the EU [1]—but also from an epidemiologic view considering its contribution to an increasing number of fall-related deaths [2]. Bearing in mind that the majority of the causal vertebral fragility fractures (VFFs) already occurs in osteopenic individuals [3] emphasizes the importance of early detecting patients at risk. A UK audit, however, showed that incidental VFFs are substantially underdiagnosed in non-dedicated CT exams due to deficient reporting [4]. Here, even basic tools (e.g., routine sagittal reformations, stringent terminology) could improve clinico-radiological workflow and patients' outcome [5]. Besides, fracture-related treatment costs represent the main cost factor for osteoporosis, thus causing considerable economic burden to health systems [1].

A diagnostic gap was not only found in patients with primary or postmenopausal osteoporosis [6–8]—this is also an issue regarding patients with secondary causes for reduced bone mineral density (BMD), e.g., patients suffering from malignant conditions and undergoing therapy also affecting BMD [9]. For instance, men with prostate cancer receiving androgen deprivation therapy (ADT) bear an increased risk to suffer from accelerated bone loss, which is a major adverse effect [10–12]. Even though guidelines recommend evaluation with baseline and periodic follow-up BMD quantification [13], there is a severe under-use of dedicated imaging methods such as dual-energy x-ray absorptiometry (DXA) or quantitative CT (QCT)—e.g., for patients with non-metastatic prostate cancer, only about one in ten patients over 65 years receiving ADT undergoes a baseline bone densitometry [14–16].

Most patients with such malignant conditions are regularly subjected to contrast-enhanced CT for (re-)staging or the assessment of age-related comorbidities, in which a vast set of imaging data is generated. This gave rise to the question whether contrast-enhanced CT scans may be used for opportunistic BMD measurements to avoid additional dedicated examinations.

In clinical osteodensitometry, dual-energy CT (DECT) imaging has been available for more than 30 years [17]. However, in contrast to other DECT approaches such as dual-source CT or single-source CT with rapid kV switching, which are routinely performed in single-energy mode, DLCT continuously detects dual-energy information in standard CT protocols. Consequently, this novel implementation of DECT provides spectral data on clinical demand in all examinations without the need to prospectively select qualified patients for DECT imaging. Providing spectral information retrospectively in all examinations not only does facilitate radiological workflow, but also virtually lends itself for the retrospective approach of opportunistically measuring BMD.

By means of two superimposed detector layers, dual-layer spectral CT (DLCT) enables the separation of low- and high-energy photons, therefore providing energy-specific attenuation coefficients of present materials [18]. Based on this spectral information, one can infer on the material composition of body tissues or fluids, e.g., by measuring the concentration of calcium hydroxyapatite for BMD quantification [19] or the iodine concentration for quantifying contrast enhancement [20].

In a previous publication, the feasibility of opportunistic screening for osteoporosis was already demonstrated in vivo for native DLCT examinations [21]. Consequently, the scope of applicability in this paper is confined to clinical settings in which current non-enhanced DLCT data are missing.

The objective of this study was to evaluate the usability of contrast-enhanced DLCT scans for calculating precise BMD values based on non-dedicated CT examinations, i.e., with examinations performed for indications other than osteodensitometry.

For this purpose, the present analysis investigated (I) the effects of iodine contrast agent on the accuracy of DLCT-BMD measurements and (II) any possible improvement of accuracy by adjusting for concentrations of iodine contrast agent measured in large vessels.

Materials and methods

Patient population

According to the study protocol, 471 consecutive patients with a complete triphasic DLCT examination of the abdomen or thorax/abdomen were enrolled if exams were performed for indications other than osteodensitometry. Of those, patients with metal-containing implants adjacent to the thoracolumbar spine such as aortic stent grafts ($n = 293$) or spinal instrumentation ($n = 36$) were excluded. The same applies for patients with malignant conditions affecting the spine, e.g., spinal bone metastases ($n = 7$) or hematologic diseases ($n = 3$), resulting in a patient sample of 132 patients (63 ± 16 years; 32% women) who were retrospectively identified in the institutional PACS between September 2016 and October 2018.

Institutional Review Board approval was obtained prior to this study (Ethics Commission of the School of Medicine, Technical University of Munich, Germany). Informed consent was waived for this retrospective analysis of routinely acquired imaging data.

DLCT image acquisition

CT images were acquired with one DLCT scanner (IQon Spectral CT, Philips Healthcare). For all scans, a routine abdominal CT protocol was used with a tube voltage of 120 keV. Non-contrast-enhanced (NE) scans had an exposure of 107 ± 49 mAs (mean ± SD) and a mean CT dose index ($CTDI_{vol}$) of 9.7 ± 4.5 mGy; contrast-enhanced (CE) scans had an exposure of 110 ± 43 mAs and a mean $CTDI_{vol}$ of 10.0 ± 3.9 mGy.

CE scans were performed using iomeprol, a non-ionic iodinated contrast agent for intravenous application (Imeron 400 MCT, Bracco Imaging Deutschland GmbH). Per routine clinical protocol and depending on the clinical situation, a volume of 50 to 70 ml was administered with a flow rate of 3 ml/s. Arterial phases were triggered when the average CT numbers of a volume of interest (VOI) in the descending thoracic aorta exceeded a threshold value of 150 HU. The portal-venous phases started 70 s after contrast administration.

Image analysis, post-processing, and BMD calculation

On sagittal reformations, circular VOIs were manually placed in the ventral halves of L1 to L3. If one or more of these showed a pathology such as a fracture or extensive degenerative changes, adjacent thoracolumbar vertebrae were used instead. CT numbers in NE, arterial (AR), and portal-venous (PV) phases were extracted from both conventional and two virtual monoenergetic images at different energy levels (VMI; 50 and 200 keV), respectively (Fig. 1).

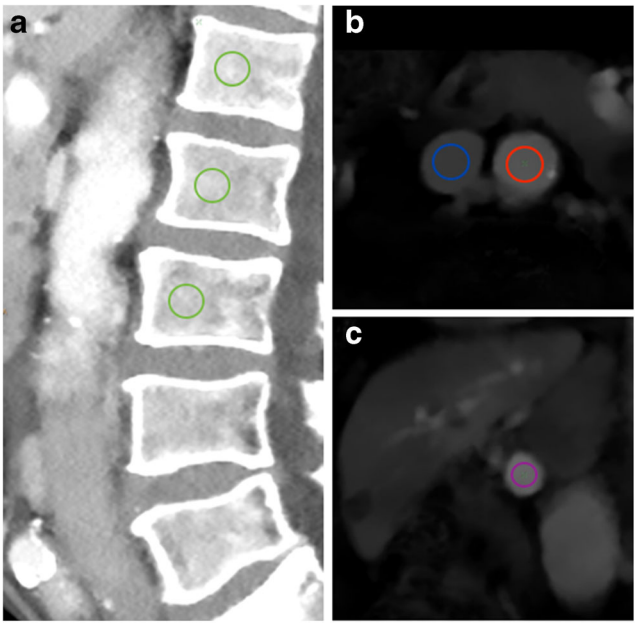

Fig. 1 Sagittal (**a**), axial (**b**), and multiplanar reformation (**c**) of dual-layer spectral CT imaging of a 77-year-old male patient. Spinal VOIs are positioned in the ventral halves of L1–L3 (green) (VMI at 50 keV). Vascular VOIs are positioned orthogonally and mid-luminally in the abdominal aorta (red), the inferior vena cava (blue), and the portal vein (violet) (iodine density maps)

Subsequently, patients' BMD values were calculated in two ways: Based on VMIs, DLCT-BMD values were computed for all three scan phases as previously described by Roski et al [21]. In short, after performing an ex vivo high-dose calibration scan of three hydroxyapatite (HA)-containing insets of the European spine phantom (ESP) with DLCT, attenuation values of VMIs can be linearly assigned to respective BMD values via projection calibration as they are proportional to measured HA concentrations.

Conventional BMD values were similarly calculated for all scan phases by using an asynchronous calibration [22, 23] with attenuation values of a standard QCT phantom (Mindways QCT) consisting of five differently concentrated solutions of K_2PO_4. Here, phantom measurements were averaged over 33 examinations, which were performed in the same time period and on the same scanner. Instead of VMIs, conventional images were used for BMD quantification. These are reconstructed by using a weighted sum of counts measured in the two detector layers, with resulting images being analogous to a conventional single-energy CT scanner [24].

Additionally, mid-luminal iodine concentrations (mg/ml) were measured within the abdominal aorta (AA) and the inferior vena cava (IVC) on axial images—immediately inferior to the renal vessels—as well as within the vena portae (VP) on multiplanar reformations (Fig. 1). A commercially available spectral CT software was used for the generation of iodine density maps based on iodine-water decomposition (IntelliSpace Portal 10.1.0, Philips Healthcare).

Statistical analysis

Both DLCT and conventional BMD values from CE scans were separately correlated with their reference values from corresponding NE scans in multivariable linear regression models using forward selection. BMD values from CE scans, vessel iodine concentrations (AA, IVC, and VP), age, and sex represented the set of selectable independent variables. DLCT-BMD from NE scans had previously shown its validity in a comparison with QCT [21]. Consequently, these data served as standard of reference for the contrast-enhanced DLCT-BMD values in this study. Likewise, the respective native values served as the dependent variable for conventional BMD. This linear regression analysis was performed separately for AR and PV. For the phase-independent (PI) approach, due to present within-subject correlation, generalized estimated equations (GEE) were used to investigate functional relations between contrast-enhanced and native BMD.

Beforehand, the patient sample was randomly split up into a training cohort ($n = 88$) for the multivariable linear regression model and a test cohort ($n = 44$) for the eventual validation of its predictive accuracy. For the phase-independent GEE analysis, individual patient scans of the AR and PV phase were independently assigned to the training cohort ($n = 176$) and the test cohort ($n = 88$).

Bland-Altman plots showing data from the test cohorts were used to examine the agreement of native and calculated BMD values, thus estimating the predictive value of the regression model. Moreover, agreement was calculated on a patient base as mean of absolute errors (MAEs) before and after the application of conversion equations. The external data of the test cohort was used to validate the conversion equations of both linear regressions and the GEE analysis with R^2 values.

The statistical calculations were performed using SPSS 23 (IBM).

Results

In vivo DLCT-based and conventional BMD measurements

For DLCT-BMD, measurements in native scans averaged to 102.95 ± 46.33 mg/ml (mean ± SD), whereas arterial (112.23 ± 7.88 mg/ml [+ 9.0%]) and portal-venous (126.86 ± 53.89 mg/ml [+ 23.2%]) scan phases revealed substantially higher results (Fig. 2). DLCT-BMD from AR and PV showed high correlations ($r = 0.994$ [95% confidence interval, 0.991–0.996] and $r = 0.989$ [0.984–0.992]), yet a low agreement with DLCT-BMD from NE.

Conventionally calculated BMD showed similar, yet continuously lower results: native BMD values were 97.00 ± 43.48 mg/ml, whereas in CE phases, likewise, BMD values were substantially higher with 106.44 ± 44.35 mg/ml (+ 9.7%) for AR and 119.67 ± 42.93 mg/ml (+ 23.3%) for PV, respectively.

Linear regression and generalized estimating equation analyses

Both phase-specific regression models had very high coefficients of determination for DLCT-BMD measurements with conventional BMD values consistently showing lower goodness of fit (Table 1).

Besides respective BMD values from CE scan phases, a significant association of the iodine concentration of the VP could be detected for all three DLCT models (AR: change of R^2 (R^2c) = 0.007 (DLCT-BMD)/R^2c = 0.008 (conventional BMD), PV: R^2c = 0.001/not significant). Patient's age was significantly associated with the outcome only for the phase-independent GEE analysis, the iodine concentration of AA only for the PV linear regression model (R^2c = 0.008/R^2c =

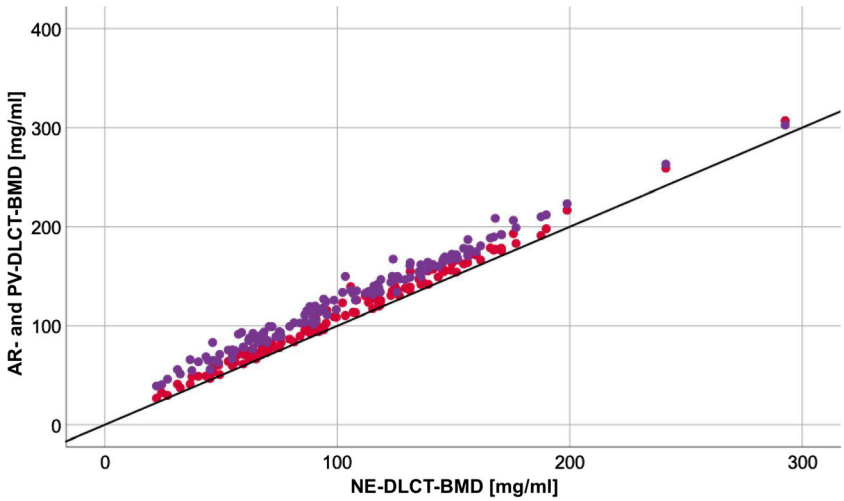

Fig. 2 Scatter plot showing DLCT-BMD values of 132 patients (averaged over three vertebrae each) derived from different contrast-enhanced scan phases (AR = red and PV = violet); the black bisecting line serves as standard of reference showing the corresponding line of native BMD values

Table 1 Comparison of R^2 change and adjusted R^2 for several multivariable linear regression analyses with forward selection, either based on contrast-enhanced DLCT-BMD or on conventional BMD data, respective native BMD values served as dependent variable, illustrated for AR and PV

	Variable	DLCT-BMD (R^2c/R^2adj)	Conv. BMD (R^2c/R^2adj)
a) arterial phase			
AR			
1	BMD_{AR}	0.983 ($p = 0.000$)	0.978 ($p = 0.000$)
2	$Iodine_{VP}$	0.007 ($p = 0.000$)	0.008 ($p = 0.000$)
Total		0.990	0.986
b) portal-venous phase			
PV			
1	BMD_{PV}	0.976 ($p = 0.000$)	0.966 ($p = 0.000$)
2	$Iodine_{AA}$	0.008 ($p = 0.000$)	0.010 ($p = 0.000$)
3	$Iodine_{VP}$	0.001 ($p = 0.019$)	-
Total		0.984	0.975

0.010). Neither iodine concentration of IVC nor sex was identified as a significant predictor for any scan phase.

The derived conversion equations for the DLCT-BMD data are:

$$\mathrm{cBMD(AR)} = 0.989 \times \mathrm{BMD(AR)} - 2.170 \times \mathrm{Iodine(VP)} - 4.070$$
$$\mathrm{cBMD(PV)} = 0.981 \times \mathrm{BMD(PV)} - 1.407 \times \mathrm{Iodine(AA)} - 1.109 \times \mathrm{Iodine\ (VP)} - 5.928$$
$$\mathrm{cBMD(PI)} = 0.941 \times \mathrm{BMD(CE)} - 2.636 \times \mathrm{Iodine(VP)} - 0.141 \times \mathrm{Age} + 9.233$$

Agreement of native and calculated BMD

After converting the BMD values of the test cohorts using the presented equations, corresponding Bland-Altman plots showed a substantial agreement between converted and respective natively measured BMD (Fig. 3).

For the arterial phase, DLCT-BMD had a mean of absolute errors (MAEs) of 9.99 (95% confidence interval, 8.38–11.59) mg/ml before and 3.57 (2.56–4.58) mg/ml after the conversion of measured to estimated BMD, whereas conventional BMD improved from 9.93 (8.12–11.75) to 4.70 (3.53–5.86) mg/ml.

For the portal-venous phase, conversion of contrast-enhanced data reduced MAE from 21.58 (19.73–23.42) mg/ml to 3.69 (2.69–4.70) mg/ml for DLCT-BMD (21.76 [19.39–24.13] to 5.15 [3.76–6.54] mg/ml for conventional BMD).

The MAE of the phase-independent GEE model changed from 14.57 (12.81–16.33) mg/ml before to 4.49 (3.87–5.11) mg/ml after the conversion of DLCT-BMD (14.77 [12.88–16.66] to 4.82 [3.99–5.64] mg/ml for conventional BMD).

The above conversion equations were validated with external data of the test cohorts and consistently showed high coefficients of determination (Table 2).

Discussion

Converted BMD values, derived from routine clinical contrast-enhanced DLCT and adjusted for vessel iodine concentrations, showed a high agreement with non-enhanced DLCT-BMD. Moreover, the phase-independent conversion equation provides results which are adequate for the detection of low BMD in a clinical context as well.

Before this conversion, DLCT-BMD values were consistently higher for all scan phases when measured in contrast-enhanced scans compared with their native BMD references (Fig. 2). This represents the challenge of adequately separating intravascular iodine within the vertebra from HA, which is attributable to similar spectral absorption behavior of the two components. Another explanation for this BMD variation is the present dual-layer set-up, which cannot provide absolute selectivity on the detector level due to an overlap of the high- and low-energy spectra [25, 26].

As the very same VOIs were used for comparing both calculations, the utilization of spectral information is capable of additionally improving overall BMD accuracy. Although DLCT is still not perfectly specific for HA, the consistently higher coefficients of determination in the linear regression (Table 1) and the GEE analysis suggest that DLCT-BMD shows a more pronounced functional relation between contrast-enhanced and native scans compared with conventional BMD. Besides, quantifying iodine concentrations outside osseous structures, more precisely in large vessels (Vena portae, Aorta), significantly improves the accuracy of converted BMD.

In a pilot analysis ($n = 12$), tissue iodine concentrations of paraspinal muscle and fat were measured for all scan phases. Balancing the linear model between completeness and

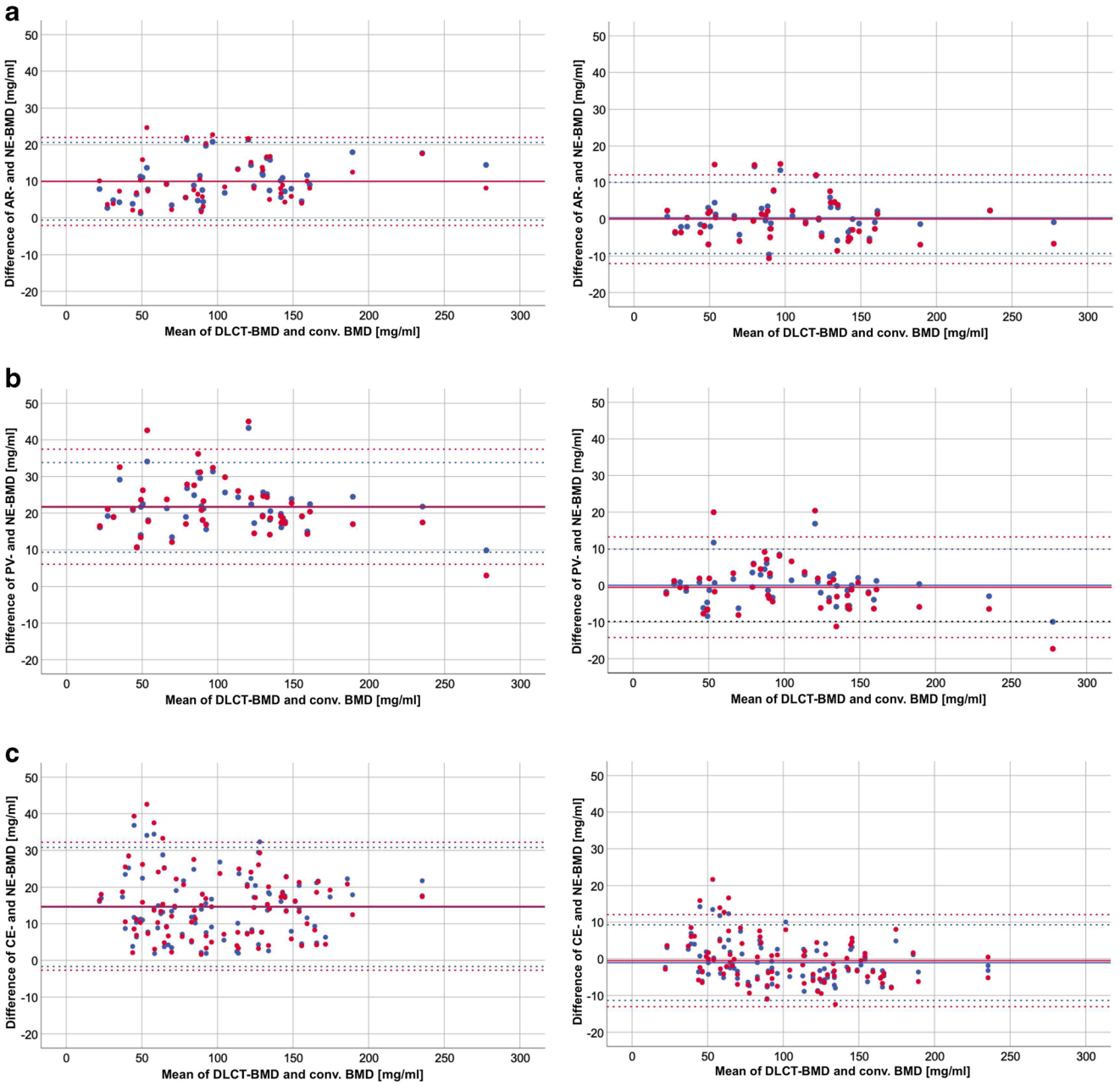

Fig. 3 Bland-Altman plots showing data of randomly selected test cohorts ($n = 44$ for AR and PV, $n = 88$ for PI); the y-axis shows differences between BMD derived from contrast-enhanced scan phases and native BMD; the x-axis shows mean values of native DLCT-BMD and native conventional BMD; the black solid lines indicate equivalence of BMD values; the colored solid lines indicate the mean of BMD differences; the colored dotted lines indicate the 95% limits of agreement (mean difference ± 1.96 SD); blue represents data of DLCT-BMD; red represents data of conventional BMD; top row = AR (**a**), middle row = PV (**b**), bottom row = PI (**c**); left column: BMD data before application of conversion equation, right column: estimated BMD after application of conversion equation

Table 2 Coefficients of determination (R^2) for external data of the test cohorts ($n = 44$ for AR and PV, $n = 88$ for PI)

	DLCT-BMD (R^2)	Conv. BMD (R^2)
Arterial phase (AR)	0.989	0.983
Portal-venous phase (PV)	0.987	0.981
Phase-independent analysis (PI)	0.989	0.981

complexity, however, the rationale was to set up a slender, numerically stable model without overfitting or multicollinearity. Here, preliminary data suggested focusing on vessel iodine measurements in order to adjust for the influence of intravascular contrast agent. After the conversion, DLCT-BMD showed a high agreement between native and converted values in Bland-Altman plots (Fig. 3a–c) and a substantial reduction of MAEs (relative reduction of 64% for

AR, 83% for PV, and 69% for PI). The validation with external data of the test cohort revealed coefficients of determination that are equivalent to those of the training cohort (Table 2). This finding confirms a numerically stable model for BMD prediction that is accurate in new data.

Particularly the phase-independent approach features critical advantages over phase-specific conversion equations as in clinical routine, the iodine concentration within the vertebra's trabecular compartment may be affected by numerous factors apart from scan timing [27, 28]: e.g., contrast application speed, volume, the patient's circulatory capacity, volume of distribution, red vs. yellow bone marrow ratio. BMD values derived from a phase-independent conversion equation could minimize the influence of those factors and therefore may be most useful in clinical reality.

Focusing on contrast-enhanced clinical DLCT exams, these routinely acquired clinical CT data were utilized for opportunistic BMD measurements to monitor changes such as tumor- or therapy-associated bone loss, when current non-enhanced scans are missing. The proposed DLCT-based method provides the opportunity to retrospectively screen for low BMD and could at once spare patients additional exposure to radiation by dedicated bone densitometric exams. Quantifying individual iodine concentrations in abdominal vessels turned out to be a practicable way of adjusting for the influence of intravascular contrast agent. In this context, there is extensive literature indicating the high accuracy of DLCT-based iodine quantification: within the typically encountered concentration ranges in clinical radiology, relative mean errors of about 3.3 to 4.6% were found, with simulated patient size and tube voltage inconsistently affecting measuring precision [20, 29, 30].

Comparable studies assessing iodine-associated effects on BMD quantification with multidetector CT (MDCT) encountered limitations: a study by Baum et al had a small training cohort for the conversion equation, relied on phantom calibration and only used PV scans [31]. A comparable study by Kaesmacher et al was limited by a small number of enrolled patients [32].

The conversion equations in this DLCT study, however, are based on a solid training cohort of 88 patients. An additional correction step was introduced by adjusting for vascular iodine concentrations, which can be obtained with minimal effort in work and time. Besides, DLCT potentially combines the inherent benefits of dual-energy imaging for osteodensitometry with the major advantage of QCT, i.e., exclusive volumetric measurements of the trabecular compartment, which is more sensitive regarding therapy-associated bone remodeling processes [33]—however, without needing synchronous phantom calibration.

Note that the present statistical models already show very high determination coefficients for conventional BMD: contrary to a comparable study investigating asynchronously calibrated BMD derived from contrast-enhanced MDCT, DLCT-BMD has substantially narrower 95% limits of agreement (− 10 to + 11 mg/ml (DLCT) vs. ca. − 30 to + 14 mg/ml (MDCT) for AR and − 10 to + 10 mg/ml (DLCT) vs. ca. − 39 to + 8 mg/ml for PV) and a better linear fit (R^2: 0.983 vs. 0.923 for AR, 0.976 vs. 0.904 for PV) [32]. Considering the minor contribution of the vessel iodine corrections, these results suggest a notably higher measuring accuracy of the DLCT scanner compared with MDCT.

Apart from several phantom studies, two in vivo trials already showed the diagnostic accuracy of native DLCT regarding osteodensitometric applications: Van Hedent et al demonstrated that DLCT-based BMD measurements perform very well in the detection of decreased BMD using DXA as standard of reference [34]. A previously mentioned study by Roski et al showed that non-enhanced DLCT-based BMD measurements are on a par with phantom-based QCT [21].

This study has limitations. As CT exams were retrieved from clinical routine, there was no systematic variation in the amount of applied contrast agent to adjust for contrast load. Furthermore, neither overall circulatory parameters nor the local vascularization of the vertebral bodies for correlating contrast distribution could be investigated according to the retrospective nature of this analysis. Moderating both scan protocol inconsistencies and varying circulatory parameters, the phase-independent analysis is potentially meeting clinical reality best. Besides, the vertebral VOIs were placed manually, which contributes to the risk of a higher intra- or interobserver variability. A next step would be to overcome this issue by implementing a BMD analysis pipeline drawing on automatic segmentation. Additional longitudinal studies will be needed to investigate the in vivo reproducibility and the predictive power regarding incidental fractures.

In summary, this study showed that BMD values can be accurately estimated from contrast-enhanced multiphasic dual-layer spectral CT examinations, even independently from the used contrast phase. Moreover, measuring only one abdominal vessel for iodine concentration could significantly increase the goodness-of-fit in statistical models. Therefore, iodine-adjusted DLCT-BMD measurements suggest their potential value for a reliable opportunistic assessment of BMD even in routine clinical contrast-enhanced examinations.

Funding Open Access funding enabled and organized by Projekt DEAL. This work was supported by the European Research Council (ERC-StG-2014 637164; H2020, AdG 695045); by the German Federal Ministry of Education and Research (BMBF) under grant IMEDO (13GW0072C); by the German Research Foundation (as part of the Gottfried Wilhelm Leibniz program); and by the TUM Institute for Advanced Study, funded by the German Excellence Initiative.

Compliance with ethical standards

Guarantor The scientific guarantor of this publication is Dr. Benedikt J. Schwaiger, MD.

Conflict of interest The authors of this manuscript declare no relationships with any companies, whose products or services may be related to the subject matter of the article.

Statistics and biometry No complex statistical methods were necessary for this paper.

Informed consent Written informed consent was waived by the Institutional Review Board.

Ethical approval Institutional Review Board approval was obtained.

Methodology
- retrospective
- diagnostic or prognostic study
- performed at one institution

References

1. Hernlund E, Svedbom A, Ivergard M et al (2013) Osteoporosis in the European Union: medical management, epidemiology and economic burden. A report prepared in collaboration with the International Osteoporosis Foundation (IOF) and the European Federation of Pharmaceutical Industry Associations (EFPIA). Arch Osteoporos 8:136
2. Sanchez-Riera L, Carnahan E, Vos T et al (2014) The global burden attributable to low bone mineral density. Ann Rheum Dis 73:1635–1645
3. Pasco JA, Seeman E, Henry MJ, Merriman EN, Nicholson GC, Kotowicz MA (2006) The population burden of fractures originates in women with osteopenia, not osteoporosis. Osteoporos Int 17:1404–1409
4. Howlett DC, Drinkwater KJ, Mahmood N, Illes J, Griffin J, Javaid K (2020) Radiology reporting of osteoporotic vertebral fragility fractures on computed tomography studies: results of a UK national audit. Eur Radiol. https://doi.org/10.1007/s00330-020-06845-2
5. Abrahamsen B (2020) Hiding in plain sight-unreported osteoporotic vertebral fractures. Eur Radiol. https://doi.org/10.1007/s00330-020-06944-0
6. Feldstein A, Elmer PJ, Orwoll E, Herson M, Hillier T (2003) Bone mineral density measurement and treatment for osteoporosis in older individuals with fractures: a gap in evidence-based practice guideline implementation. Arch Intern Med 163:2165–2172
7. Siris ES, Miller PD, Barrett-Connor E et al (2001) Identification and fracture outcomes of undiagnosed low bone mineral density in postmenopausal women: results from the National Osteoporosis Risk Assessment. JAMA 286:2815–2822
8. Lafata JE, Kolk D, Peterson EL et al (2007) Improving osteoporosis screening: results from a randomized cluster trial. J Gen Intern Med 22:346–351
9. Pfeilschifter J, Diel IJ (2000) Osteoporosis due to cancer treatment: pathogenesis and management. J Clin Oncol 18:1570–1593
10. Melton LJ 3rd, Lieber MM, Atkinson EJ et al (2011) Fracture risk in men with prostate cancer: a population-based study. J Bone Miner Res 26:1808–1815
11. Dalla Via J, Daly RM, Owen PJ, Mundell NL, Rantalainen T, Fraser SF (2019) Bone mineral density, structure, distribution and strength in men with prostate cancer treated with androgen deprivation therapy. Bone 127:367–375
12. Greenspan SL, Coates P, Sereika SM, Nelson JB, Trump DL, Resnick NM (2005) Bone loss after initiation of androgen deprivation therapy in patients with prostate cancer. J Clin Endocrinol Metab 90:6410–6417
13. Gralow JR, Biermann JS, Farooki A et al (2013) NCCN Task Force report: bone health in cancer care. J Natl Compr Canc Netw 11(Suppl 3):S1–S50 quiz S51
14. Holt A, Khan MA, Gujja S, Govindarajan R (2015) Utilization of bone densitometry for prediction and administration of bisphosphonates to prevent osteoporosis in patients with prostate cancer without bone metastases receiving antiandrogen therapy. Cancer Manag Res 7:13–18
15. Suarez-Almazor ME, Peddi P, Luo R, Nguyen HT, Elting LS (2014) Low rates of bone mineral density measurement in Medicare beneficiaries with prostate cancer initiating androgen deprivation therapy. Support Care Cancer 22:537–544
16. Shahinian VB, Kuo YF (2013) Patterns of bone mineral density testing in men receiving androgen deprivation for prostate cancer. J Gen Intern Med 28:1440–1446
17. Genant HK, Boyd D (1977) Quantitative bone mineral analysis using dual energy computed tomography. Invest Radiol 12:545–551
18. Rassouli N, Etesami M, Dhanantwari A, Rajiah P (2017) Detector-based spectral CT with a novel dual-layer technology: principles and applications. Insights Imaging 8:589–598
19. Mei K, Schwaiger BJ, Kopp FK et al (2017) Bone mineral density measurements in vertebral specimens and phantoms using dual-layer spectral computed tomography. Sci Rep 7:17519
20. Pelgrim GJ, van Hamersvelt RW, Willemink MJ et al (2017) Accuracy of iodine quantification using dual energy CT in latest generation dual source and dual layer CT. Eur Radiol 27:3904–3912
21. Roski F, Hammel J, Mei K et al (2019) Bone mineral density measurements derived from dual-layer spectral CT enable opportunistic screening for osteoporosis. Eur Radiol. https://doi.org/10.1007/s00330-019-06263-z
22. Wang L, Su Y, Wang Q et al (2017) Validation of asynchronous quantitative bone densitometry of the spine: accuracy, short-term reproducibility, and a comparison with conventional quantitative computed tomography. Sci Rep 7:6284
23. Budoff MJ, Malpeso JM, Zeb I et al (2013) Measurement of phantomless thoracic bone mineral density on coronary artery calcium CT scans acquired with various CT scanner models. Radiology 267:830–836
24. Hojjati M, Van Hedent S, Rassouli N et al (2017) Quality of routine diagnostic abdominal images generated from a novel detector-based spectral CT scanner: a technical report on a phantom and clinical study. Abdom Radiol (NY) 42:2752–2759

25. Shefer E, Altman A, Behling R et al (2013) State of the art of CT detectors and sources: a literature review. Curr Radiol Rep 1:76–91
26. Faby S, Kuchenbecker S, Sawall S et al (2015) Performance of today's dual energy CT and future multi energy CT in virtual non-contrast imaging and in iodine quantification: a simulation study. Med Phys 42:4349–4366
27. Acu K, Scheel M, Issever AS (2014) Time dependency of bone density estimation from computed tomography with intravenous contrast agent administration. Osteoporos Int 25:535–542
28. Pompe E, Willemink MJ, Dijkhuis GR, Verhaar HJ, Mohamed Hoesein FA, de Jong PA (2015) Intravenous contrast injection significantly affects bone mineral density measured on CT. Eur Radiol 25:283–289
29. Ehn S, Sellerer T, Muenzel D et al (2018) Assessment of quantification accuracy and image quality of a full-body dual-layer spectral CT system. J Appl Clin Med Phys 19:204–217
30. Sauter AP, Kopp FK, Munzel D et al (2018) Accuracy of iodine quantification in dual-layer spectral CT: influence of iterative reconstruction, patient habitus and tube parameters. Eur J Radiol 102: 83–88
31. Baum T, Muller D, Dobritz M, Rummeny EJ, Link TM, Bauer JS (2011) BMD measurements of the spine derived from sagittal reformations of contrast-enhanced MDCT without dedicated software. Eur J Radiol 80:e140–e145
32. Kaesmacher J, Liebl H, Baum T, Kirschke JS (2017) Bone mineral density estimations from routine multidetector computed tomography: a comparative study of contrast and calibration effects. J Comput Assist Tomogr 41:217–223
33. Black DM, Greenspan SL, Ensrud KE et al (2003) The effects of parathyroid hormone and alendronate alone or in combination in postmenopausal osteoporosis. N Engl J Med 349:1207–1215
34. Van Hedent S, Su KH, Jordan DW et al (2018) Improving bone mineral density assessment using spectral detector CT. J Clin Densitom. https://doi.org/10.1016/j.jocd.2018.10.004